

N71-23604
NASA CR-118009



GULF RADIATION TECHNOLOGY

Gulf-RT-10482

STUDY OF RADIATION EFFECTS IN SILICON SOLAR CELLS

Final Report

B. C. Passenheim, R. A. Berger, J. F. Colwell,
and J. A. Naber

**CASE FILE
COPY**

Prepared for
Jet Propulsion Laboratory
Pasadena, California 91103

under
Contract 952387

January 29, 1971

GULF RADIATION TECHNOLOGY
A DIVISION OF GULF ENERGY & ENVIRONMENTAL SYSTEMS COMPANY
P.O. BOX 608, SAN DIEGO, CALIFORNIA 92112



GULF RADIATION TECHNOLOGY

Gulf-RT-10482

STUDY OF RADIATION EFFECTS IN SILICON SOLAR CELLS Final Report

**B. C. Passenheim, R. A. Berger, J. F. Colwell,
and J. A. Naber**

**Prepared for
Jet Propulsion Laboratory
Pasadena, California 91103
under
Contract 952387
Gulf Radiation Technology Project 6105**

January 29, 1971

**GULF RADIATION TECHNOLOGY
A DIVISION OF GULF ENERGY & ENVIRONMENTAL SYSTEMS COMPANY
P.O. BOX 608, SAN DIEGO, CALIFORNIA 92112**

ABSTRACT

Radiation effects in lithium-diffused bulk silicon have been studied to ascertain the nature of the defects responsible for the degradation in output of silicon devices (solar cells) irradiated by space radiation. Minority-carrier lifetime temperature dependence measurements were performed before and after irradiation with 30-MeV electrons and fission neutrons. For low fluences of 30-MeV electrons, the lifetime degradation constant

$$K = \frac{\Delta 1/\tau}{\Delta \Phi} \simeq 6 \times 10^{-8} \text{ cm}^2/\text{e-sec}$$

for lightly diffused silicon ($n(\text{Li}) \leq 10^{15}/\text{cc}$) was the same as phosphorus-doped silicon of comparable donor density. The degradation constant for lithium-rich silicon ($n(\text{Li}) \geq 10^{16}/\text{cc}$) was almost twice as great. The degradation constant in lithium-diffused samples did not depend on oxygen for 30-MeV electron irradiations, but for fission neutrons the minority-carrier lifetime in oxygen-rich quartz-crucible (QC) silicon degraded at least twice as fast ($1.6 \times 10^{-5} \text{ cm}^2/\text{n-sec}$) as in oxygen-lean float-zone (FZ) silicon. The initial recombination center introduction rate seems to be the same at all temperatures between 110° and 300°K, but because of the temperature dependence of the capture cross section, the degradation constant increases with decreasing temperature. The degradation constant was found to decrease with extended fluences.

Recombination centers located more than 0.3 eV from a band edge were produced by 30-MeV electron irradiations in both FZ and QC silicon. In addition to the deep centers, centers near ($E_c - 0.17$) eV were observed in FZ silicon both before and after irradiation. Lifetimes at and above room temperature reflect recombination through the deep centers, which were observed to anneal by first-order kinetics. For electron irradiations, activation energies of 0.80 ± 0.10 and 1.0 ± 0.2 eV were found for FZ and QC silicon, respectively. The 0.17-eV center annealed much

more slowly. Effective frequency factors ranged from about 10^6 to nearly 10^{10} sec^{-1} as the lithium donor density increased from about 4×10^{14} to almost $3 \times 10^{16}/\text{cc}$. One-hour anneals at 390°K caused more than 80% lifetime recovery at low fluences, but at high fluences trapping centers were seen which could not be removed by thermal anneal. These annealing characteristics suggest migration of lithium to the defect center as the annealing mechanism.

About 95% of the neutron-induced recombination centers thermally annealed between 300° and 400°K . The anneal was clearly first-order, with an activation energy of $0.67 \pm 0.05 \text{ eV}$ for FZ silicon. Assuming first-order annealing, an activation energy of $1.2 \pm 0.6 \text{ eV}$ was found for QC silicon. These activation energies suggest annealing results from migration of lithium to the recombination center.

For 30-MeV electron irradiations at 300°K , an electron-spin resonance investigation showed that the introduction rate of the oxygen-vacancy (Si-B1) center ranged from the normal rate of $(\frac{\Delta n}{\Delta \Phi} = 0.15 \pm 0.05 \text{ cm}^{-1})$ in lightly diffused ($10^{16}/\text{cc}$) silicon to less than $(0.025 \pm 0.010) \text{ cm}^{-1}$ in lithium-rich ($4 \times 10^{17}/\text{cc}$) QC silicon. On thermal anneal, the electrical conductivity, LiO^+ density, and Si-B1 density all decreased between 320° and 380°K . In nondiffused silicon, the Si-B1 center anneals above 550°K .

For phosphorus-doped lithium-diffused float-zone and quartz-crucible silicon irradiated at or below 150°K , to fluences of $\sim 10^{17} \text{ e/cm}^2$ the phosphorus-vacancy (Si-G8) introduction rate $(\frac{\Delta n}{\Delta \Phi} = 0.16 \pm 0.05 \text{ cm}^{-1})$ was the same as for silicon which contained no lithium. LiO^+ resonances were observed before irradiation but disappeared on irradiation. The Si-G8 center thermally annealed between 425° and 475°K , as it does in nondiffused silicon. More than $10^{15}/\text{cc}$ unidentified centers remained after a 15-minute anneal at 600°K .

Infrared absorption measurements indicate the introduction rate of the divacancy (Si-G7) center is comparable for electron-irradiated lithium-diffused ($5 \times 10^{16} \text{ Li/cc}$) and nondiffused silicon at electron fluences of $\sim 10^{17} \text{ e/cm}^2$. Sample temperatures were kept below 150°K during and after

irradiation. The divacancy anneals at or below 300°K in diffused silicon, compared with 325° to 575°K in nondiffused silicon. As the 1.8- μ m divacancy band disappears, new bands near 1.4 and 1.65 μ m appear, and these anneal near 600°K.

Although measurements under this contract were done on bulk silicon diffused with lithium, the desired ultimate goal is an operating device—namely, a solar cell—that is resistant to radiation damage. Therefore, in addition to measuring changes in the electronic properties of bulk materials due to damaging radiation and annealing, it is important to be able to predict the effect of such changes on the device performance. To achieve this goal, a computer code called PN has been applied to generate solar cell current-voltage (I-V) output. This code can be used to predict the steady-state I-V characteristics of solar cells with arbitrary doping profiles, spectral light intensity, nonuniform radiation damage, etc. It can include the degradation of carrier lifetimes with radiation fluence and the annealing of this damage with time.

In this report, the theory and operation of this code are briefly discussed. It is shown that the code generates accurate I-V curves for a realistic N-on-P diffused-junction solar cell geometry. It is shown that results from the PN code for a step-junction solar cell agree with the predictions of a simplified analysis. This gives confidence that the code can be used for more complex (and realistic) junctions which cannot be directly analyzed. Finally, the code is applied successfully to the complicated problem on nonuniform radiation damage from low-energy protons. Computer predictions of cell output versus proton fluence are shown to be quite close to measured results.

CONTENTS

ABSTRACT	2
1. INTRODUCTION	9
2. IRRADIATION FACILITIES	13
3. SAMPLE PREPARATION	14
4. STUDY OF MINORITY-CARRIER LIFETIME	16
4.1 Introduction	16
4.2 Minority-Carrier Lifetime Measurement Techniques	16
4.2.1 Photoconductivity Decay	16
4.2.2 Steady-State Photoconductivity	16
4.3 Experimental	17
4.3.1 Samples	17
4.3.2 Sample Chambers	18
4.4 Minority-Carrier Lifetime Recombination Theory	18
4.5 Minority-Carrier Lifetime Measurements	24
4.5.1 30-MeV Electron Irradiations in Heavily Diffused FZ Silicon	26
4.5.2 30-MeV Electron Irradiations in Lightly Diffused FZ Silicon	27
4.5.3 30-MeV Electron Irradiations in Heavily Diffused QC Silicon	30
4.5.4 30-MeV Electron Irradiations in Lightly Diffused QC Silicon	32
4.5.5 Neutron Irradiations of Lithium-Diffused FZ Silicon	44
4.5.6 Neutron Irradiations of Lithium-Diffused QC Silicon	45
4.6 Conclusions	53
4.6.1 30-MeV Electron Irradiations	53
4.6.2 Fission Neutron Irradiations	55
5. STUDY OF SPECIFIC RADIATION-INDUCED DEFECTS	57
5.1 Electron-Spin Resonance	57
5.1.1 Introduction	57
5.1.2 Samples	60
5.1.3 Results of ESR Measurements	61
5.1.4 Conclusions	67
5.2 Infrared Absorption Studies	68
6. USE OF COMPUTER PN CODE FOR PREDICTING PERFORMANCE OF SILICON SOLAR CELLS	72
6.1 Introduction	72
6.2 Description of PN Code	74
6.3 Application of Code to a Typical Solar Cell	77
6.4 Dependence of Electrical Output on Physical Parameters	80
6.4.1 Calculation of Open-Circuit Voltage, V_{oc}	80
6.4.2 Short-Circuit Current	85
6.5 Computer-Simulated 300-keV Proton Damage	85
6.6 Conclusions	93

CONTENTS (Cont.)

7. OTHER WORK	95
8. SUMMARY OF CONCLUSIONS	96
8.1 Minority-Carrier Lifetime	96
8.1.1 30-MeV Electron Irradiations	96
8.1.2 Fission Neutron Irradiations	99
8.2 Electron-Spin Resonance	99
8.3 Infrared Absorption	100
8.4 Computer Simulation of Solar Cell	100
9. RECOMMENDATIONS FOR FUTURE WORK	102
10. NEW TECHNOLOGY	105
11. PUBLICATIONS AND PRESENTATIONS	106
REFERENCES	107

FIGURES

1. Preirradiation electrical conductivity and Hall coefficient of lithium-diffused float-zone silicon	19
2. Apparatus for measuring lifetime and resistivity as a function of neutron fluence	20
3. Variable-temperature (50° to 500°K) cryostat used to make electrical and optical measurements	21
4. Recombination cross section in silicon versus temperature	25
5. Inverse temperature dependence of minority-carrier lifetime in an 11-ohm-cm lithium-diffused silicon sample exposed to 30-MeV electrons at 300°K	28
6. Temperature dependence of minority-carrier lifetime for 30-MeV electron-irradiated lightly-diffused FZ silicon	29
7. Minority-carrier lifetime degradation constant for lithium-diffused silicon versus temperature of irradiation and measurement	31
8. Temperature dependence of minority-carrier lifetime for 60-ohm-cm QC silicon (not lithium-diffused)	33
9. Temperature dependence of minority-carrier lifetime for a 2-ohm-cm lithium-diffused QC silicon sample, before and after irradiation with 2.7×10^{12} e/cm ² 30-MeV electrons at 300°K and after a 25-minute anneal at 385°K	34
10. Inverse minority-carrier lifetime versus 30-MeV electron fluence for a 2-ohm-cm QC silicon sample irradiated at 300°K; isochronally annealed at 385° to 390°K for 25 to 30 minutes	36
11. Inverse minority-carrier lifetime versus 30-MeV electron fluence for lithium-diffused n-type QC silicon irradiated at 300°K	37
12. Lifetime degradation constant versus majority-carrier concentration for FZ and QC n-type silicon irradiated with 30-MeV electrons at 300°K	38

FIGURES (Cont.)

13.	Temperature dependence of minority-carrier lifetime for a 2-ohm-cm oxygen-containing lithium-diffused silicon sample, before and after irradiation with 2.7×10^{12} e/cm ² 30-MeV electrons at 112°K, and after a 30-minute anneal at 390°K	39
14.	Unannealed fraction of annealable recombination centers versus annealing time after 30-MeV electron irradiation of lithium-diffused n-type QC silicon irradiated at 300°K	40
15.	Unannealed fraction of annealable defects after 5-minute isochronal anneals at indicated temperatures after 30-MeV irradiation of lithium-diffused n-type QC silicon irradiated at 300°K	42
16.	Minority-carrier lifetime versus $1000/T$ of lithium-diffused n-type QC silicon	47
17.	Degradation of inverse lifetime of lithium-diffused n-type QC silicon at 280°K as a function of neutron fluence	48
18.	Unannealed fraction of annealable defects in lithium-diffused FZ and QC n-type silicon, measured at 280°K, versus isochronal anneal temperature, after APFA irradiation	49
19.	Isothermal anneal of lithium-diffused n-type QC silicon after APFA irradiation	50
20.	Minority-carrier lifetime temperature dependence of a 2-ohm-cm lithium-diffused QC silicon sample before and after neutron irradiation of about 1×10^{10} n/cm ²	52
21.	Resistivity of electron-irradiated lithium-diffused silicon versus 295°K storage time	64
22.	Resistivity after 15-minute isochronal anneals for lithium-diffused electron-irradiated silicon	65
23.	Density of paramagnetic centers after 15-minute isochronal anneals for lithium-diffused, phosphorus-doped, electron-irradiated silicon	66
24.	Divacancy model	69
25.	Relative transmission of high-purity FZ (10^4 -ohm-cm) and high-purity lithium-diffused FZ silicon after irradiation with 30-MeV electrons at <150°K	70
26.	Measured I-V curve compared with cell simulated by PN code; both cells graded junction in AM1 sunlight	79
27.	Diagram showing relative energies of carriers across an n/p solar cell junction	81
28.	V_{oc} versus g for run 310.1	83
29.	Variation of open-circuit voltage, V_{oc} , with minority-carrier lifetime in the base, τ_n	84
30.	Variation of short-circuit current, I , with minority-carrier lifetime, τ , where $L = \sqrt{30\tau}$ cm	86
31.	Current-voltage curves of a graded-junction cell degraded by 300-keV protons to fluences as marked on curves	91
32.	Normalized short-circuit current, I_{sc}/I_0 , versus proton fluence, Φ (protons/cm ²)	92

TABLES

1. History of Previous Work	58
2. Samples Used in ESR Studies	62
3. Annealing History of Samples Used in Divacancy Study	71
4. Input Parameters for PN Code Step Junction Cell	82
5. Range Versus Energy for Low-Energy Protons in Silicon	87
6. Distribution of Defect Recombination Centers as a Function of Fluence of 300-keV Protons in an Unshielded Solar Cell. .	89

1. INTRODUCTION

The overall purpose of this program was to ascertain the nature of the defects responsible for the degradation in output of silicon devices (solar cells) irradiated by space radiation. When the nature of the defects and their annealing mechanisms are known, it will be possible (1) to determine the parameters that will lead to development of radiation-hardened devices, (2) to predict the effects of radiation and annealing on solar cells, and (3) to make use of computer programs to predict radiation effects in solar cells on extended space flights.

The present effort was concentrated on the study of the effects of lithium on the production and annealing of damage in silicon. This work was performed on lithium-diffused bulk silicon using measurements including conductivity, Hall effect, minority-carrier lifetime, electron-spin resonance (ESR), electrical conductivity, and infrared absorption. The temperature range from 77.5° to 400° K was investigated. The damage was introduced by 30-MeV electrons and fission neutrons ($E > 10$ keV). Thirty-MeV electrons produce defects similar to those produced by high-energy protons.

In recent years, investigators at Gulf Radiation Technology (Rad Tech)* and elsewhere have carried out basic research programs in an attempt to determine whether the degradation is caused by primary radiation-induced defects or by an association of these primary defects with impurities. The annealing properties of these defects have also been studied. In these programs, lithium-diffused silicon solar cells have shown promise of being superior to other types of silicon solar cells in a radiation environment.

There are two approaches to determining the feasibility of using lithium-diffused silicon solar cells in space applications. One is the direct approach, in which the output characteristics of the cells are

* Formerly Defense Sciences Department of Gulf General Atomic Incorporated.

measured as a function of type of irradiation particle, fluence, lithium concentration, time, and temperature. This approach is time-consuming, since it requires long-term experiments to measure the cell output characteristics after an irradiation. In addition, the number of parameters to be studied and the various environments to be considered make this approach cumbersome. Furthermore, solar cell development progresses so rapidly that, by the time testing is complete, the cells often are considered obsolete by the manufacturer. The second approach is the basic-mechanisms approach. Its objective is to obtain an understanding of the physical, microscopic natures of the defects and their annealing. Once these are understood, the response of the cells in various environments can be predicted. This understanding can also lead to recommendations for improving the performance of the cells in an irradiation environment. The basic-mechanisms approach can complement the direct approach by suggesting experiments and pointing out important parameters that may otherwise have been overlooked. Used together, the two approaches minimize the need for long-term experiments.

In the basic-mechanisms approach, data from silicon solar cells are sometimes difficult to interpret because of problems inherent in the use of lithium-diffused silicon solar cells. These problems include high field effects in the depletion region; large concentration gradients of lithium near the junction (i.e., the actual lithium concentration within a diffusion length of the junction); effects of irradiation on contacts; and aging of contacts. Therefore, at Gulf Rad Tech we have concentrated on the electrical properties of bulk lithium-diffused silicon, measuring the effects of irradiation with 30-MeV electrons and fission neutrons and subsequent annealing behavior. Special emphasis has been placed on minority-carrier lifetime measurements, since solar cell efficiency depends strongly on this parameter.

Minority-carrier lifetime measurements supply information about the nature of the recombination centers. Lifetime studies in lithium-diffused silicon for preirradiation and postirradiation and preanneal and post-anneal conditions indicate recombination center densities and energy

levels and their annealing characteristics. These studies have been carried out for samples with varied lithium and oxygen concentrations and at various temperatures.

Electron-spin resonance (ESR) measurements yield additional detailed information about radiation-induced defects which may be responsible for lifetime degradation. Under favorable conditions, this technique may specifically identify the centers observed in minority-carrier lifetime studies. The ESR technique was previously used to study the production and annealing of the oxygen-vacancy (Si-B1), the divacancy (Si-G7), and the phosphorus-vacancy (Si-G8) centers in lithium-diffused silicon. In the present investigation, optical techniques were applied to the divacancy study, and the ESR study of the phosphorus-vacancy was completed.

Infrared (IR) absorption techniques have been used to augment the findings of ESR measurements of the divacancy. Infrared absorption measurements are less sensitive than ESR measurements, but unlike ESR can generally be used to observe defects regardless of their charge state. The presence or absence of oxygen in samples was checked by IR techniques.

Electrical resistivity measurements were used to determine the lithium concentration and to help determine the position of the Fermi level for the ESR and minority-carrier lifetime studies. Donor density estimates based on resistivity measurements were periodically corroborated by Hall effect measurements.

The program amassed a considerable amount of experimental evidence on production and anneal of radiation damage in bulk silicon of various lithium, phosphorus, and oxygen concentrations at various temperatures. Both high-energy electrons and fission neutrons have been used as irradiation sources. Minority-carrier lifetimes indicate the energy levels and recombination center production rates. Electron-spin resonance and infrared absorption measurements have supplied information on the production and anneal of certain specific defects.

The incentive for collecting this information is to attempt to (1) understand the specific nature of the radiation-induced damage and

its relationship to lithium content, and (2) to apply this information to the case of a lithium-diffused solar cell exposed to space radiation.

To accomplish the second objective, a computer program has been generated which calculates the current-voltage output of a solar cell when input parameters are supplied such as the spectral intensity of the illumination and the initial details of the cell construction (i.e., junction depth, doping profiles, carrier lifetimes, etc.). Further, the effects of radiation damage and thermal anneal can be simulated and the solar cell output recalculated for cells in various stages of degradation and recovery. Experimentally determined degradation and annealing rates of bulk silicon supply the information required by the code to simulate degraded and annealed cells. This code shows great potential for supplying quantitative predictions of solar cell output for any variety of cell constructions and ambient conditions. Judicious use of the code could considerably reduce the number of cells and variety of experimental conditions currently required to establish the response of cells exposed to real or simulated space radiation.

To show the worth of this code, it has been applied to the initial and degraded output of a typical N-on-P solar cell exposed to proton irradiation.

2. IRRADIATION FACILITIES

Most of the irradiations for the present program were performed at the Gulf Rad Tech electron linear accelerator (Linac) facility. This facility contains an L-band traveling-wave electron accelerator capable of producing electrons with energies between 3 and 45 MeV, pulse widths from 0.01 to 5 μ sec, and peak currents of approximately 700 mA. This machine was used both as the source of displacement radiation and as the ionizing radiation source needed to obtain excess carriers in the lifetime experiments. The intensity and pulse widths were reduced for the ionization pulses to minimize displacement damage that would occur as a result of these pulses.

A second source of ionizing pulses for the lifetime experiments was a Rad Tech flash X-ray. This machine delivers a 120-nsec pulse of 600-keV X-rays. For samples with lifetimes greater than 20 μ sec, a Xenon strobe light was also used to inject carriers.

The Gulf Rad Tech Accelerator Pulsed Fast Assembly (APFA) was one fission neutron source for minority-carrier lifetime studies. The APFA is a 7-in.-diameter uranium (93% U^{235}) unreflected fast reactor which can be operated as either a steady-state reactor or a repetitively pulsed (up to 720 pps) subcritical fast neutron source. The APFA offers easy accessibility for positioning of test samples, greatly facilitating in situ measurements. Samples may be located inside a 3/4-in.-diameter hole in the reactor or adjacent to the core. Once the test samples are in position, the reactor is brought to the desired reactivity configuration and (if desired) pulsed.

Two other neutron sources employed were the Gulf General Atomic TRIGA reactor and a Fansteel and uranium target (3-in.-dia.) (γ, n) neutron source. The latter was used in conjunction with the Linac, using Bremsstrahlung from 40-MeV electrons to initiate the (γ, n) reaction. In-situ measurements were not attempted with either of these neutron sources.

3. SAMPLE PREPARATION

In the initial work with lithium-diffused silicon performed by Gulf Rad Tech,⁽¹⁾ samples were prepared by NASA/Goddard; Centralab, Semiconductor Division, Globe Union, Inc.; and Radio Corporation of America. Subsequently, in order to save time and ensure that our sample requirements were met, we produced our own lithium-diffused samples. Silicon was diffused by two techniques: lithium-oil paint-on and lithium-tin bath diffusion. Details of these diffusion techniques have been presented previously.⁽²⁾

The same diffusion techniques were used to prepare the samples investigated in this reporting period. In addition to these two techniques, a third technique was employed using lithium-aluminum hydride in ether as a diffusion source.⁽³⁾

As previously reported,⁽²⁾ the probability of obtaining a uniform lithium donor density was less using the lithium-oil diffusion than by other techniques. However, the paint-on process is so convenient to use, when attempting to make a small number of samples of a particular donor density, that we continued to rely heavily on this process. After diffusion and redistribution, lithium donor density was established by measuring resistivity profiles by a four-probe technique. The experimental uncertainty, or measurement-to-measurement scatter using the four-probe apparatus, is estimated to be $\pm 12\%$. In this process, the resistivity was measured at various points across the front and back surfaces of the diffused and redistributed 2-mm-thick slabs. Samples which showed nonuniformities greater than about 20% were discarded. If a sample appeared to be of uniform resistivity, a portion of the sample was thinned in 0.25 mm increments by lapping or sawing off one side, and the resistivity of each side was remeasured. The measured resistivity was corrected for the diminishing sample thickness according to the method of Valdes.⁽⁴⁾ Samples showing nonuniformities greater than about 20% across their thickness were also discarded.

Finally, the lithium donor density was estimated from the measured four-probe resistivity using data by Irvin,⁽⁵⁾ and compared to either the resistivity of a completed sample, or to the Hall coefficient of a completed sample, or both. Thus, the lithium donor density is thought to be uniform to within 20% for every sample. This rather tedious evaluation procedure would be intolerable in a manufacturing operation, but was acceptable for making the small batch-lots required for this research program.

4. STUDY OF MINORITY-CARRIER LIFETIME

4.1 INTRODUCTION

Minority-carrier lifetime measurements have been studied for several reasons. First, changes in minority-carrier lifetimes due to radiation-induced defects can be observed at very low fluence levels (approximately 10^{12} e/cm²), making these measurements some of the most sensitive measurements available. Second, the temperature dependence of minority-carrier lifetime establishes the density and energy levels of recombination centers. Third, the solar cell output can be related to the minority-carrier lifetime (τ). A discussion of the relationship between solar cell performance and minority-carrier lifetime is presented in Section 6 of this report.

4.2 MINORITY-CARRIER LIFETIME MEASUREMENT TECHNIQUES

The minority-carrier lifetimes were measured by two techniques. The first was the standard photoconductivity decay method, and the second was the steady-state photoconductivity method.

4.2.1 Photoconductivity Decay

The photoconductivity decay technique is described in Ref. 1. Three penetrating carrier-injection sources were employed: a filtered Xenon strobe light, a 600-keV flash X-ray, and a low-level, 0.1- μ sec pulse of 30-MeV electrons. Carrier-injection levels of less than 1% were generally used. The same preirradiation, low-injection-level lifetime was measured using all three injection sources. Photodecay signals were observed on an oscilloscope and photographed. When necessary, these data were reduced by a computer calculation, as previously described.⁽⁶⁾

4.2.2 Steady-State Photoconductivity

The steady-state photoconductivity technique was used for the neutron irradiation experiments and some of the electron irradiation experiments.

For these measurements, minority carriers were injected with a tungsten-filament light source which was chopped by a toothed wheel at 10^3 Hz before passing through a lens system, water, gallium arsenide and silicon filters. At equilibrium, the change in conductivity is $\Delta\sigma = g\tau e(\mu_n + \mu_p)$, where g is the generation rate of the light source and μ_n and μ_p are the electron and hole mobilities. The direct-current conductivity is $\sigma_0 = n_0 e \mu_n$. Thus, holding the sample current constant, one finds that

$$\left| \frac{\Delta V}{V} \right| = \frac{\Delta\sigma}{\sigma_0} = \frac{\Delta n}{n_0} = \frac{g\tau}{n_0} \left(\frac{\mu_n + \mu_p}{\mu_n} \right) . \quad (1)$$

The signal observed was dc voltage (V) modulated by a 10^3 -Hz chopped signal of amplitude $\Delta V = 10^{-3}$ V. From Eq. 1, it is clear that

$$\tau = \frac{n_0}{g} \left(\frac{\mu_n}{\mu_n + \mu_p} \right) \left| \frac{\Delta V}{V} \right| = A \left| \frac{\Delta V}{V} \right| . \quad (2)$$

The constant A was empirically determined for each sample by comparing the measured photodecay lifetime (τ) with the amplitude of the steady-state signal ($\Delta V/V$) at one or more temperatures. Characteristically, $A = 1$ to 3×10^{-2} sec, depending on the light intensity. Carrier-injection levels of less than 1% were used.

4.3 EXPERIMENTAL

4.3.1 Samples

Vacuum float-zone silicon samples used in these lifetime investigations were fabricated from 10^4 -ohm-cm n-type silicon. This high-purity material had a room temperature lifetime of about 10^3 μ sec before lithium diffusion. Quartz-crucible samples were lithium-diffused from 60-ohm-cm phosphorus-doped material which had an initial room-temperature lifetime in excess of 100 μ sec.

Thus, the density of recombination centers prior to diffusion was negligibly low. The samples were lithium-diffused by either the lithium-tin bath or one of the paint-on techniques. Lifetime samples were of the

standard four-lead configuration. Hall effect samples had an additional lead midway between the voltage leads, on the back of the sample. Gold preforms were ultrasonically tacked to $1.6 \times 1.6 \times 10$ mm samples and bonded by heating to 450°C for 7 min. Electrical leads of 0.002-in. copper were soft-soldered to the gold dots, and a copper-constantan thermocouple was cemented to one end of the sample with GE-7031 insulating varnish.

Figure 1 shows typical conductivity and Hall effect results on a lithium-diffused float-zone silicon sample. A donor density of $2.5 \times 10^{14}/\text{cc}$ was estimated from the room-temperature resistivity.⁽⁵⁾ The conductivity decrease with increasing temperature is attributed to the temperature dependence of lattice scattering.⁽⁷⁾

4.3.2 Sample Chambers

Samples were attached to headers which could be installed in either of the two variable-temperature chambers illustrated in Figs. 2 and 3. To inject carriers, a tungsten light source, lens, and chopper system was used in the steady-state minority-carrier lifetime measurements. The tungsten source and chopper could be replaced with a Xenon strobe lamp, 600-keV flash X-ray, or linear accelerator for photodecay measurements. When the injection source had to be filtered to remove nonpenetrating light, water, gallium arsenide, and silicon filters were used. In both chambers the silicon filter was mounted on the sample block so that it was always at the sample temperature. Thermocouples and resistance heaters were included to permit monitoring and adjusting of the temperature. The chamber in Fig. 3 fit between the pole pieces of an electromagnet and was used to make Hall effect measurements.

4.4 MINORITY-CARRIER LIFETIME RECOMBINATION THEORY

The theory of recombination of excess carriers has been treated by others,⁽⁸⁻¹⁰⁾ and the relation between theory and experimentally measured quantities has been reported earlier.^(1,2,11,12) The conclusions can be summarized as follows.

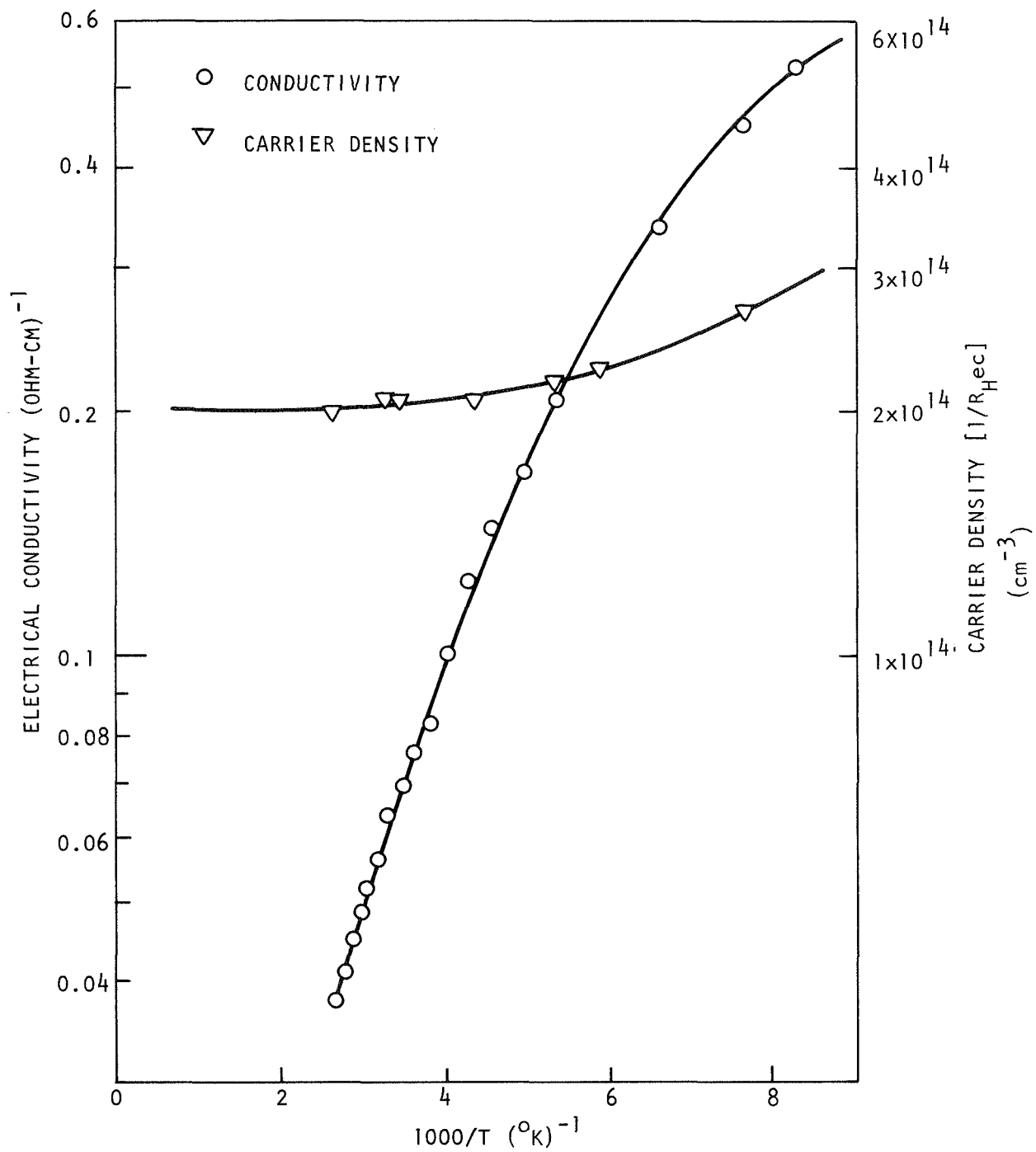


Fig. 1 Preirradiation electrical conductivity and carrier density of lithium-diffused float-zone silicon

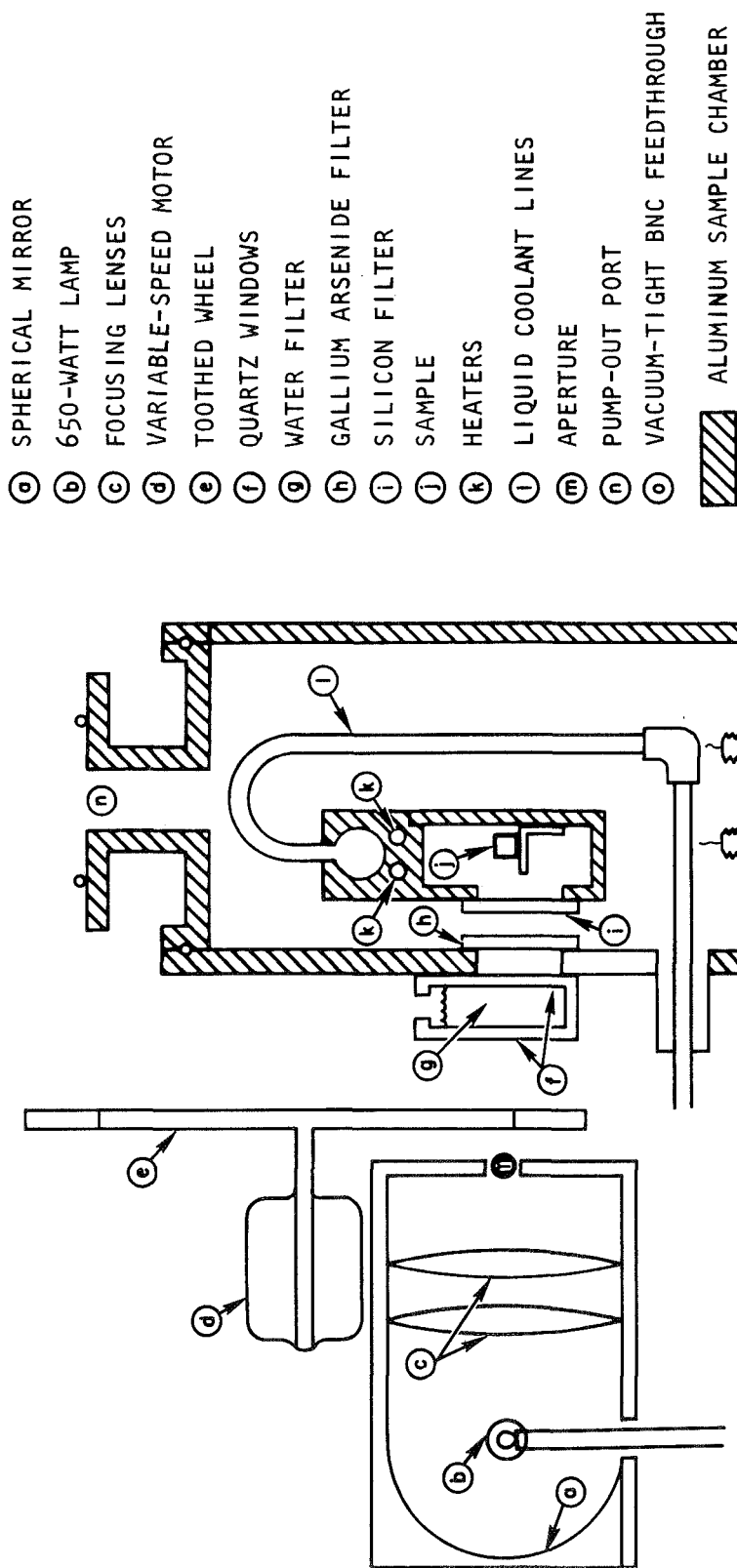


Fig. 2 Apparatus for measuring lifetime and resistivity as a function of neutron fluence
(not to scale)

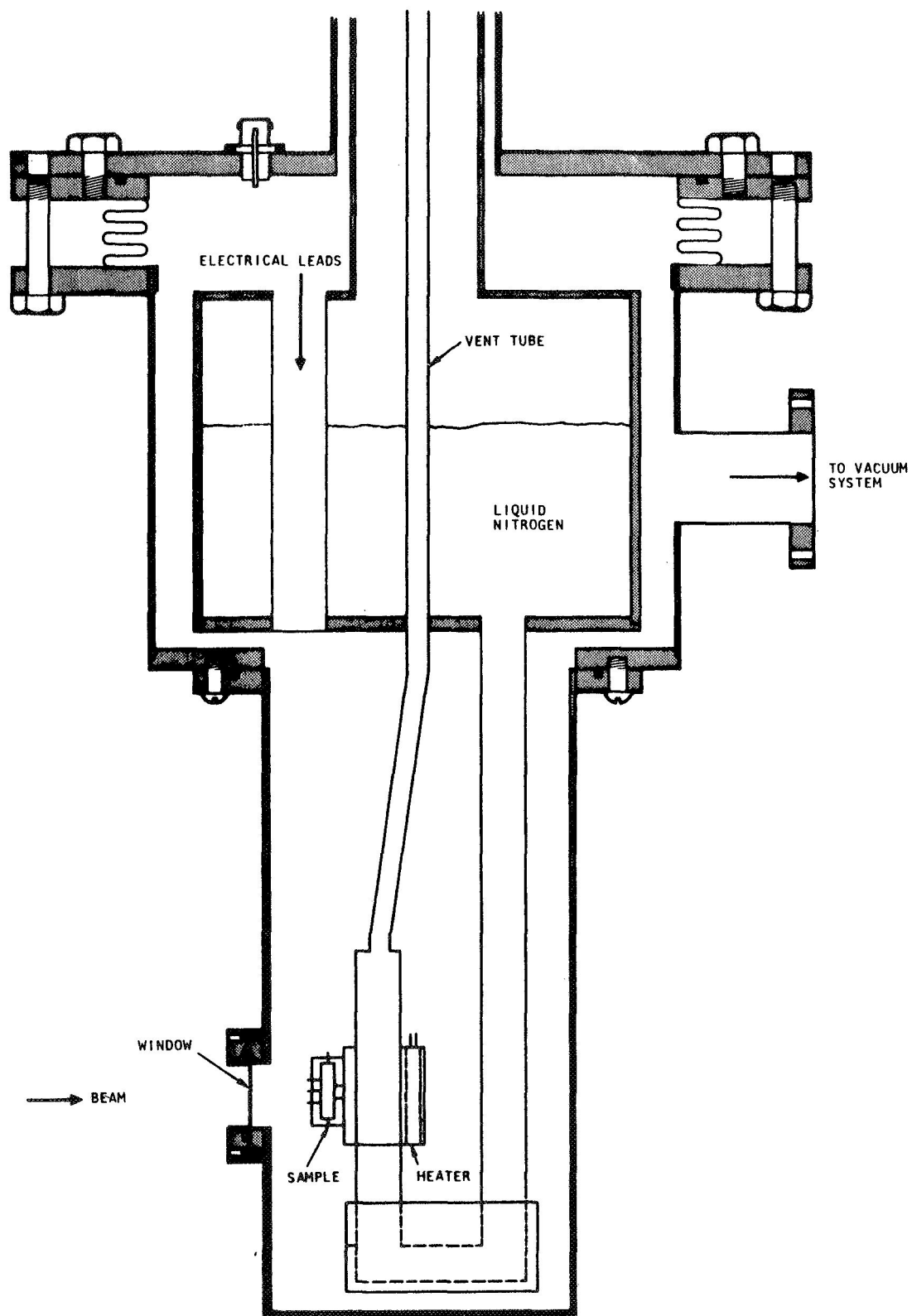


Fig. 3 Variable-temperature (50° to 500°K) cryostat used to make electrical and optical measurements

The Shockley-Read theory for a single-level defect assumes that the number of recombination centers is small relative to the excess-carrier density. This assumption implies that the excess electrons and holes have equal densities and lifetimes. The expression for the lifetime in this case is

$$\tau = \tau_{p_0} \left(\frac{n_0 + n_1 + \Delta n}{n_0 + p_0 + \Delta n} \right) + \tau_{n_0} \left(\frac{p_0 + p_1 + \Delta p}{n_0 + p_0 + \Delta n} \right), \quad (3)$$

where n_0 and p_0 are the thermal equilibrium electron and hole concentrations, n_1 and p_1 are the electron and hole concentrations calculated when the Fermi level is assumed to lie at the recombination center level, $\Delta n = \Delta p$ is the excess-carrier concentration, τ_{n_0} is the lifetime for electrons in highly p-type material, and τ_{p_0} is the lifetime for holes in highly n-type material. In n-type material (for p-type, n's and p's are interchanged), where $n_0 \gg p_0$, dividing by n_0 gives

$$\tau = \frac{\tau_{p_0} \left(1 + \frac{n_1}{n_0} \right) + \tau_{n_0} \left(\frac{p_1}{n_0} \right) + \frac{\Delta n}{n_0} (\tau_{p_0} + \tau_{n_0})}{1 + \frac{\Delta n}{n_0}} \quad (4)$$

or

$$\tau = \frac{\tau_\ell + \tau_h \left(\frac{\Delta n}{n_0} \right)}{1 + \frac{\Delta n}{n_0}} \quad (5)$$

where τ_ℓ (low-injection-level lifetime) and τ_h (high-injection-level lifetime) are the corresponding terms in the equations.

Our measurements were largely confined to low-injection-level measurements ($\Delta n/n_0 < 1\%$) in n-type material. The low-injection-level lifetime, $\tau_\ell = \tau_{p_0} (1 + n_1/n_0) + \tau_{n_0} (p_1/n_0)$, may be simplified in this limit for two special cases.

Case 1: When the recombination level (E_T) is closer to a band edge than the Fermi level (E_F), either

$$n_1 > n_0 > p_1 \quad \text{or} \quad p_1 > n_0 > n_1 ,$$

and

$$\tau \simeq \tau_{p_0} (1 + n_1/n_0) \quad \text{or} \quad \tau \simeq \tau_{n_0} (p_1/n_0) ,$$

where

$$n_1 = N_C \exp(E_T - E_C)/kT ,$$

$$p_1 = N_V \exp(E_V - E_T)/kT ,$$

where N_C and N_V are the conduction and valence band carrier densities. Forcing the Fermi level below the recombination level contributes an exponential factor to the lifetime temperature dependence.

Case 2: When the Fermi energy is well above the recombination center level,

$$n_0 \gg n_1 > p_1 ,$$

$$\tau \simeq \tau_{p_0} .$$

The temperature dependence of τ is found in terms containing τ_{p_0} , τ_{n_0} , n_1 , p_1 , and n_0 . The term n_0 is known, however, and can be extracted from the data. The temperature dependences of τ_{p_0} and τ_{n_0} are exhibited through the thermal velocity, V_{th} , of the carriers and the capture cross section, σ , where

$$\tau_{p_0} = \frac{1}{N_R V_{th} \sigma_p}$$

and

$$\tau_{n_0} = \frac{1}{N_R V_{th} \sigma_n},$$

and where N_R is the concentration of recombination centers.

Theoretical work on the temperature dependence of the cross section for neutral and attractive recombination centers has been performed by Leadon⁽¹²⁾ and Lax.⁽¹³⁾ A brief summary of Lax's theory is given in Ref. 14. Figure 4 gives the temperature dependence for the cross sections of the singly charged attractive center and the neutral center.

4.5 MINORITY-CARRIER LIFETIME MEASUREMENTS

The experimental study of the effects of radiation and annealing on the minority-carrier lifetime of lithium-diffused silicon was undertaken because minority-carrier lifetime is directly related to solar cell outputs. In this and previous programs,^(1,2) material parameters and experimental conditions were varied in an effort to obtain enough information to permit prediction of solar cell response for a variety of cell parameters and environments. Solar cells may be fabricated from oxygen-rich (quartz-crucible) or oxygen-lean (float-zone or Lopex) silicon.

The lithium donor density of a cell is spatially variable, and the temperature at which a cell operates depends on its mission or environment. The cell environment also determines the nature of the degrading radiation. Hence, we have attempted to determine the nature of the degradation and annealing characteristics of minority-carrier lifetime in bulk lithium-diffused silicon as a function of (a) oxygen content, (b) lithium donor density, (c) irradiation temperature, and (d) fluence.

During this contract period, the bulk of the experimental investigation was devoted to the study of high-energy electron and neutron damage in relatively low-lithium-density, oxygen-rich (quartz-crucible) and oxygen-lean (float-zone) bulk silicon. During previous investigations, reported in detail elsewhere,^(1,2) high-lithium-density quartz-crucible (QC) and high- and low-lithium-density float-zone (FZ) silicon were investigated. This section is organized as follows. First, our earlier

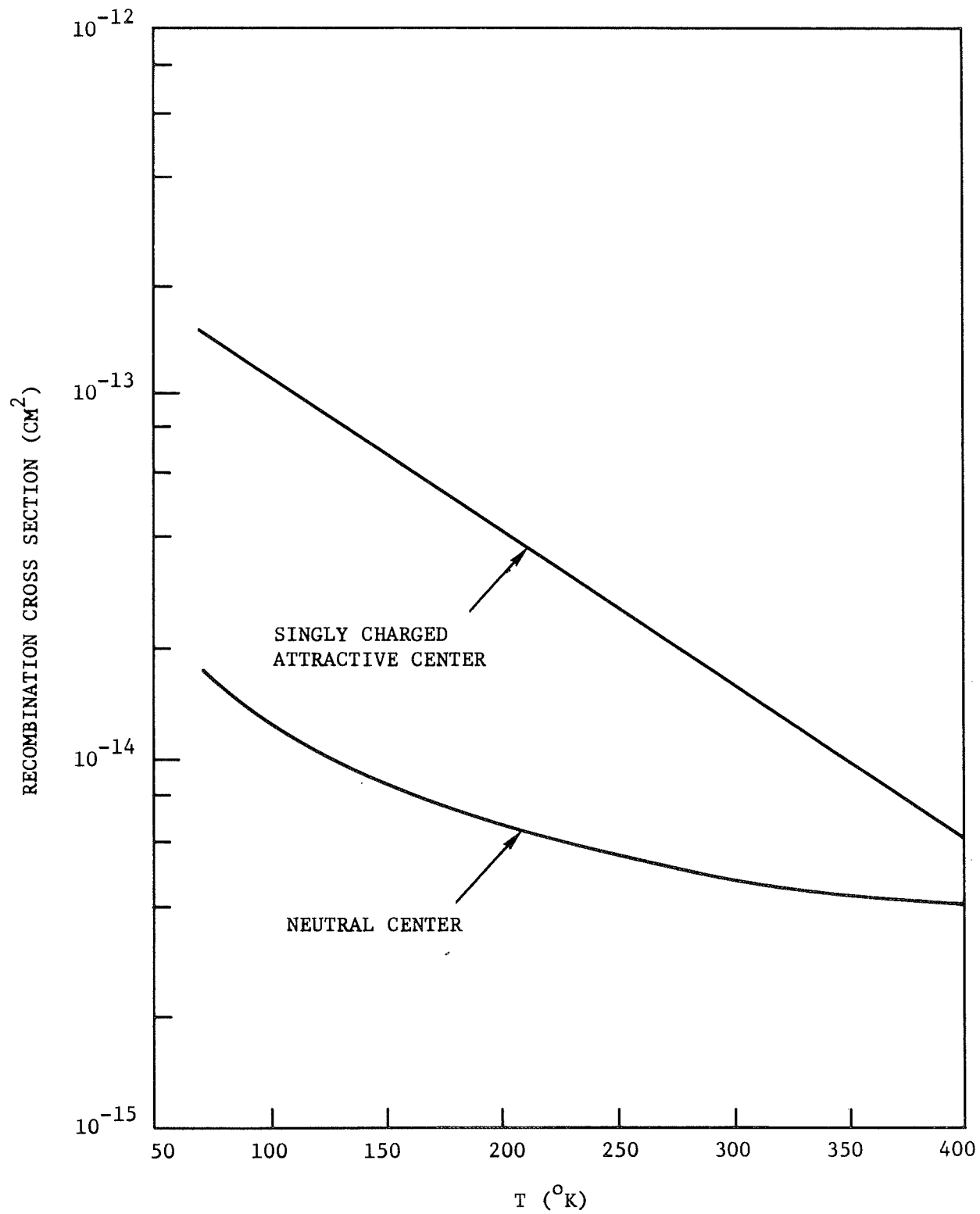


Fig. 4 Recombination cross section in silicon versus temperature

results on high- and low-density lithium-diffused electron-irradiated FZ silicon are summarized. Then prior results on high-lithium-density oxygen-rich material are reviewed. Finally, the results on lithium-lean oxygen-rich electron-irradiated silicon are presented.

After presenting the results of electron-irradiated silicon, we review prior measurements on neutron-irradiated silicon, and current results are presented.

4.5.1 30-MeV Electron Irradiations in Heavily Diffused FZ Silicon*

Several samples of 10^4 -ohm-cm high-purity float-zone silicon were lithium-diffused to lithium donor densities ranging from 1.5 to $\sim 5 \times 10^{16}$ /cc. Donor densities were determined by resistivity and Hall effect measurements. Experimental results on samples diffused by the NASA Goddard Space Flight Center and samples diffused by Gulf Rad Tech were in agreement. These samples all had preirradiation room-temperature minority-carrier lifetimes of less than $5 \mu\text{sec}$; hence, only room-temperature lifetime degradation rates were measured. At these high donor densities, the Fermi level can only be swept from about $(E_c - 0.03)$ eV at 77°K to about $(E_c - 0.2)$ eV near 400°K . An average minority-carrier lifetime degradation rate of $1.1 \pm 0.2 \times 10^7 \text{ cm}^2/\text{e-sec}$ was observed at room temperature for 30-MeV electron irradiations. This degradation rate is approximately twice that observed for phosphorus-doped silicon of equivalent donor density.** A study of the temperature dependence of minority-carrier lifetime indicated that the preirradiation lifetime was due to attractive centers more than 0.17 eV from a band edge and that the radiation-induced recombination center was probably neutral, located more than 0.17 eV from a band edge.

The results of isothermal and 5-minute isochronal anneals indicated the annealing kinetics were first-order, with the annealing stage centered near 320°K . An activation energy of $E = 0.85 \pm 10 \text{ eV}$ and a frequency factor of $\nu_0 \approx 10^{11} \text{ sec}^{-1}$ were deduced from these data. For fluences up to about 10^{13} e/cm^2 , the thermal anneal of minority-carrier lifetime was essentially complete.

*Results reported in detail in Ref. 1.

**Refer to Fig. 12.

4.5.2 30-MeV Electron Irradiations in Lightly Diffused FZ Silicon*

Several minority-carrier lifetime samples were fabricated from 10^4 -ohm-cm FZ silicon which had been lithium-diffused by either the lithium-oil paint-on or lithium-tin bath technique to lithium donor densities of from 3 to 5×10^{14} /cc. Initial minority-carrier lifetime degradation rates at room temperature were found to be ($K = 6 \pm 2 \times 10^{-8}$ cm²/e-sec), the same as for silicon of comparable donor density which contained no lithium.** A study of the minority-carrier lifetime temperature dependence provided evidence of two recombination centers, with one center (which could be either neutral or attractive) located about 0.17 eV below the conduction band and a second attractive center further than 0.35 eV from either band edge. These two centers were present before as well as after irradiation. At low temperatures, data on these samples might be still better described by assuming a third recombination center within 0.10 eV of the conduction band, where other investigators have reported centers.⁽¹⁵⁾ However, the initial minority-carrier lifetime near room temperature is almost entirely controlled by the deep centers, and the room-temperature degradation rate primarily reflects the production of radiation-induced deep centers. Isothermal anneals at temperatures in the 360° to 400°K range indicated first-order annealing kinetics with an activation energy of $E = 0.75 \pm 0.10$ eV and a frequency factor of $\nu \approx 10^6$ sec⁻¹.

Measuring the minority-carrier lifetime temperature dependence before and after irradiation with 30-MeV electrons and before and after various anneals indicated that the rapid first-order anneal is primarily due to the disappearance of the deep center. Typical results are shown in Figs. 5 and 6. The centers in the vicinity of ($E_c - 0.17$) eV were essentially unaffected by a one-hour anneal at 390°K, but were observed to decrease in number when the sample was stored near room temperature for a period of days (10 to 30 days).

Under heavy irradiation ($\Phi \gtrsim 4 \times 10^{13}$ e/cm²), trapping centers were observed after anneal which were unaffected by further anneals of up to 66 hours at 430°K.

*Reported in detail in Ref. 2.

**Refer to Fig. 12.

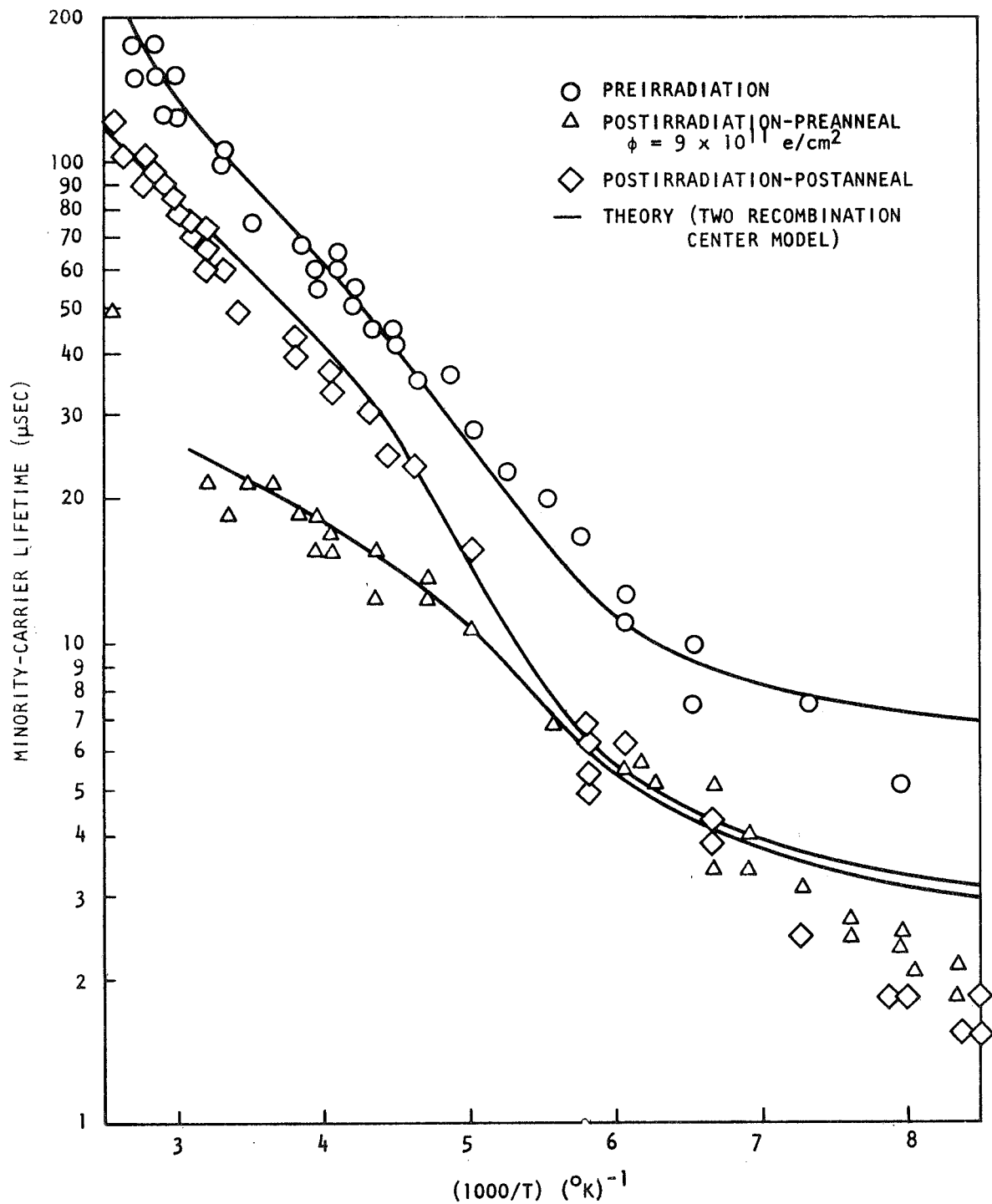


Fig. 5 Inverse temperature dependence of minority-carrier lifetime in an 11-ohm-cm lithium-diffused silicon sample exposed to 30-MeV electrons at 300°K

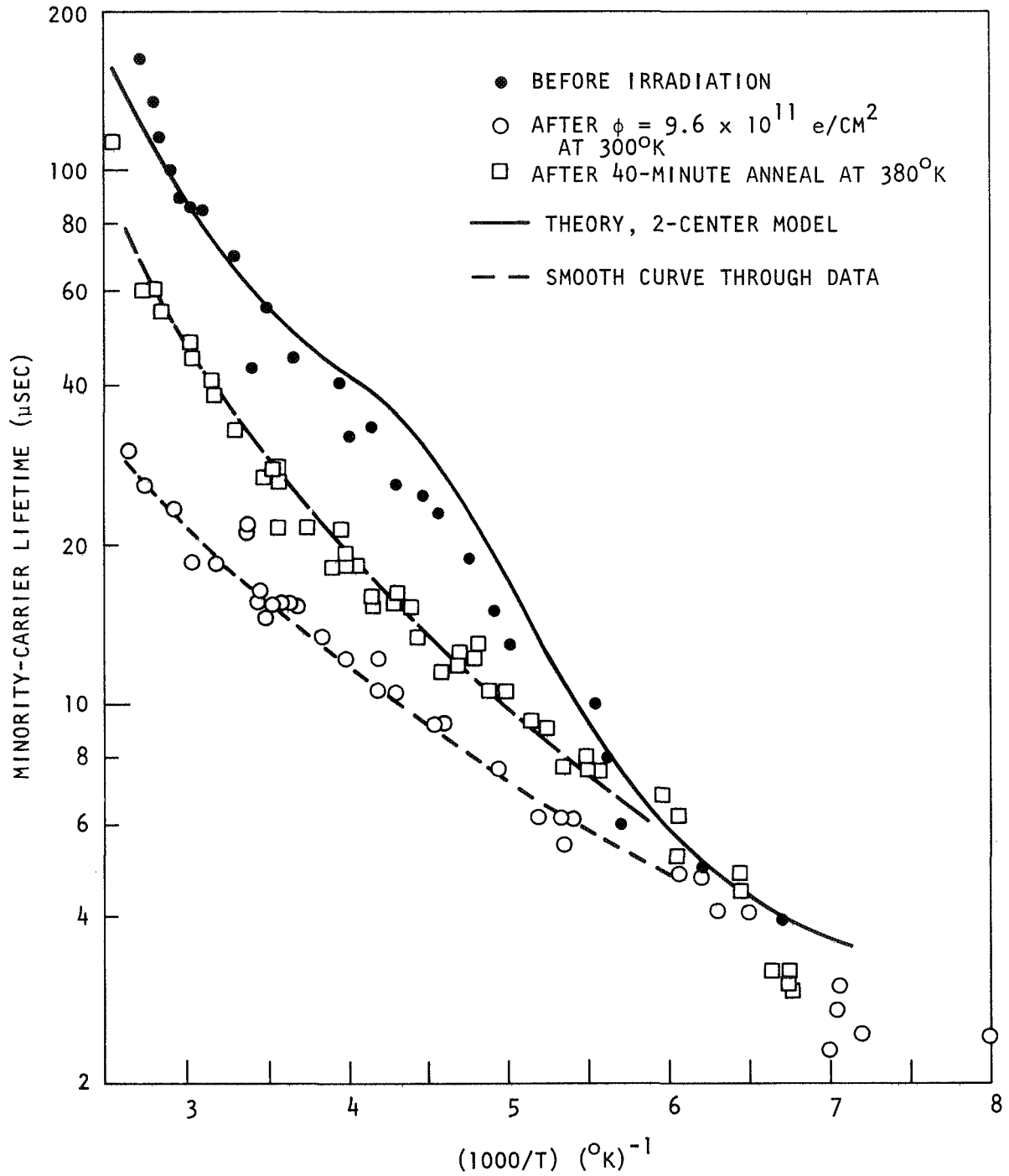


Fig. 6 Temperature dependence of minority-carrier lifetime for 30-MeV electron-irradiated lightly-diffused FZ silicon

The minority-carrier lifetime degradation rate was measured at temperatures between 115° and 300°K. The results of these measurements are shown in Fig. 7. The uncertainty is relatively high because the degradation rate varies by 30 to 50% from sample to sample and, for any given sample, depends on its previous irradiation and anneal history. Nevertheless, no irradiation temperature dependence of the recombination center introduction rate was noted, as evidenced by the absence of any anneal below room temperature. The degradation rate measured at about 115°K was close to ten times as great as that measured at 300°K. This difference is attributed to the temperature dependence of the recombination center's capture cross section,^(12,13) and implies that solar cells operated at temperatures below room temperature would degrade more rapidly than similar cells run at room temperature.

4.5.3 30-MeV Electron Irradiations in Heavily Diffused QC Silicon*

The primary differences between Czochralski-grown quartz-crucible (QC) and vacuum-float-zone (FZ) silicon is that QC silicon has an oxygen concentration one to two orders of magnitude higher than FZ silicon ($O(\text{FZ}) \lesssim 10^{16}/\text{cc}$, $O(\text{QC}) \gtrsim 10^{17}/\text{cc}$), while the dislocation density is much greater in FZ than in QC silicon.

Minority-carrier lifetime studies were performed on samples of 50-ohm-cm phosphorus-doped silicon which was lithium-diffused by Centralab Semiconductor Products to a lithium donor density of about $1 \times 10^{16}/\text{cc}$. Diffusion was by the paint-on technique. Preirradiation room-temperature minority-carrier lifetimes were approximately 6 μsec , dropping to about 1 μsec near 100°K. These lifetimes were too short to effectively measure degradation rates at reduced temperatures. The room-temperature minority-carrier lifetime degradation constant was the same as for heavily diffused FZ silicon or is independent of oxygen content ($K = 1.1 \pm 0.2 \times 10^{-7} \text{ cm}^2/\text{e-sec}$). This is twice as high as phosphorus-doped silicon of comparable donor density. The temperature dependence of the preirradiation minority-carrier lifetime was best described by a single attractive center, located more than 0.17 eV from either band edge. The high initial donor density

*Described in detail in Ref. 1.

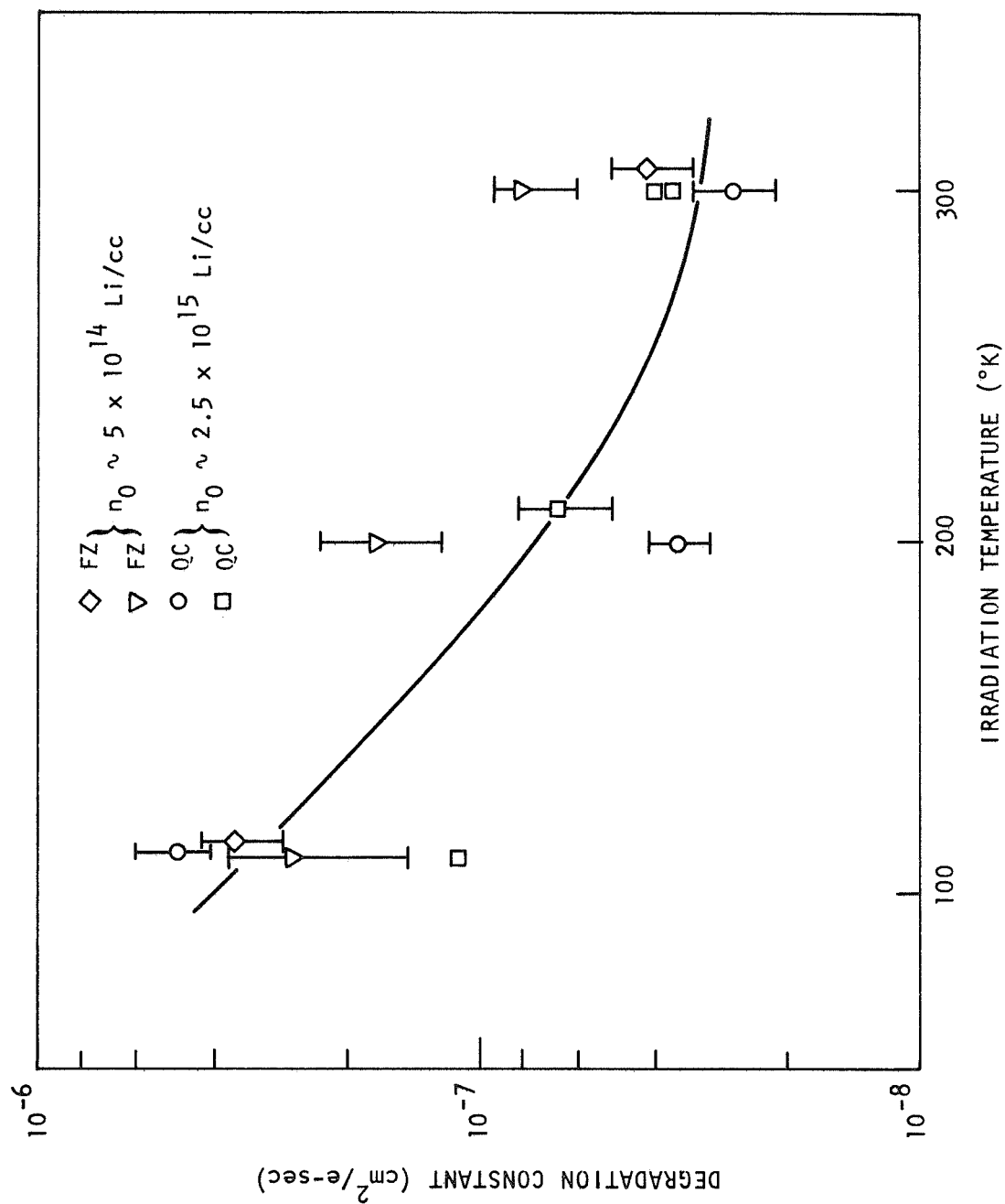


Fig. 7 Minority-carrier lifetime degradation constant for lithium-diffused silicon versus temperature of irradiation and measurement

prevented moving the Fermi level below about ($E_c - 0.2$) eV. Injection level dependence measurements tended to support the single-level assignment, both before and after irradiation with 30-MeV electrons. Comparing pre- and postirradiation minority-carrier lifetime temperature dependences suggested (with reservations imposed by experimental uncertainties) a neutral radiation-induced center more than 0.17 eV from a band edge. Isothermal anneals indicated first-order annealing kinetics. Five-minute isochronal anneals showed an annealing stage centered near 365°K.

Analysis of these anneals resulted in activation energy estimates of $E = 0.75 \pm 0.10$ eV and effective frequency factors of about 10^8 sec^{-1} . For fluences up to about 10^{13} e/cm^2 , complete recovery of minority-carrier lifetime was observed at all temperatures from 100° to 400°K.

4.5.4 30-MeV Electron Irradiations in Lightly Diffused QC Silicon

During this contract period, the bulk of the minority-carrier lifetime studies have been performed on 30-MeV electron-irradiated lithium-diffused high-purity QC silicon. A 60-ohm-cm silicon boule was purchased from Wacker Chemical Company.

Figure 8 shows the minority-carrier-lifetime temperature dependence of the starting material. Assuming a capture cross section as given by Lax,⁽¹³⁾ this temperature dependence indicates recombination due to about $4 \times 10^{10}/\text{cc}$ attractive centers farther than 0.4 eV from a band edge. Two-millimeter-thick slices of silicon were lithium-diffused by the lithium-oil paint-on technique and redistributed to a uniform donor density of about $2 \times 10^{15}/\text{cc}$, as determined by resistivity and Hall effect measurements. The resistivity of these samples was about 2 ohm-cm.

That the 60-ohm-cm material actually contained oxygen was verified by infrared absorption measurements of the 9- μm absorption band due to oxygen.⁽¹⁶⁾ Only a small 9- μm lattice band was observed in the 10^4 - and 0.4-ohm-cm FZ silicon previously used in lifetime and ESR measurements.

Figure 9 shows a family of curves of minority-carrier lifetime for the 2-ohm-cm lithium-diffused QC silicon versus temperature, including preirradiation, postirradiation, and postirradiation-postanneal measurements. These lifetime temperature dependences can be attributed to

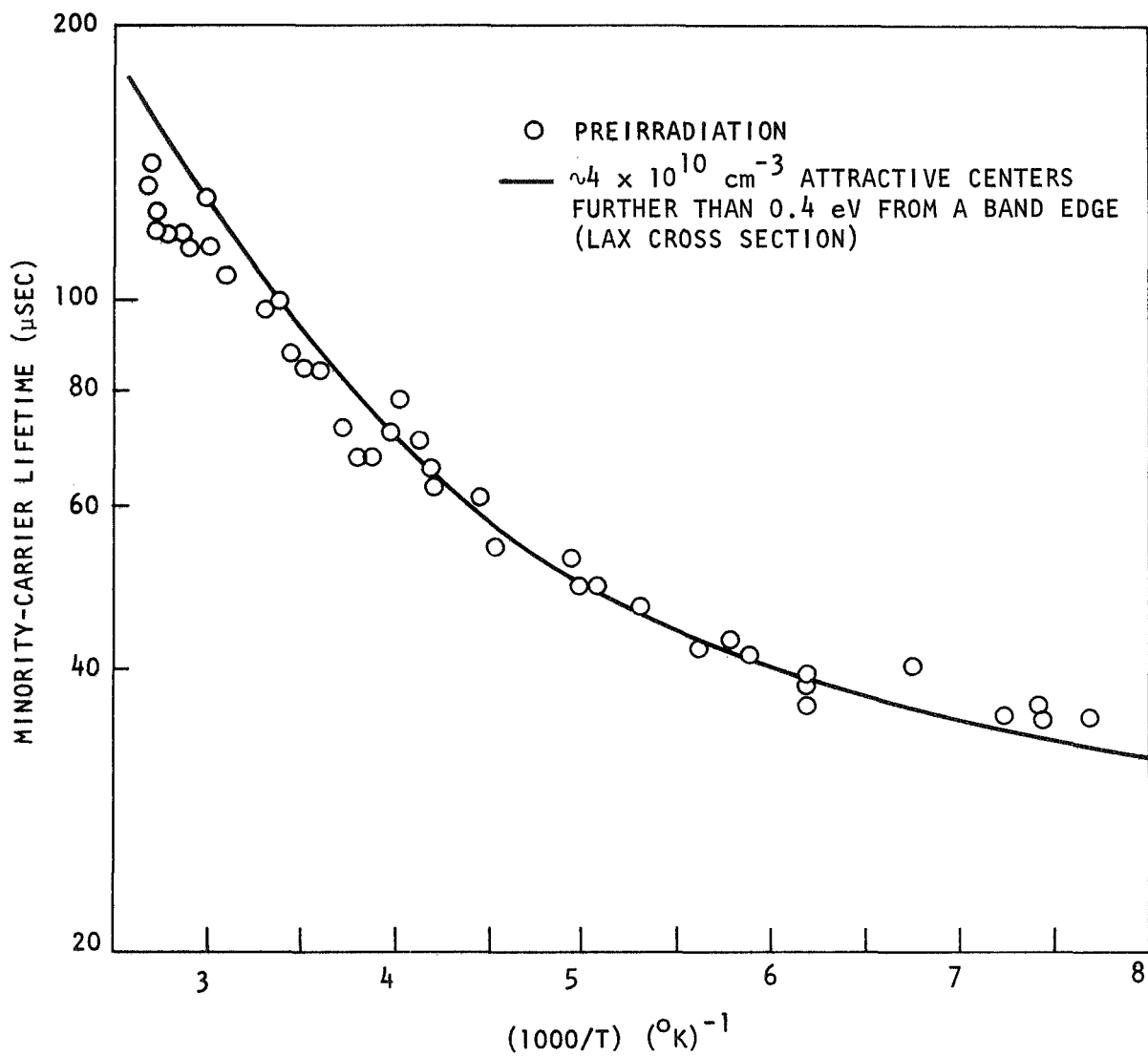


Fig. 8 Temperature dependence of minority-carrier lifetime for 60-ohm-cm QC silicon (not lithium-diffused)

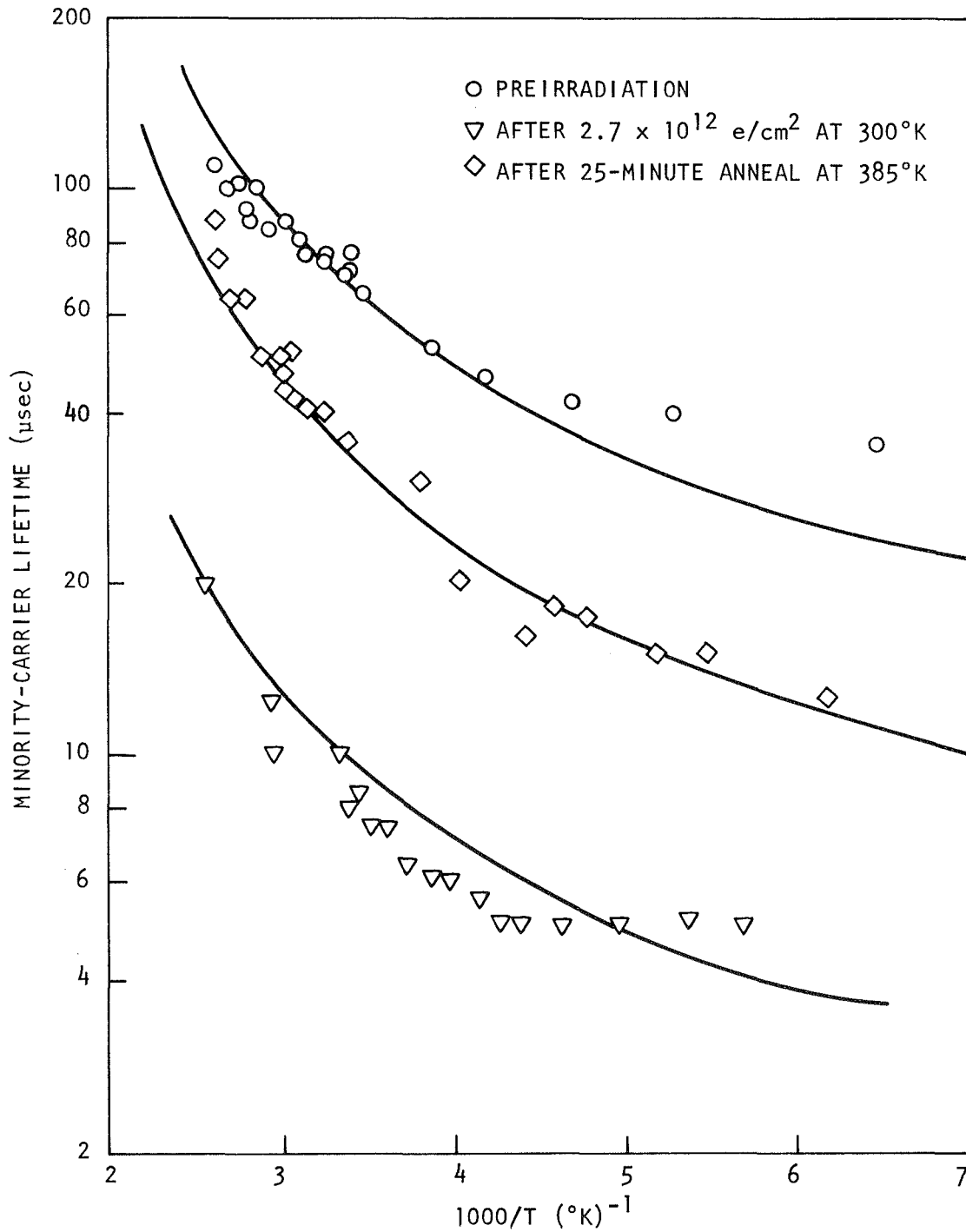


Fig. 9 Temperature dependence of minority-carrier lifetime for a 2-ohm-cm lithium-diffused QC silicon sample, before and after irradiation with $2.7 \times 10^{12} \text{ e/cm}^2$ 30-MeV electrons at 300°K and after a 25-minute anneal at 385°K

recombination through attractive centers more than 0.3 eV from a band edge. If the capture cross sections of Lax are used, the preirradiation lifetime indicates about 6×10^{10} centers/cc, rising to about 5×10^{11} centers/cc after irradiation to a fluence of 2.6×10^{12} e/cm² and dropping to about 1.2×10^{11} /cc after a 25-minute anneal at 385°K. For the sample shown in Fig. 9, the room-temperature minority-carrier lifetime degradation constant was found to be $K = 3.9 \pm 0.3 \times 10^{-8}$ cm²/e-sec. The average 300°K degradation constant for QC lithium-diffused silicon ($n(\text{Li}) \approx 2 \times 10^{15}$ /cc) was $K = 5 \pm 1 \times 10^{-8}$ cm²/e-sec.

Figures 10 and 11 are plots of inverse lifetime versus fluence for other 2-ohm-cm samples, showing 300°K lifetime degradation and anneal.

Figure 12 summarizes the degradation constant results for both oxygen-rich (QC) and oxygen-lean (FZ) lithium-diffused silicon exposed to 30-MeV electrons at 300°K. The degradation constant is seen to depend on the lithium donor density, but seems to be independent of oxygen concentration. Also shown in Fig. 12 is a theoretical prediction,⁽¹⁷⁾ and some experimental results for phosphorus-doped silicon which contained no lithium.

Figure 13 shows the minority-carrier lifetime temperature dependence before and after irradiation at 112°K. Also shown is the lifetime temperature dependence after a 30-minute, 390°K anneal. Again, the lifetime temperature dependence can be attributed to attractive deep recombination centers. From these measurements, a defect center introduction rate of 0.15 cm^{-1} is estimated, if Lax's cross section is assumed, for irradiations with 30-MeV electrons at all temperatures between 100° and 300°K. For these samples, the measured degradation constant as a function of temperature is compared with lithium-diffused FZ silicon of comparable donor density in Fig. 7. To determine the annealing behavior of these samples, both isochronal and isothermal anneals were performed after room-temperature irradiation.

Figure 14 shows the unannealed fraction of annealable recombination centers versus anneal time for isothermal anneals at several temperatures between 385° and 411°K. The annealing results of three separate 2-ohm-cm

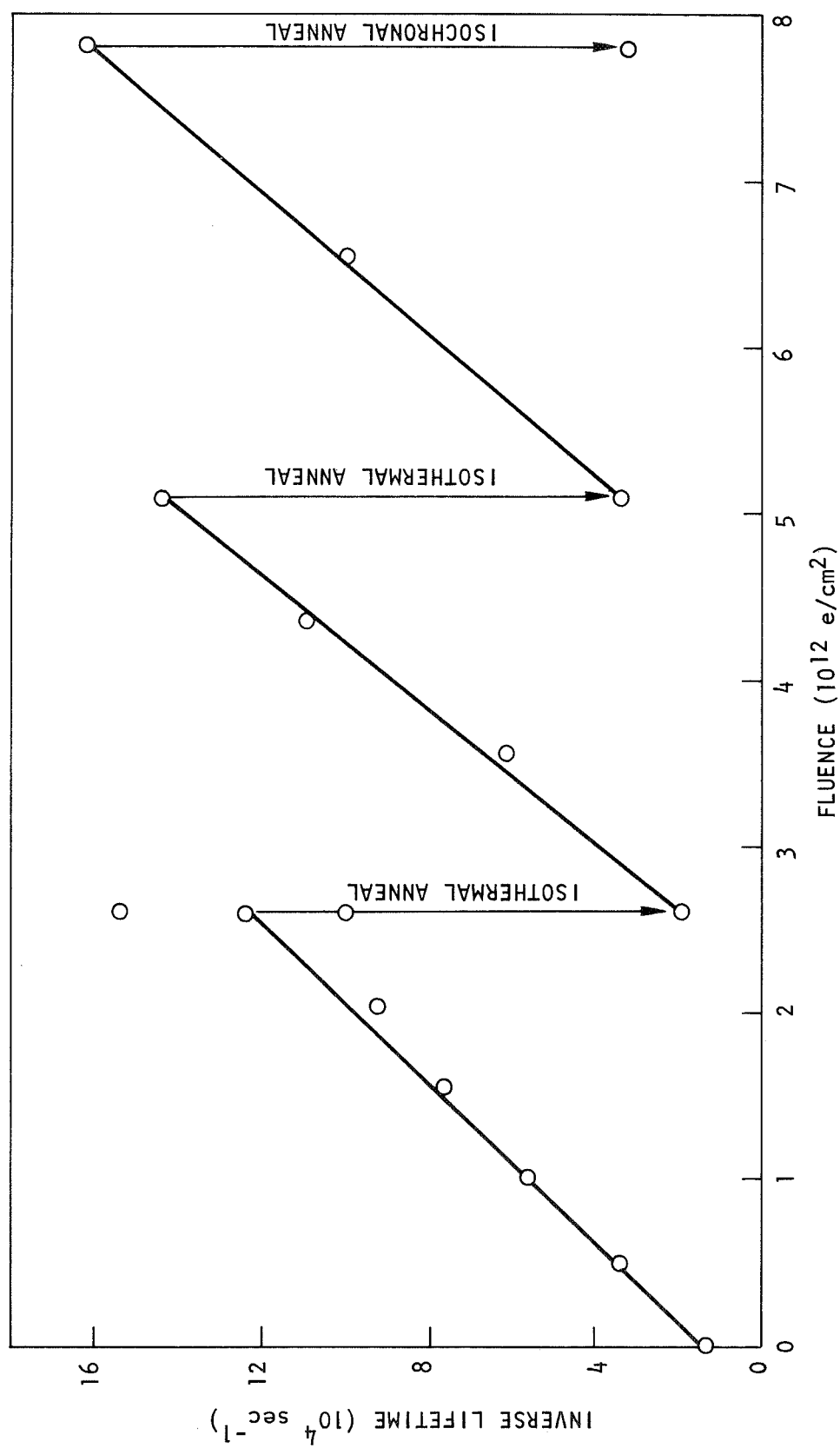


Fig. 10 Inverse minority-carrier lifetime versus 30-MeV electron fluence for a 2-ohm-cm Qc silicon sample irradiated at 300°K; isochronally annealed at 385° to 390°K for 25 to 30 minutes

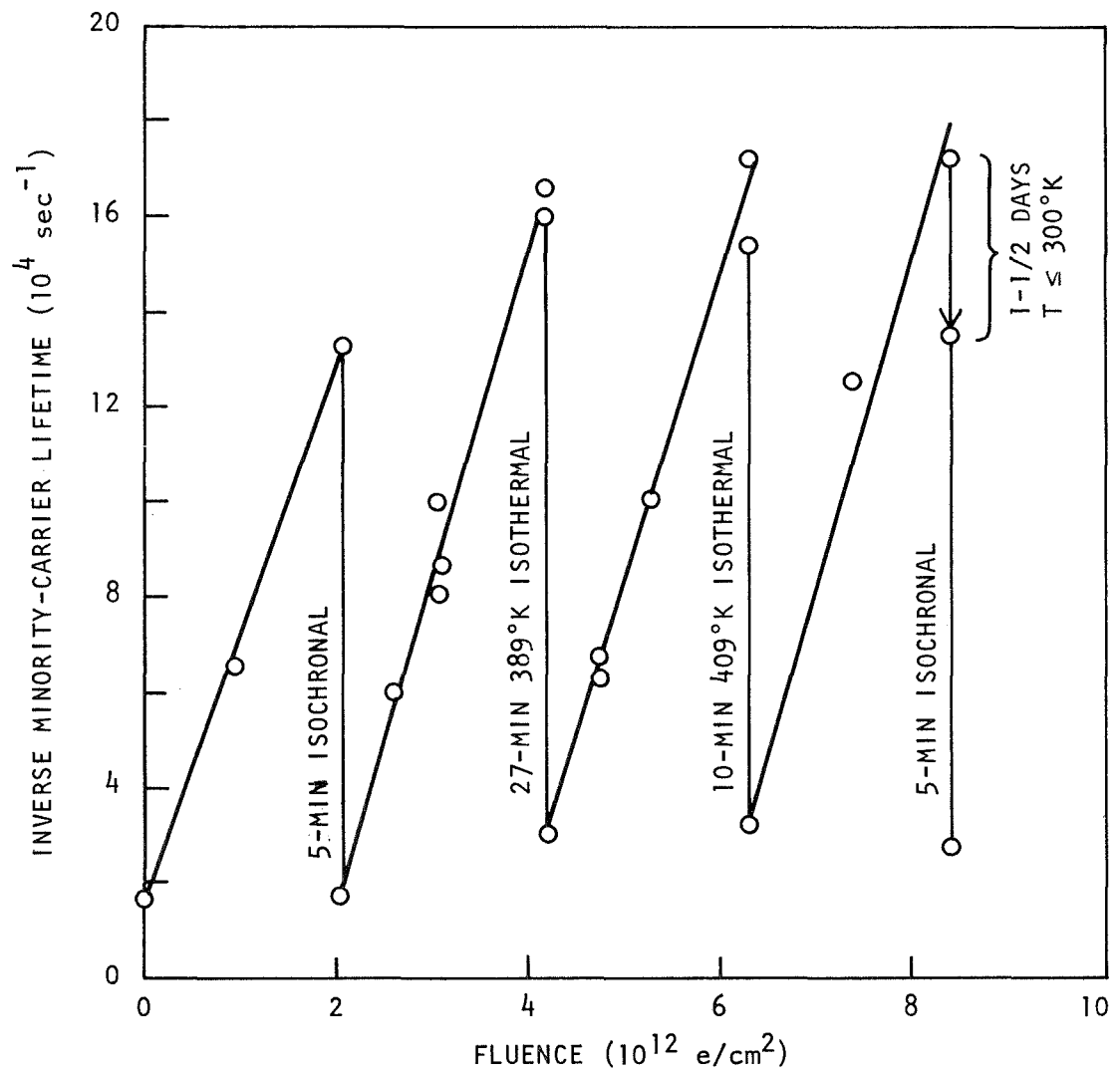


Fig. 11 Inverse minority-carrier lifetime versus 30-MeV electron fluence for lithium-diffused n-type QC silicon irradiated at 300°K

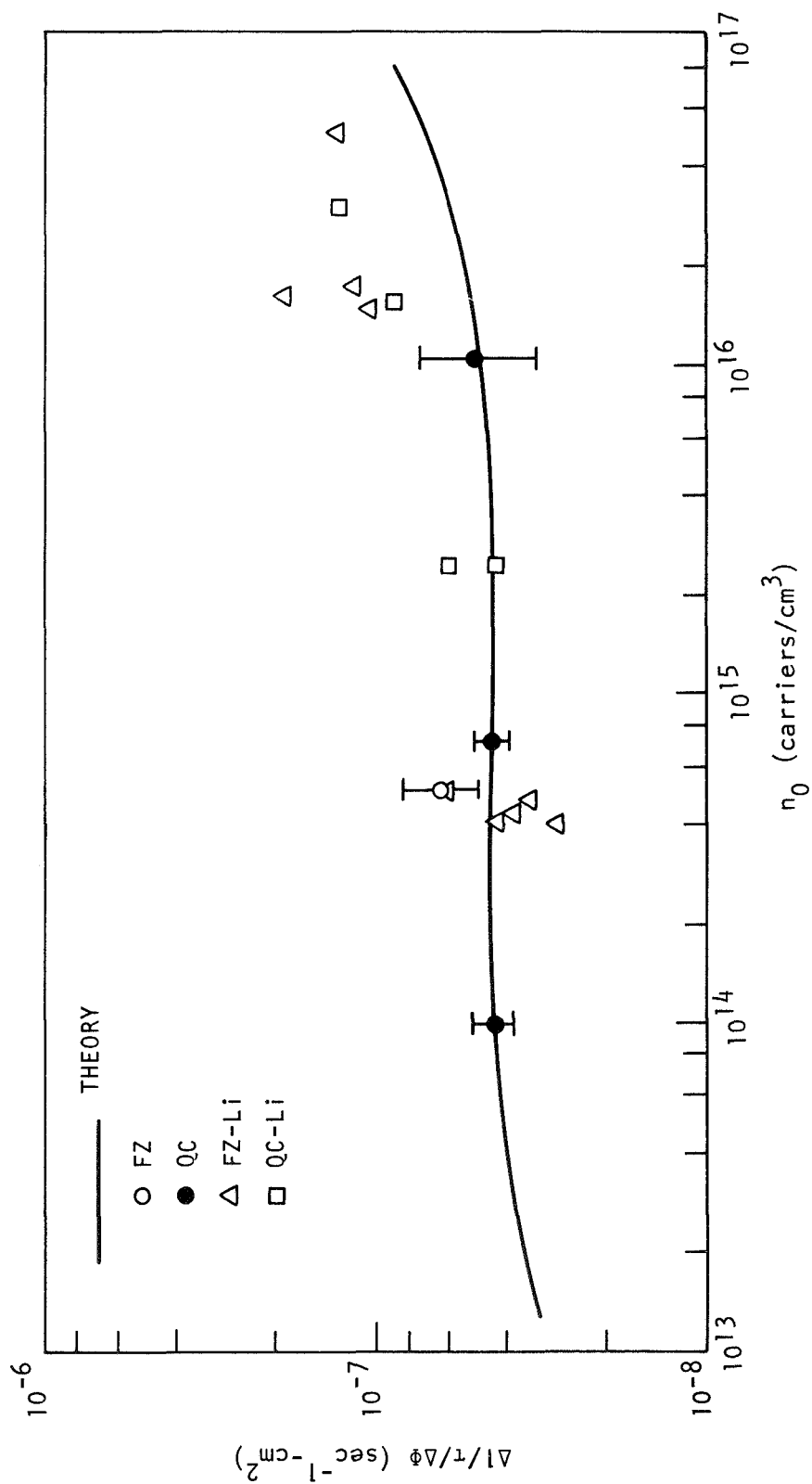


Fig. 12 Lifetime degradation constant versus majority-carrier concentration for FZ and QC n-type silicon irradiated with 30-MeV electrons at 300°K

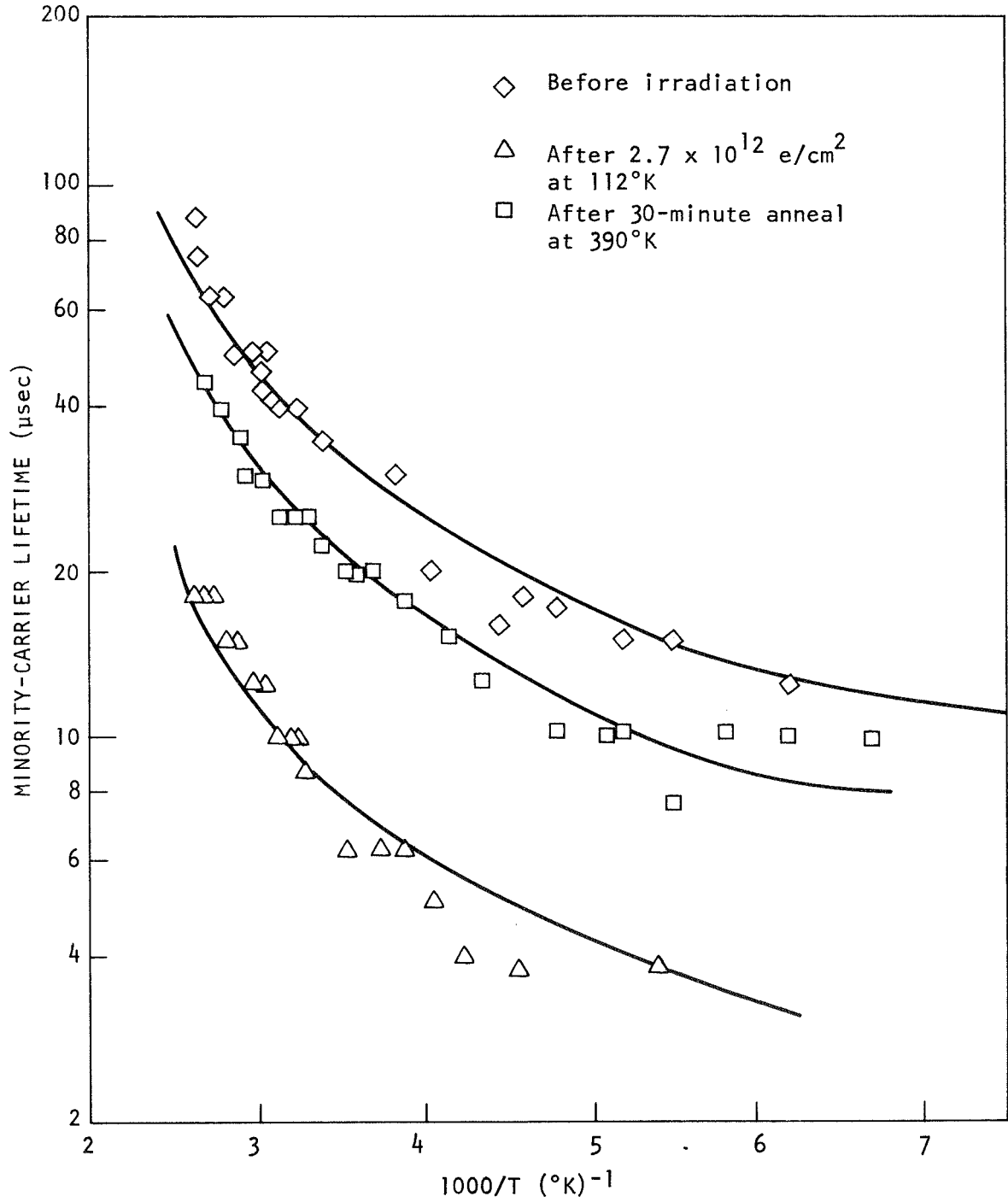


Fig. 13 Temperature dependence of minority-carrier lifetime for a 2-ohm-cm oxygen-containing lithium-diffused silicon sample, before and after irradiation with $2.7 \times 10^{12} \text{ e/cm}^2$ 30-MeV electrons at 112°K , and after a 30-minute anneal at 390°K

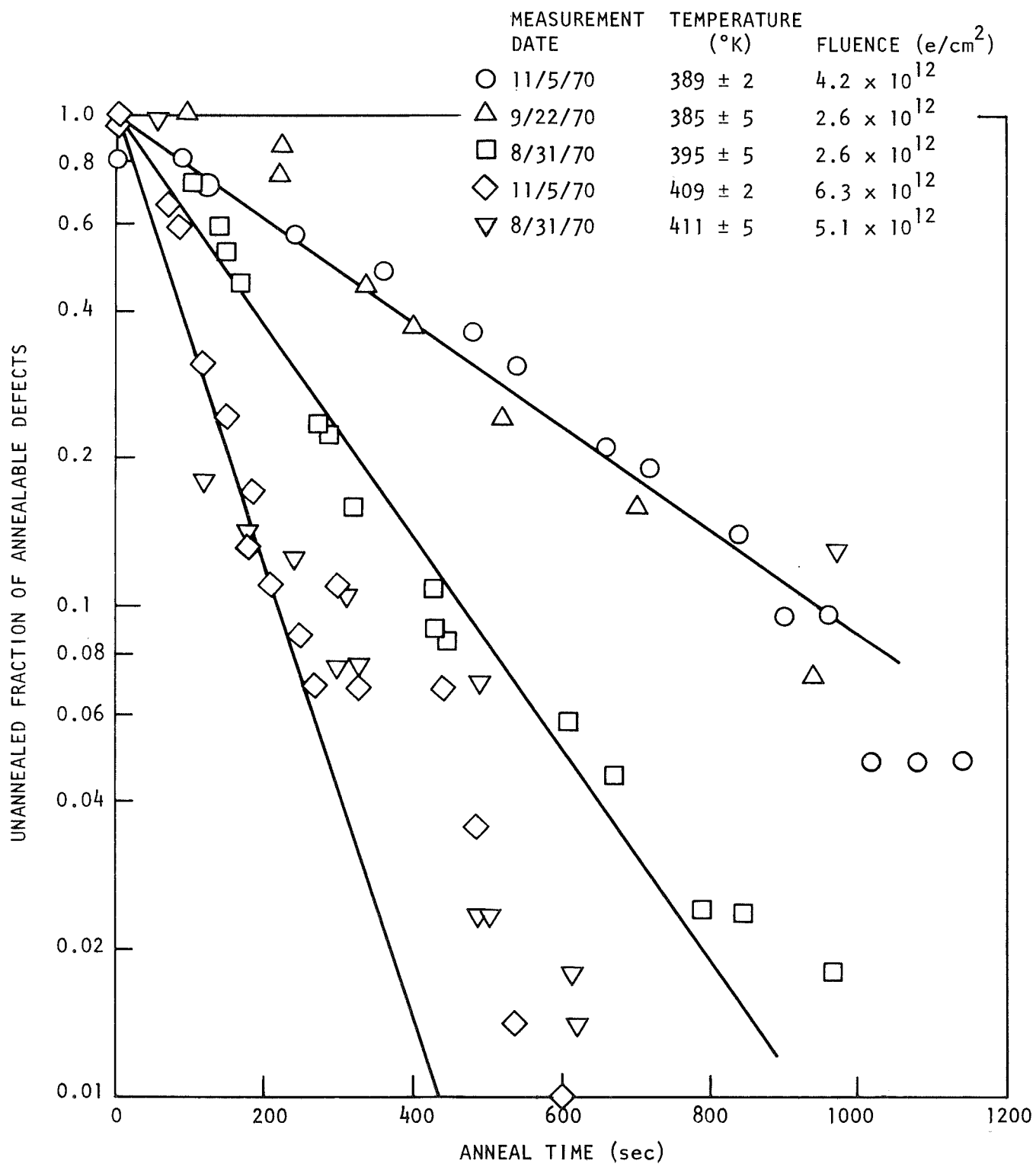


Fig. 14 Unannealed fraction of annealable recombination centers versus annealing time after 30-MeV electron irradiation of lithium-diffused n-type QC silicon irradiated at 300°K

lithium-diffused QC samples are shown. In these plots, the defect density is taken to be inversely proportional to the minority-carrier lifetime, so the unannealed fraction of annealable defects is

$$f = \frac{1/\tau_t - 1/\tau_f}{1/\tau_0 - 1/\tau_f},$$

where τ_t is the lifetime at time t ,

τ_0 is the lifetime before annealing, and

τ_f is the lifetime when annealing has ceased.

For isothermal anneals, the lifetime is measured at the anneal temperature. Within the experimental uncertainty, the unannealed fraction of annealable defects is found to satisfy the relationship $N(t) = N_0 \exp[-R(T)t]$ so that the anneal is first-order⁽¹⁸⁾ (i.e., $dN/dt = -RN$). The rate constant $R(T) = \nu_e \exp[-E/kT]$ is temperature-dependent. Analysis of the isothermal anneal data yields the activation energy, E , of the process. The isothermal data shown in Fig. 14 yielded an activation energy of $E = 0.90 \pm 0.20$ eV. The relatively large uncertainty of the activation energy could result from an uncertainty of only $\pm 3^\circ\text{K}$ in the isothermal annealing temperature. The effective frequency factor, ν_e , was calculated to be between 10^8 and 10^{10} sec^{-1} .

Figure 15 shows the unannealed fraction of annealable defects after 5-minute isochronal anneals at the indicated temperatures. For these measurements, the minority carrier is measured at 300°K before and after the 5-minute isochronal anneals at elevated temperatures, and the unannealed fraction is given by

$$f(E) = \frac{1/\tau_T - 1/\tau_f}{1/\tau_0 - 1/\tau_f},$$

where τ_T is the lifetime at 300°K immediately after annealing at temperature T . The results of five isochronal anneals on four different samples are shown in Fig. 15. It is clear that 90% of the annealing occurs within 20° to either side of 375°K . Linearity of the isothermal anneal data of Fig. 14 and the narrow annealing range of Fig. 15 indicate

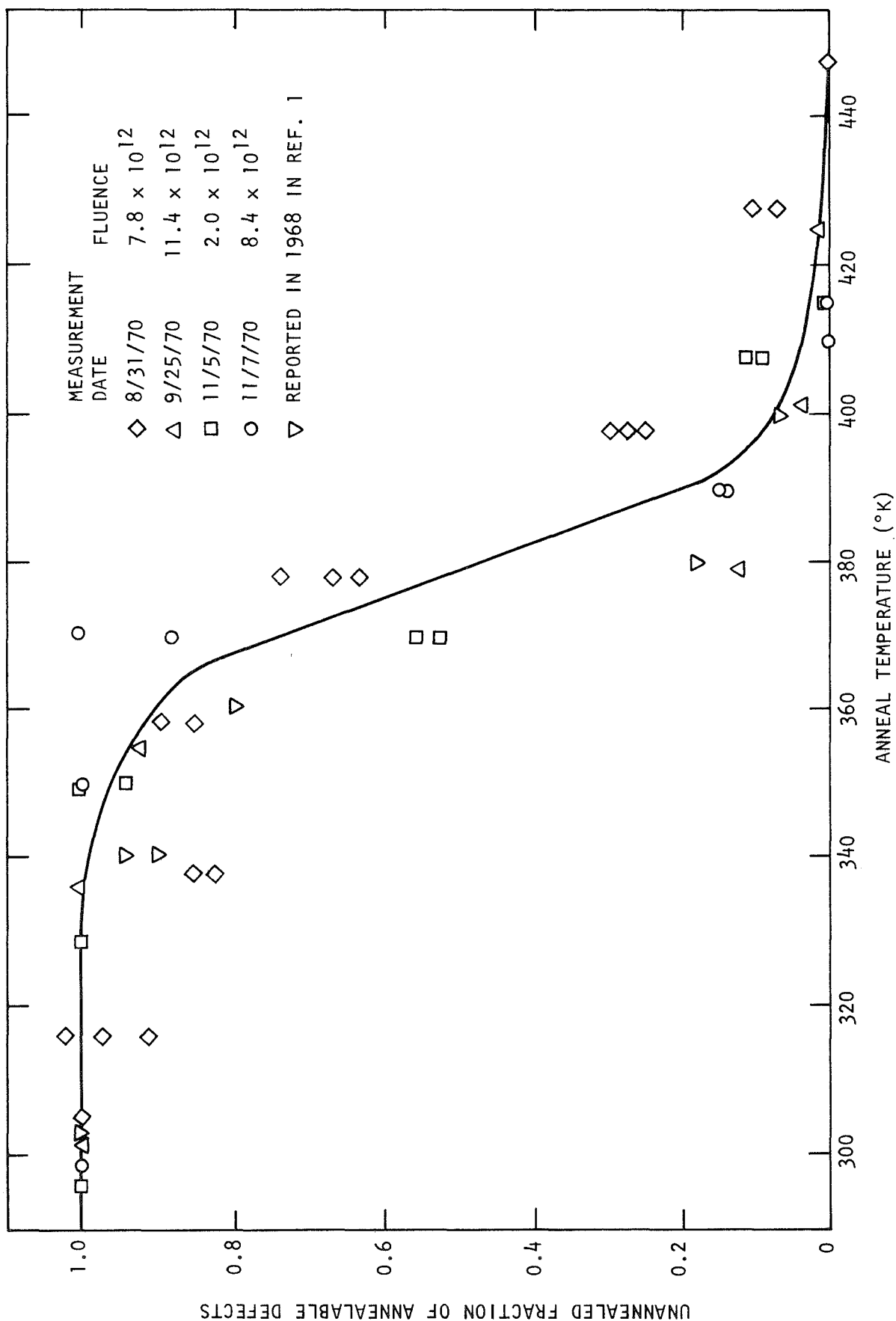


Fig. 15 Unannealed fraction of annealable defects after 5-minute isochronal anneals at indicated temperatures after 30-MeV irradiation of lithium-diffused n-type QC silicon irradiated at 300°K

the anneal is a first-order annealing process with a single activation energy. Analysis of isochronal data indicates an activation energy of about 1.0 ± 0.2 eV. These results are in agreement with the annealing activation energies reported by other experimenters^(19,20) on lithium-diffused oxygen-containing silicon solar cells, and agree reasonably well with the activation energy for motion of lithium in QC silicon.⁽²¹⁾ A single annealing stage centered near 365°K was previously observed in more heavily diffused QC silicon ($\rho = 0.67$ ohm-cm, $n_0 \approx 10^{16}/\text{cc}$),⁽¹⁾ and is shown for comparison in Fig. 15.

It is very interesting that the minority-carrier lifetime shows no evidence of the Si-Bl (oxygen-vacancy) center.

In low-energy electron-irradiated QC n-type silicon, investigators^(22,23) feel that the Si-Bl center complex is the main recombination center. These same investigators have suggested, by indirect measurement, that in 1-MeV electron-irradiated lithium-diffused QC silicon, the Bl center is still the main recombination center. However, other investigators^(1,24) have shown by direct measurement that the Bl center introduction rate is decreased by the presence of lithium. These two results on lithium-diffused material seem to be contradictory. Electron-spin resonance measurements⁽¹⁾ on a comparable lithium-diffused quartz-crucible sample (10^{16} Li/cc) indicate an introduction rate of about 0.15 cm^{-1} after the high 30-MeV electron fluence of $5 \times 10^{16} \text{ e/cm}^2$. If silicon Si-Bl centers were produced at that rate, their effect on the minority-carrier lifetime should be readily apparent at temperatures below about 200°K . Thus, the present measurements indicate that the Si-Bl center introduction rate in these samples at low fluences has been reduced by the presence of lithium or other impurities.

A possible explanation for this is that the radiation-induced mobile vacancies, which are negatively charged in n-type silicon, are captured by the positively charged phosphorus, Li^+ , or LiO^+ donors rather than by the neutral oxygen present, and that the Si-Bl (oxygen-vacancy) is produced only when the number of mobile vacancies produced approaches or exceeds the number of positively charged donors initially present.

Theoretical calculations indicate that one would expect about seven displaced atoms per incident 30-MeV electron.⁽²⁵⁾ Since most of the vacancies produced never escape their interstitials, one mobile vacancy per incident 30-MeV electron is a more reasonable estimate.⁽²⁵⁾ However, in the present measurements, the initial phosphorus donor density is estimated to be $10^{14}/\text{cc}$, the lithium donor density is estimated to be $2 \times 10^{15}/\text{cc}$, and the total fluence to which the samples were exposed was $\Phi \approx 1 \times 10^{13} \text{ e/cm}^2$. Thus, the phosphorus and lithium donor density exceeded the total number of displaced atoms by at least an order of magnitude. This suggests that the observed deep radiation-induced center may be a lithium-vacancy, lithium-oxygen-vacancy, or phosphorus-vacancy.

On the other hand, in the earlier, more complete investigation of high-purity QC silicon,⁽¹⁾ the dominant radiation-induced recombination center was thought to be an acceptor level near $(E_c - 0.38) \text{ eV}$, which is not the Si-B1 center. Thus, our current observation that no oxygen-vacancy defects were detected by minority-carrier lifetime measurements in 30-MeV electron-irradiated lithium-diffused QC silicon may be due to the nature of 30-MeV electron-induced damage and may have little to do with the presence or absence of lithium. Regardless of the identity of these defects in lithium-diffused silicon, they are annealed by lithium.

One further remark would seem to be in order: In our previous investigations on the minority-carrier lifetime in lithium-diffused FZ silicon, we observed a center located near $(E_c - 0.17) \text{ eV}$, which is about where one expects the Si-B1 center. We cannot definitely say this is not the Si-B1 center, nor have we otherwise identified this defect; however, the fact that a defect near $(E_c - 0.17) \text{ eV}$ was observed in lithium-diffused FZ (low-oxygen) silicon even before irradiation and not in lithium-diffused QC (high-oxygen) silicon even after irradiation suggests that the center near $(E_c - 0.17) \text{ eV}$ is probably not the Si-B1 center.

4.5.5 Neutron Irradiations of Lithium-Diffused FZ Silicon

The neutron-induced degradation and thermal anneal of minority-carrier lifetime in 3.7-ohm-cm lithium-diffused FZ silicon has been

described in detail elsewhere.^(2,26) This investigation showed a degradation constant of $6.4 \pm 0.4 \times 10^{-6} \text{ cm}^2/\text{n-sec}$, which is nearly the same as for phosphorus-doped FZ silicon of equivalent resistivity.⁽²⁷⁾ Isothermal and isochronal anneals indicated a first-order annealing process with an activation energy of $E \approx 0.69 \text{ eV}$ and an effective frequency near $\nu \approx 1 \times 10^7 \text{ sec}^{-1}$.

4.5.6 Neutron Irradiations of Lithium-Diffused QC Silicon

During this contract period, a sample of lithium-diffused QC silicon was damaged with fission neutrons. The bar-shaped sample was of the same 2-ohm-cm material previously described, with a length-to-cross-sectional-area ratio of 14.9 cm^{-1} . The sample was mounted in a chamber filled with helium gas, and minority-carrier lifetime was measured by both photoconductivity decay and steady-state photoconductivity techniques. The technique of monitoring lifetime as a function of fluence by continual observation of $(\Delta V/V)$, where ΔV is the voltage change produced by chopping an illumination source and V is the dc sample voltage, has been previously explained.⁽²⁾

It was shown that the minority-carrier lifetime (τ) is proportional to $\Delta V/V$,

$$\tau A = - \frac{\Delta V}{V} , \quad (6)$$

where

$$A = \frac{g}{n_0} \left(\frac{\mu_n + \mu_p}{\mu_n} \right) \quad (7)$$

is a constant for the experimental condition of 0.1% injection level, constant temperature, and low neutron fluences. In the expression for A , g is the generation rate of excess carriers due to illumination, n_0 is the equilibrium conduction electron density, and μ_n and μ_p are electron and hole mobilities, respectively.

The sample was subjected to neutron irradiation at the Gulf Rad Tech APFA facility. The APFA was run in the steady-state mode at a neutron flux of $4.17 \times 10^7 \text{ n/cm}^2\text{-sec}$ and $2.08 \times 10^7 \text{ m/cm}^2\text{-sec}$ ($E > 10 \text{ keV}$, fission). Fluences were measured by extrapolation based on sulfur

pellet dosimetry. The preirradiation minority-carrier lifetime was 60 μ sec at the irradiation temperature of 280°K.

Figure 16 shows the preirradiation and postanneal minority-carrier lifetime (τ) versus 1000/T. The curve drawn through the data points is for an attractive center using the capture cross sections of I_{ax} .⁽¹³⁾ This shows complete anneal occurred after a fluence of 2.5×10^{10} n/cm².

Figure 17 shows degradation of inverse minority-carrier lifetime ($1/\tau$) as a function of neutron fluence, Φ . The lifetime degradation constant, K, was found to be $1.6 \pm 0.2 \times 10^{-5}$ cm²/n-sec. Identical degradation constants were obtained when the sample was irradiated by fission neutrons from (a) Gulf General Atomic's TRIGA reactor and (b) neutrons produced by a (γ, n) reaction which results from irradiating a Fansteel target with 40-MeV electrons. This degradation constant is 2 to 3 times that observed in the neutron irradiation of lithium-diffused FZ silicon previously described.^(2,26)

After lifetime degradation, the sample was isochronally annealed for 5-minute periods at temperatures up to 415°K. Figure 18 shows the unannealed fraction of annealable defects measured at 280°K versus isochronal anneal temperature. For comparison, the equivalent results for 3.7-ohm-cm lithium-diffused FZ silicon are plotted on the same figure. Approximately 95% of the total radiation-induced recombination centers were annealed by this isochronal annealing schedule, and the annealing is centered near 360°K. The sample lifetime was repeatedly degraded, and isothermal anneals at 378°, 383°, 391°, and 403°K were performed. Figure 19 shows the results of two isothermal anneals as the unannealed fraction of annealable defects as a function of time. The anneal at 378°K was too slow to measure in a reasonable amount of time, and at 403°K the anneal was essentially complete in 200 seconds.

The unannealed fraction of annealable defects for isochronal annealing has been shown⁽²⁾ to be

$$f_T = \frac{1/\tau_T - 1/\tau_f}{1/\tau_0 - 1/\tau_f} = \frac{(V/\Delta V)_T - (V/\Delta V)_f}{(V/\Delta V)_0 - (V/\Delta V)_f},$$

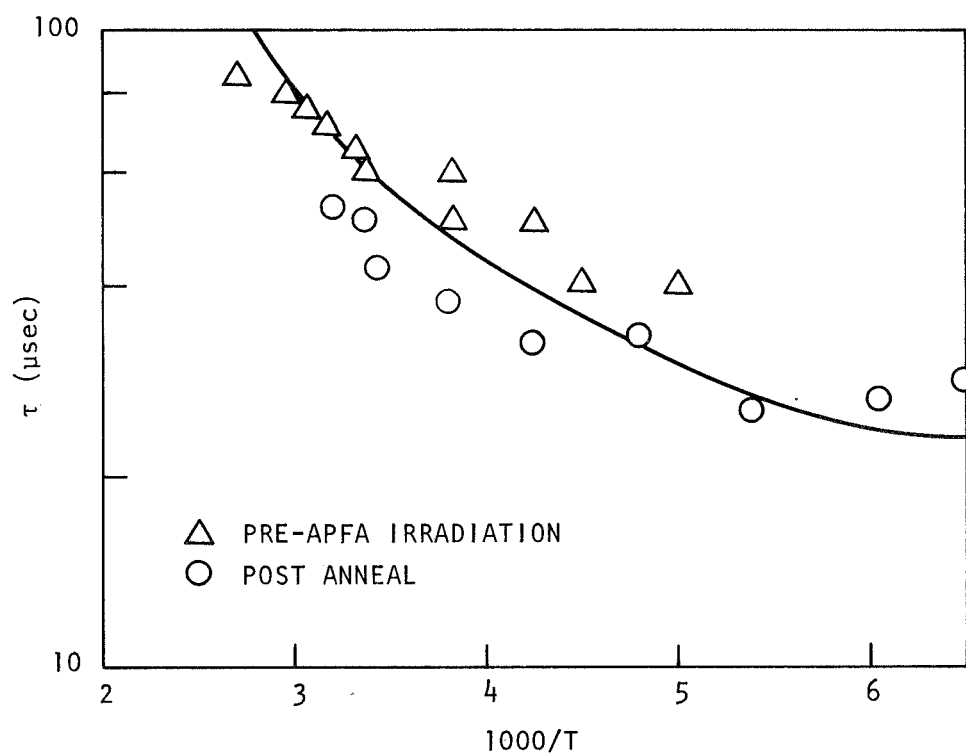


Fig. 16 Minority-carrier lifetime versus $1000/T$ of lithium-diffused n-type QC silicon

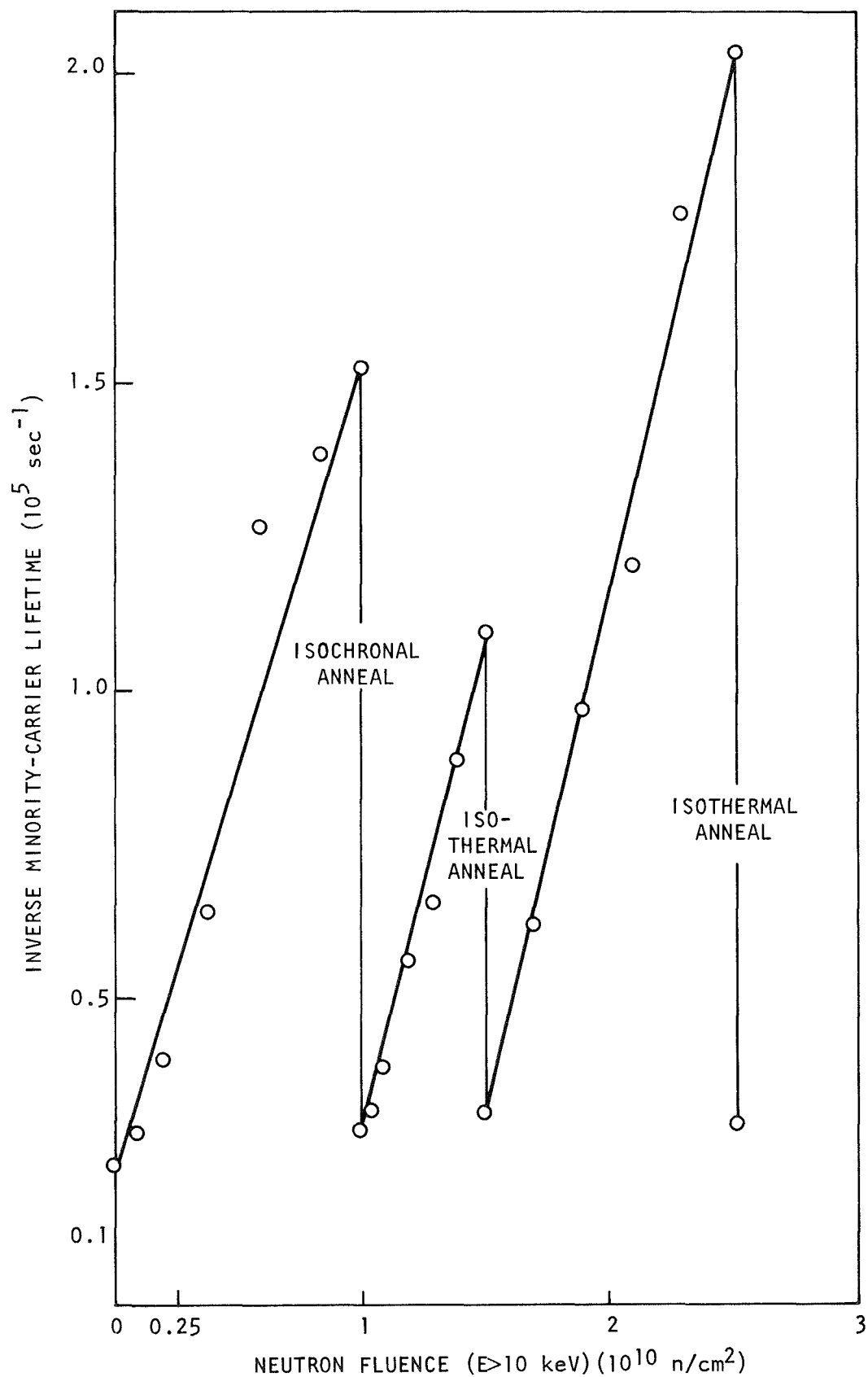


Fig. 17 Degradation of inverse lifetime of lithium-diffused n-type QC silicon at 280°K as a function of neutron fluence

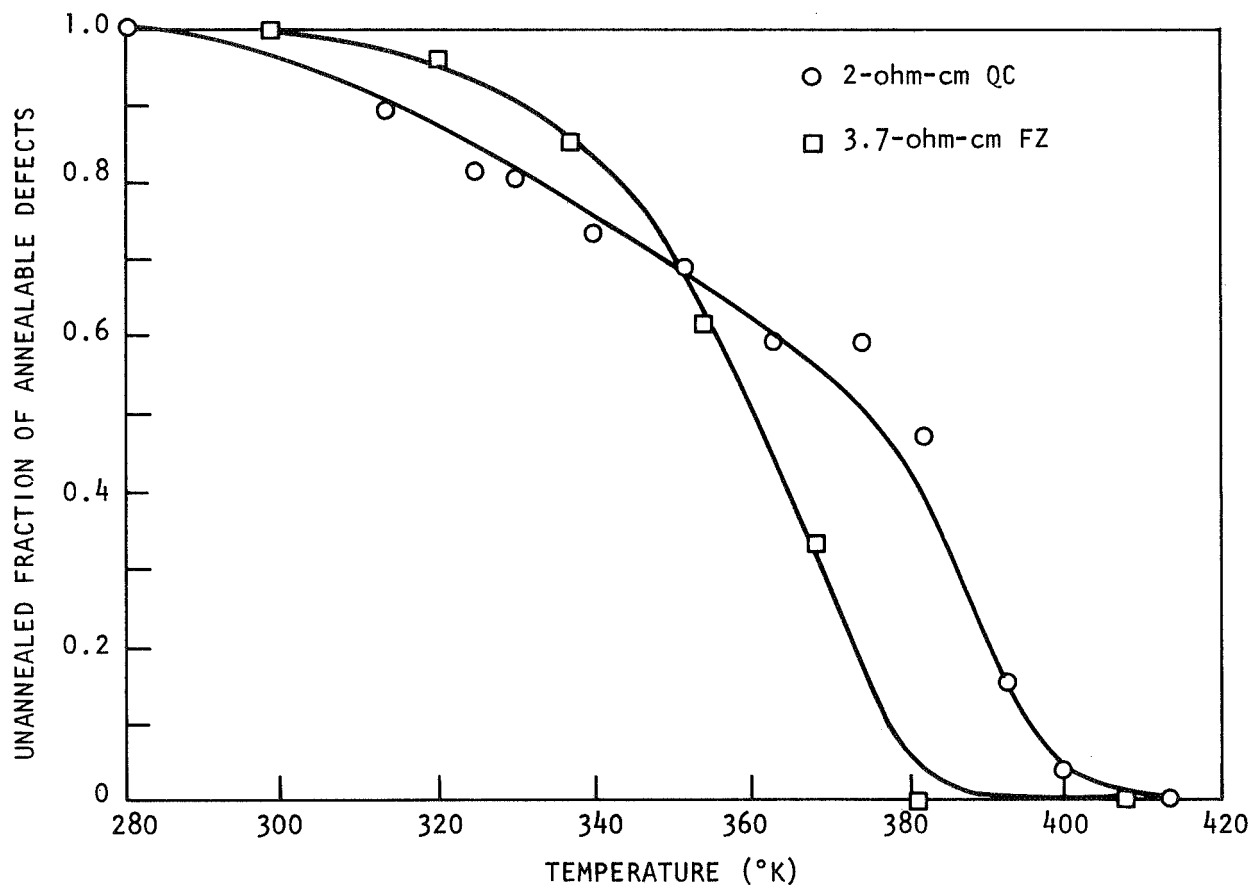


Fig. 18 Unannealed fraction of annealable defects in lithium-diffused FZ and QC n-type silicon, measured at 280°K, versus isochronal anneal temperature, after APFA irradiation

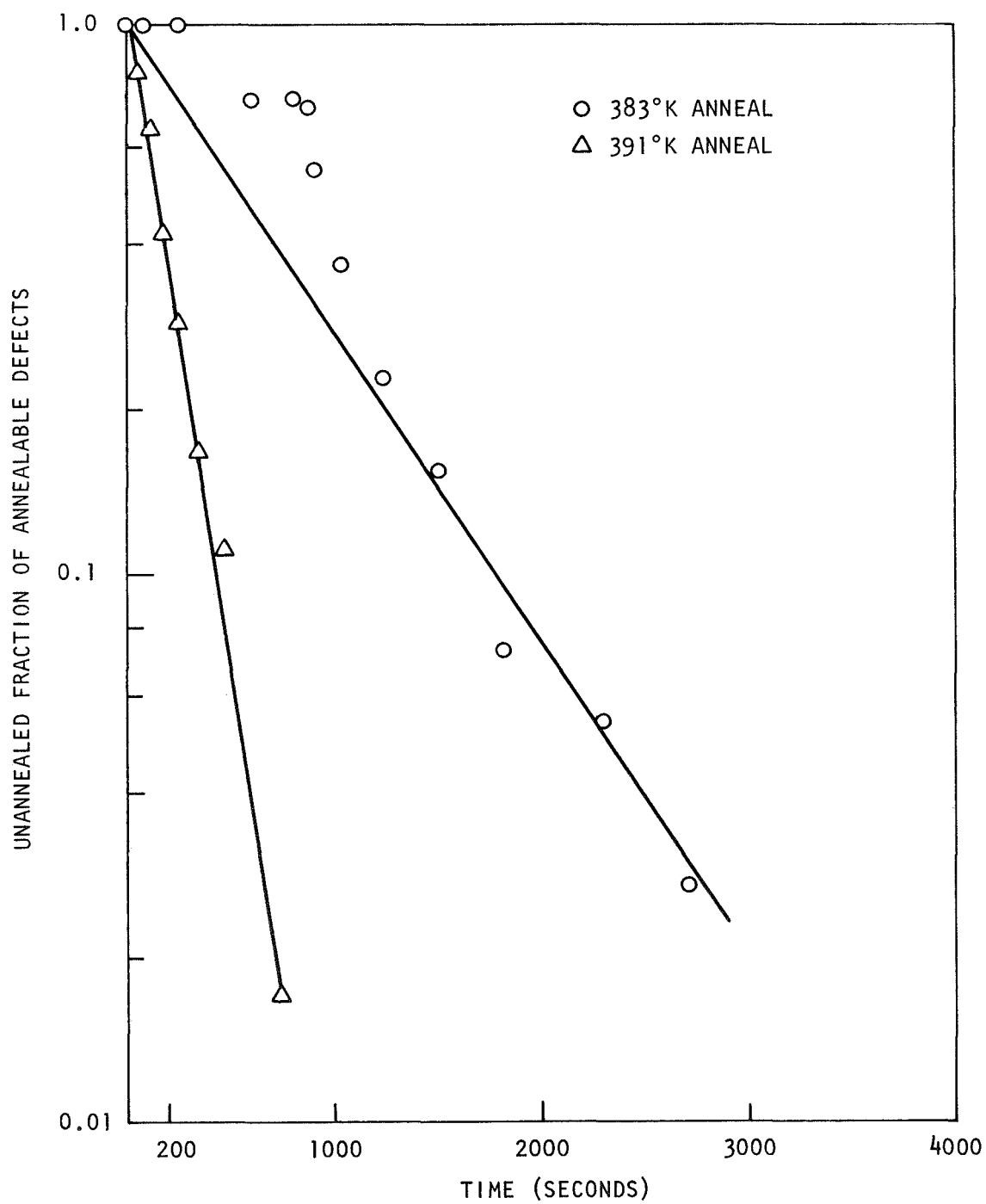


Fig. 19 Isothermal anneal of lithium-diffused n-type Qc silicon after APFA irradiation

where the τ 's are the minority-carrier lifetimes previously defined and the $(V/\Delta V)$ terms are the corresponding steady-state measurements.

A similar expression for the unannealed fraction of annealable defects exists for isothermal annealing, except that temperature T is replaced by time t , and lifetimes τ by the steady-state measurements $(V/\Delta V)$.

Linearity of the isothermal anneal data, when plotted as shown in Fig. 19, would indicate the anneal is a first-order process. Unfortunately, the 383°K anneal shows considerable nonlinearity during the first 1000 seconds. In addition, isochronal annealing occurred over a 100° range of 300° to 400°K (see Fig. 18), in contrast to the sharply defined annealing stage obtained on neutron-irradiated lithium-diffused FZ silicon. Thus, there is some uncertainty whether or not these annealing data actually represent a single first-order annealing stage. If, for lack of positive contradictory evidence, one assumes these data do represent a single first-order anneal of neutron-induced damage, analysis of the isochronal and isothermal data of Figs. 18 and 19 give an activation energy of $E = 1.2 \pm 0.6$ eV. The uncertainty of this energy is so large that a determination of an effective frequency would be meaningless.

The minority-carrier lifetime temperature dependence before and after neutron irradiation is shown in Fig. 20. To obtain data on low-injection-level minority-carrier lifetimes of less than 10 μ sec, photoconductivity decay times were measured. A 600-keV flash X-ray which has a 120-nsec width was used as an injection source. Since neutron irradiations produce damage clusters, it may not be legitimate to use the recombination cross section theory of Lax⁽¹³⁾ or Leadon.⁽¹²⁾ However, the solid lines drawn through the data of Fig. 20 represent Lax's predictions for an attractive recombination center. It is apparent that the temperature dependence of minority-carrier lifetime of neutron-irradiated lithium-diffused QC silicon is indistinguishable from the temperature dependence of attractive centers.⁽¹³⁾

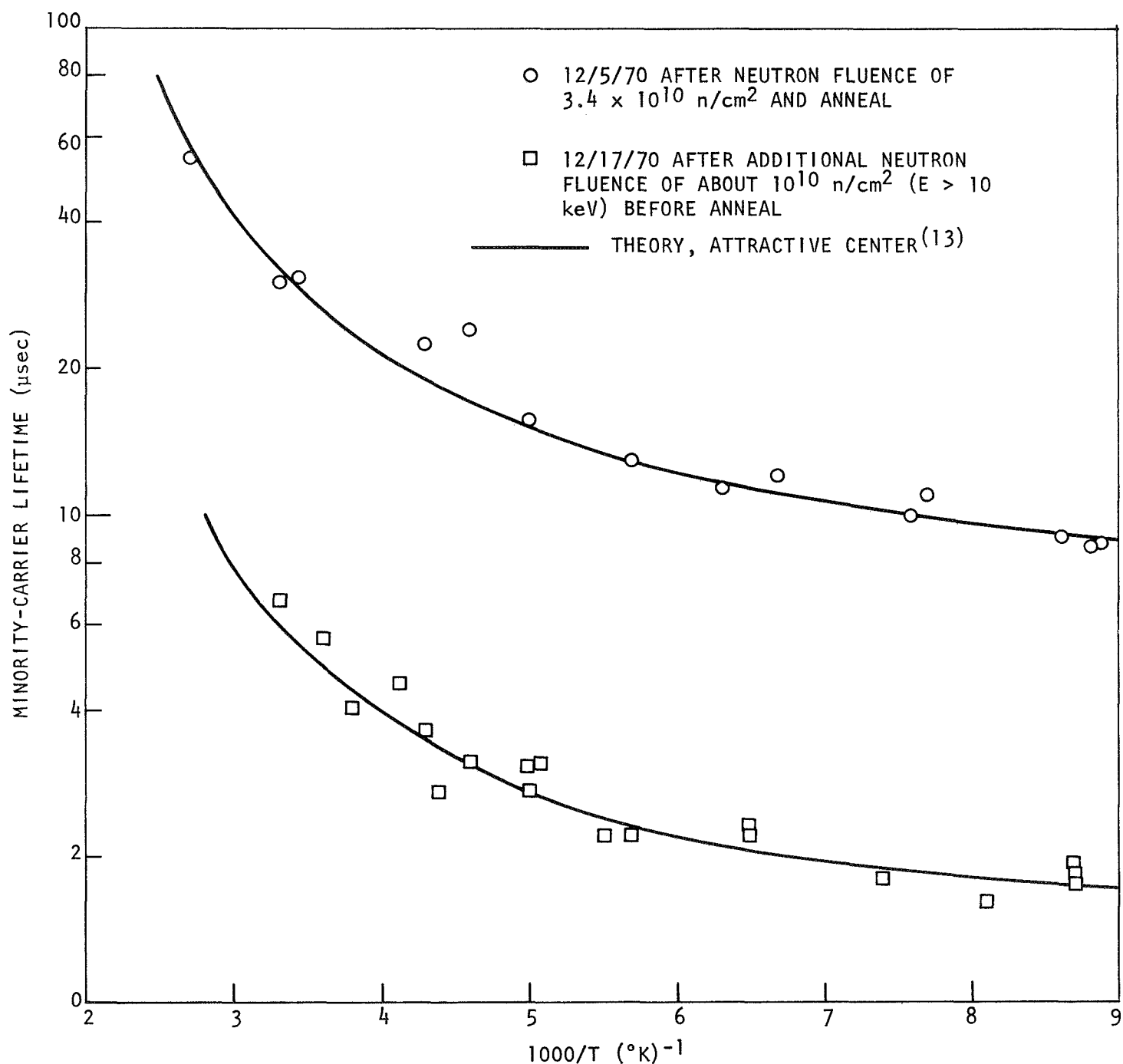


Fig. 20 Minority-carrier lifetime temperature dependence of a 2-ohm-cm lithium-diffused QC silicon sample before and after neutron irradiation of about $1 \times 10^{10} \text{ n/cm}^2$ ($E > 10 \text{ keV}$)

4.6 CONCLUSIONS

4.6.1 30-MeV Electron Irradiation

The minority-carrier lifetime of 30-MeV electron-irradiated, FZ and QC lithium-diffused n-type silicon was studied. The lifetime temperature dependence, degradation rate, and annealing characteristics were measured. Both lightly diffused ($n_0 \leq 2.0 \times 10^{15} \text{ cm}^{-3}$) and heavily diffused ($n_0 \geq 1.0 \times 10^{16}$) samples were investigated. From these studies, the following conclusions can be drawn.

1. The initial preirradiation lifetime of lightly diffused FZ silicon is due to at least two centers. Its temperature dependence indicates one center of unknown charge near ($E_c - 0.17$) eV, and an attractive center deeper than 0.35 eV from either band edge. The shallow center is not the Si-Bl center because, in lightly diffused QC silicon, preirradiation lifetime measurements indicate attractive recombination centers further than 0.3 eV from a band edge, and no center near ($E_c - 0.17$) eV. Because the initial conduction electron concentration in the heavily diffused silicon was so high, the minority-carrier lifetime temperature dependence could not distinguish between the two centers if both were present. Our measurements on heavily diffused FZ and QC silicon indicate attractive centers deeper than ($E_c - 0.17$) eV.
2. At least two kinds of recombination centers are introduced in lightly diffused FZ silicon by the 30-MeV electron irradiation: one deeper than about 0.35 eV, which controls recombination above 150° to 200°K , and one near ($E_c - 0.17$) eV, which is dominant below 150° to 200°K . In QC silicon, all radiation-induced recombination centers seem to be more than 0.3 eV from a band edge. The recombination centers in heavily diffused silicon are not well located but are deeper than ($E_c - 0.17$) eV.

3. The room-temperature minority-carrier lifetime degradation constant for heavily diffused FZ and QC silicon was approximately twice that for lightly diffused or nondiffused silicon. The increased degradation constant of heavily lithium-diffused silicon compared with that of non-lithium-diffused silicon is interpreted to indicate that the presence of lithium is effective in the production of recombination centers in lithium-diffused silicon. These recombination centers either contain lithium or are affected in their production by lithium.
4. In lightly diffused FZ and QC silicon, the minority-carrier lifetime at and above room temperature is controlled by recombination through centers further than about 0.3 eV from either band edge. These centers show first-order thermal annealing near $380 \pm 20^\circ\text{K}$, with activation energies of 0.8 ± 0.1 eV for FZ and 1.1 ± 0.2 eV for QC silicon. Effective frequency factors scale with lithium concentration.
5. In lightly diffused FZ silicon, the radiation-induced center at ($E_c - 0.17$) eV which is dominant at low temperatures was not appreciably annealed in 1 hour at 390°K but appears to anneal, at least partially, over long periods at room temperature.
6. The annealing of the recombination centers in lightly irradiated, heavily diffused FZ and QC silicon is apparently complete. However, after extended fluences, the annealing of the recombination centers is not complete; not all the recombination centers are annealed. Trapping centers also are created, and these are not reduced by thermal annealing below 430°K . This may reflect a depletion of lithium which is able to neutralize a recombination or trapping center.
7. In general, it appears that in electron-irradiated, lithium-diffused, FZ and QC silicon, both lithium-dependent and non-lithium-dependent recombination centers are produced. The number of each depends on the lithium concentration, with the largest number of lithium-dependent centers being found in

highly diffused silicon and the largest number of non-lithium-dependent centers being found in lightly diffused silicon.

8. No irradiation temperature dependence of the recombination center introduction rate for 30-MeV electrons in the 115° to 300°K temperature range was observed. However, the minority-carrier lifetime degradation constant for lithium-diffused samples irradiated and measured at 300°K is five to ten times smaller than that for samples irradiated and measured at 115°K. This may be attributed to the temperature dependence of the recombination center capture cross section.
9. Isochronal and isothermal annealing results on both FZ and QC lithium-diffused electron-irradiated silicon indicate that the anneal is a single-stage first-order anneal. Activation energies 0.8 ± 0.1 eV for FZ samples and 1.1 ± 0.2 eV for QC samples were observed, which agree with the activation energies of diffusion of lithium in FZ and QC silicon,⁽²¹⁾ respectively. Effective frequency factors ranged from 10^7 to 10^{11} sec⁻¹, increasing with increasing lithium donor density. These facts strongly suggest that the thermal annealing of radiation defects in lithium-diffused silicon is due to the migration of lithium to the defect center.

4.6.2 Fission Neutron Irradiations

A number of observations can be made concerning the results of minority-carrier lifetime studies in fission-neutron-irradiated lithium-diffused silicon. First, the lifetime degradation constant for 4-ohm-cm FZ silicon is nearly the same as for silicon containing no lithium ($K \approx 6 \times 10^{-6}$ cm²/n-sec), which is consistent with the lack of impurity dependence for neutron damage. The degradation constant for oxygen-rich QC silicon, however, is more than twice as great, suggesting a radiation-induced recombination center which contains or whose creation depends upon oxygen. Second, more than 90% of the neutron damage was annealed at temperatures between 300° and 380°K. From Stein's data, one would expect less than 10% recovery for non-lithium-diffused n-type silicon

subjected to the same annealing schedule. This is to be contrasted with the insignificant impurity dependence of the annealing observed for phosphorus- and arsenic-doped n-type silicon. Third, the activation energies determined from isothermal and isochronal anneals are very close to $E = 0.66 \pm 0.05$ eV for the energy of lithium diffusion in FZ silicon. The annealing results for QC silicon are more uncertain, but indicate an energy of $E \approx 1.2 \pm 0.6$ eV. The activation energy for lithium-oxygen dissociation and lithium diffusion is thought to be about 1.07 ± 0.05 eV. This strongly suggests that the anneal depends on the diffusion of lithium to the neutron-produced recombination centers in both FZ and QC silicon. Finally, the effective frequency factor of $\nu \approx 10^7 \text{ sec}^{-1}$ for annealing in FZ silicon suggests long-range migration.

5. STUDY OF SPECIFIC RADIATION-INDUCED DEFECTS

5.1 ELECTRON-SPIN RESONANCE

5.1.1 Introduction

Electron spin resonance (ESR) has been an important technique in the study of radiation effects in silicon, since ESR is one of the few techniques⁽²⁸⁾ which provides information about the microscopic structure of the defects. At Gulf Rad Tech, ESR has been successfully used in several programs^(6,14,29-31) investigating the production, annealing, and properties of various damage centers, including the Si-B1, Si-G6, Si-G7, and Si-G8 centers. In addition, ESR has been used to study the effect of lithium on specific radiation-induced centers. A thorough investigation of the effect of lithium on the B1 (oxygen-vacancy) center was completed under an earlier contract.⁽¹⁾ This study was of particular value since many investigators feel that the B1 center is the predominant recombination center in silicon irradiated with 1-MeV electrons. The results of this study, which are reviewed below, provided invaluable insight into the interaction of lithium with radiation-produced entities, including impurity-related defects.

An attempt to study the phosphorus-vacancy (Si-G7) center in lithium-diffused silicon by ESR techniques is also reviewed below.

During the present contract period, the ESR technique was used to gain more fundamental information of the effects of lithium on the production and annealing of the vacancy-phosphorus (Si-G8) center.

The 9.2-GHz superheterodyne ESR spectrometer used in the measurements has been previously described.⁽²⁾ All measurements were made at 20°K.

5.1.1.1 Summary of the Oxygen-Vacancy (Si-B1) Center Investigation. An investigation of the effect of lithium on the Si-B1 (vacancy-oxygen) center was completed under an earlier contract⁽¹⁾ and is summarized in the first five lines of Table 1.

Table 1
HISTORY OF PREVIOUS WORK

Growth and Dopants	Phosphorus Concn. (#/cm ³)	Lithium Concn. (#/cm ³)	Fluence (e/cm ²)	Irrad. Temp. (°K)	Center Ident.	Center Rate (cm ⁻¹)	Center Concn. (#/cm ³)	Center Anneal Point (°K)	Carrier Removal Rate (cm ⁻¹)	Ref. No.
FZ - P	1x10 ¹⁴	8x10 ¹⁵	None	NA	LiO	NA	5x10 ¹⁵	-	-	1
QC - P	1x10 ¹⁶	4x10 ¹⁷	None	NA	LiO	NA	8x10 ¹⁷	-	-	1
FZ - P	1x10 ¹⁴	8x10 ¹⁵	5x10 ¹⁶ & 5x10 ¹⁵	300	None	NA	<5x10 ¹⁵	-	-	1
QC - P	1x10 ¹⁶	4x10 ¹⁷	2x10 ¹⁷	300	Si-B1	0.025	5x10 ¹⁵	320	1.7	1
QC - P	1x10 ¹⁶	1x10 ¹⁶	5x10 ¹⁶	300	Si-B1	0.14	7x10 ¹⁵	320	-	1
FZ - P	< 10 ¹⁴	1x10 ¹⁶	3x10 ¹⁶	300	None	NA	<5x10 ¹⁵	-	-	2
FZ - P	< 10 ¹⁴	1x10 ¹⁷	4x10 ¹⁷	<150	None	NA	<5x10 ¹⁵	-	-	2
FZ - P	1.1x10 ¹⁶	3.6x10 ¹⁶	2.2x10 ¹⁷	<150	Unknown	0.05	1x10 ¹⁶	-	-	2

The Si-BI introduction rate for non-lithium-diffused quartz-crucible (QC) silicon is about 0.15 cm^{-1} , so comparison with Table 1 indicates that the Si-BI introduction rate in lithium-diffused silicon is inversely proportional to the lithium donor density. A similar impurity dependence was observed by Watkins⁽³²⁾ in phosphorus-doped silicon. This indicates a competition for the radiation-induced vacancy between the oxygen and the lithium donor. The Si-BI center density in high-lithium-concentration samples anneals near 320°K (see Table 1), while the Si-BI center anneals in silicon without lithium near 550°K .⁽³²⁾ Thus, the effect of adding lithium to the QC material is to lower the Si-BI introduction rate and to reduce its annealing temperature.

5.1.1.2 Summary of the Divacancy (Si-G7) Investigation. The divacancy is an important damage center to study, since it is thought to be one of the recombination centers present in silicon after high-energy electron and neutron irradiation. This center is believed to have three electrical levels within the forbidden gap. These levels are located at 0.17 and 0.4 eV below the conduction band and at 0.25 eV above the valence band. If the Fermi level is (1) above 0.17 eV, the divacancy is in a double negative charge state and nonparamagnetic; (2) between 0.17 and 0.4 eV, the divacancy is in a single negative charge state and paramagnetic; and (3) below 0.4 eV, the divacancy is neutral and nonparamagnetic.^(28,33)

An investigation of the effect of lithium on the Si-G7 (divacancy) was made⁽²⁾ and is summarized in lines 6 and 7 of Table 1. The results of this work showed that for room-temperature (300°K) irradiations, divacancy production is reduced by the presence of lithium. The overall effect of lithium is to decrease the number of divacancies present after a 300°K irradiation. The lithium either lowers the introduction rate of divacancies or anneals the divacancies once they are formed. Earlier work⁽¹⁾ has shown that both of these mechanisms are present in BI center production and annealing.

The ESR measurements of the divacancy were performed after irradiations below 150°K . Low irradiation temperatures were used to prevent thermal annealing of the divacancy by lithium motion before ESR measurements could be performed. These experiments were inconclusive because

no resonances were observed. It was concluded that this failure was due to either (1) a lower divacancy introduction rate in lithium-diffused silicon or (2) the presence of divacancies in a nonparamagnetic charge state. Infrared absorption measurements, described in Section 5.2, lead us to believe that divacancies are produced at close to the normal rate by 30-MeV electron irradiation at or below 150°K, but that these divacancies interact with lithium at or below 300°K to produce a different center.

5.1.1.3 Summary of Prior Vacancy-Phosphorus (Si-G8) Work. The vacancy-phosphorus is a recombination center which is thought to consist of one electrical level about 0.4 eV below the conduction band. If the Fermi level is above this level, the Si-G8 center is in a single negative charge state and is nonparamagnetic; however, if the Fermi level is below 0.4 eV, the center is in a neutral charge state and is paramagnetic. Thus, the Si-G8 center is better suited than the divacancy to study by ESR because it is paramagnetic over a much wider fluence range. The principal values in the diagonalized Si-G8 g-tensor are $g_1 = 2.0005$, $g_2 = 2.0112$, and $g_3 = 2.0096$, with $\Phi = 32^\circ$ from the [011] axis in the (011) plane.⁽²⁸⁾

An investigation of the effects of lithium in the production and annealing of the Si-G8 (vacancy-phosphorus) was begun last year⁽²⁾ and was completed during this year. This previous work is also summarized in the last line of Table 1.

On reexamination of the data taken last year, we concluded that the observed resonance in the phosphorus-doped material irradiated at $T \leq 150^\circ\text{K}$ could not be positively identified due to a low signal-to-noise ratio and the broad resonance spectrum. Thus, it was decided to attempt to positively identify the observed centers.

5.1.2 Samples

Samples for the Si-G8 ESR studies were produced by the diffusion of lithium in float-zone (FZ) n-type silicon. The lithium paint-on technique was used to diffuse lithium into the samples. Samples prepared ranged in resistivity from 0.16 to 0.30 ohm-cm, which corresponds to room-temperature carrier concentrations from 4.7 to 2×10^{16} carriers/cm³.

The samples used during this work are described in Table 2. Irradiation was performed with 30-MeV electrons from the Gulf Rad Tech Linac facility. All the ESR samples had volumes of about 0.023 cm^3 and were oriented (using light reflection patterns from an etched crystal face) along the $\langle 111 \rangle$ and $\langle 110 \rangle$ crystal axes.

A large resonance signal ($g = 1.999$, line width at half maximum of 1.9 gauss, concentration on the order of 10^{16} centers/ cm^3) was observed only in the nonirradiated, lithium-diffused material. This resonance, generally believed to be due to LiO^+ , has the same g value and about the same strength as the marker that is used to calibrate the number of spins in the ESR samples.

The resonance completely disappears after irradiation, and was not observed to return at any time during thermal anneals. Both the LiO^+ resonance and its decrease in irradiation were observed in our previous study of the oxygen-vacancy (Si-B1) center.⁽¹⁾ There was no change in the magnitude of the phosphorus donor resonance after lithium diffusion.

5.1.3 Results of ESR Measurements

Samples 14, 17, 18, 19, and 20, shown in Table 2, were irradiated to the 30-MeV electron fluences at 150°K. All clearly gave an ESR spectrum characteristic of the Si-G8 (vacancy-phosphorus or E) center seen by Watkins.⁽³⁴⁾ In addition to the Si-G8 center, a few weak lines were also observed. These lines were not strong enough to identify, but they have been seen before in non-lithium-diffused vacuum FZ phosphorus-doped material;⁽³⁵⁾ hence, they are not due to the presence of lithium.

These five samples yielded introduction rates for the Si-G8 center of from 0.1 to 0.2 cm^{-1} , which is comparable to the introduction rates previously reported for non-lithium-diffused material irradiated by 30-MeV electrons at 77°K.⁽¹⁾ The average carrier removal rate was about 0.2 cm^{-1} .

The conclusion that can be drawn from these data is that the addition of up to three times the amount of lithium as phosphorus concentration does not significantly affect the Si-G8 center introduction rate, nor does it introduce new lithium-dependent resonances.

Table 2
SAMPLES USED IN ESR STUDIES

Sample No.	Phosphorus (#/cm ³)	Lithium (#/cm ³)	Fluence* (e/cm ²)	ESR Center Identification
14	1.1x10 ¹⁶	1x10 ¹⁶	1x10 ¹⁷	Si-G8
15	"	0	0	Phosphorus donor
16	"	1x10 ¹⁶	0	Phosphorus donor, LiO
17	"	1x10 ¹⁶	1x10 ¹⁷	Si-G8
18	"	1x10 ¹⁶	2x10 ¹⁷	Si-G8
19	"	3.6x10 ¹⁶	2x10 ¹⁷	Si-G8
20	"	3.6x10 ¹⁶	2.5x10 ¹⁷	Si-G8

*All irradiations were done at T ≤ 150°K.

Figure 21 shows the resistivity, measured by four-probe technique, versus isothermal anneal time at 295°K for the samples listed in Table 2. Independent measurements indicate a $\pm 12\%$ uncertainty in these measurements. Except for sample 19, which shows an initial resistivity increase, the resistivity at 295°K remained relatively constant for about 4 hours, and then appeared to increase, indicating a loss of carriers. ESR data on sample 14 indicate that the Si-G8 center concentration is the same after one day at room temperature as it is after about three minutes at 295°K.

Figures 22 and 23 indicate the results of 15-minute isochronal anneals at elevated temperatures up to 673°K. Figure 22 indicates the change in room-temperature resistivity, which is inversely proportional to carrier concentration, and Fig. 23 shows the change in concentration of paramagnetic centers. Figure 22 indicates a decreasing carrier concentration after 15-minute anneals up to about 373°K, followed by an increase after 15-minute anneals above 373°K.

The rapid increase in carrier concentration between 573° and 673°K in the 1:1, Li:P (sample 18) material, as opposed to the 3:1, Li:P (sample 20) material, might be due to the annealing of a lithium-related defect located below the Si-G8 (phosphorus-vacancy) level at 0.4 eV. In non-lithium-diffused silicon, the Si-G8 center anneals between 425° and 473°K; however, as indicated in Fig. 23, a large number of unidentified paramagnetic centers are still present after 15-minute anneals of from 473° to 673°K. Unfortunately, the resonance signal produced by these centers does not have enough structure to allow identification with our 9.2-GHz spectrometer.

In Fig. 22, the decreasing carrier concentration between 300° and 373°K could be due to the creation of acceptors below ($E_c - 0.4$) eV. Such a decrease was previously observed in QC material during a Si-B1 center study.⁽¹⁾ The increase in carrier concentration between 373° and 673°K is due to the annealing of the Si-G8 and perhaps other deeper centers. Since an absolute measure of the number of paramagnetic defects observed by ESR techniques is difficult, the defect densities in Fig. 23 were normalized to the number of phosphorus atoms initially present in the

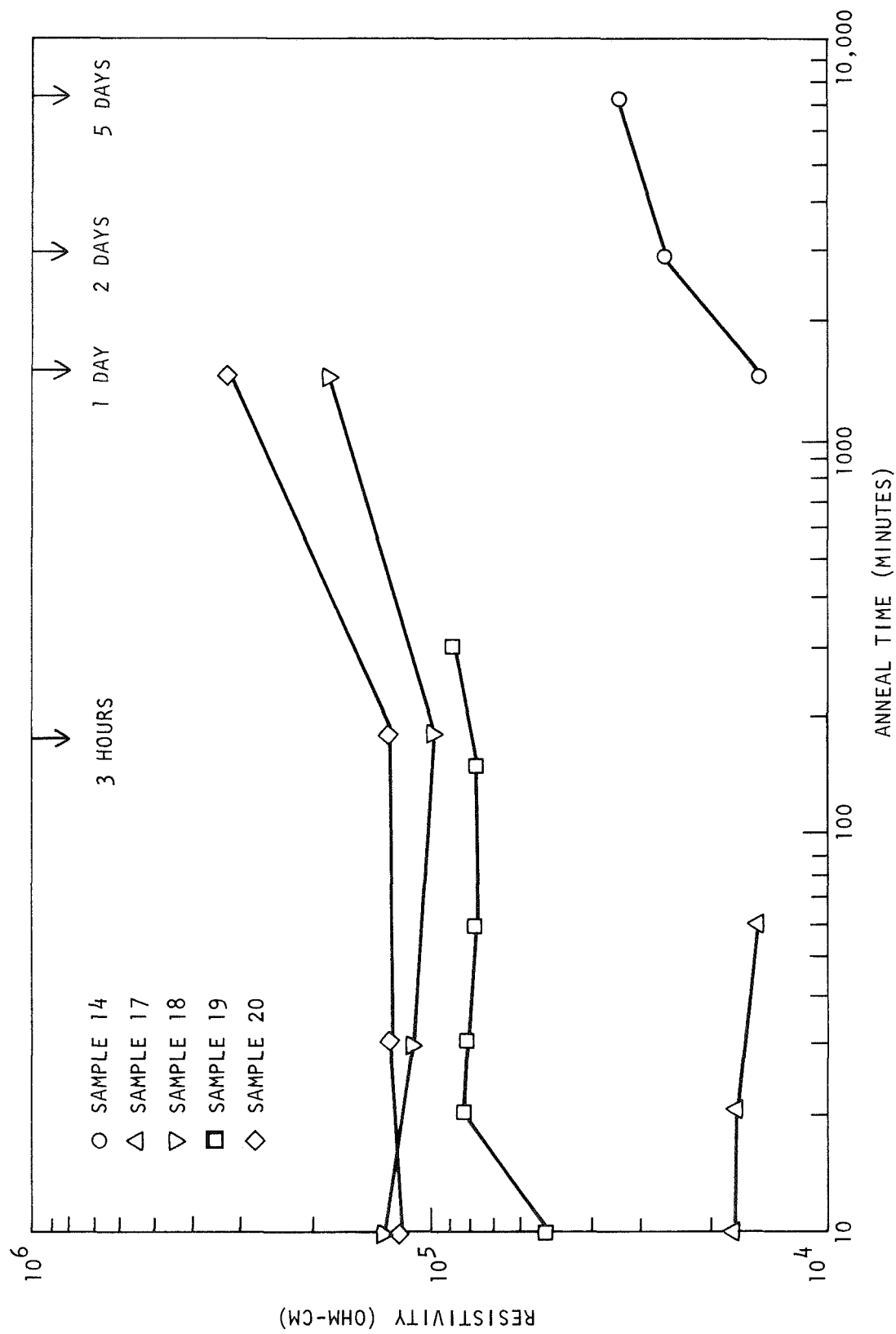


Fig. 21 Resistivity of electron-irradiated lithium-diffused silicon versus 295°K storage time

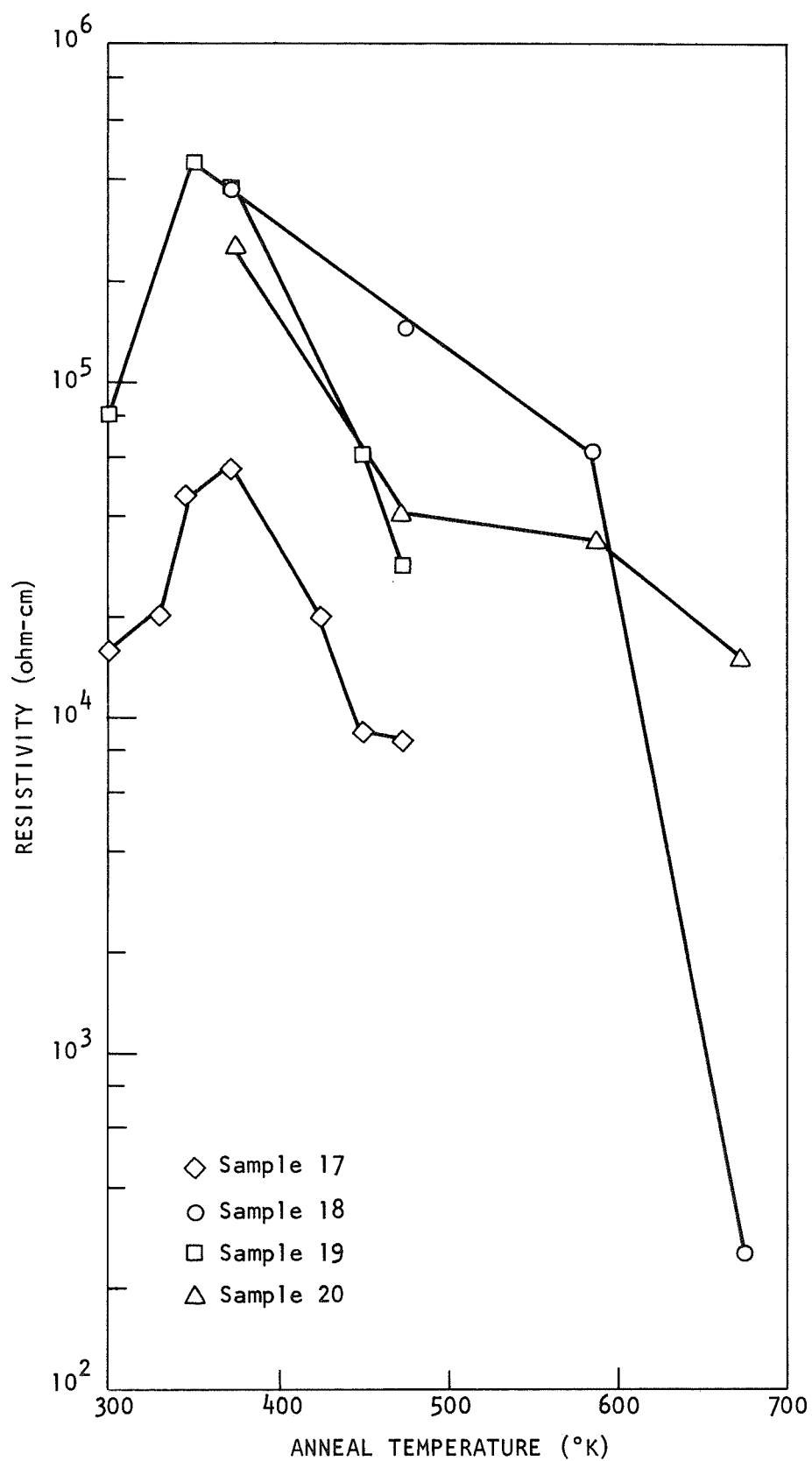


Fig. 22 Resistivity after 15-minute isochronal anneals for lithium-diffused electron-irradiated silicon

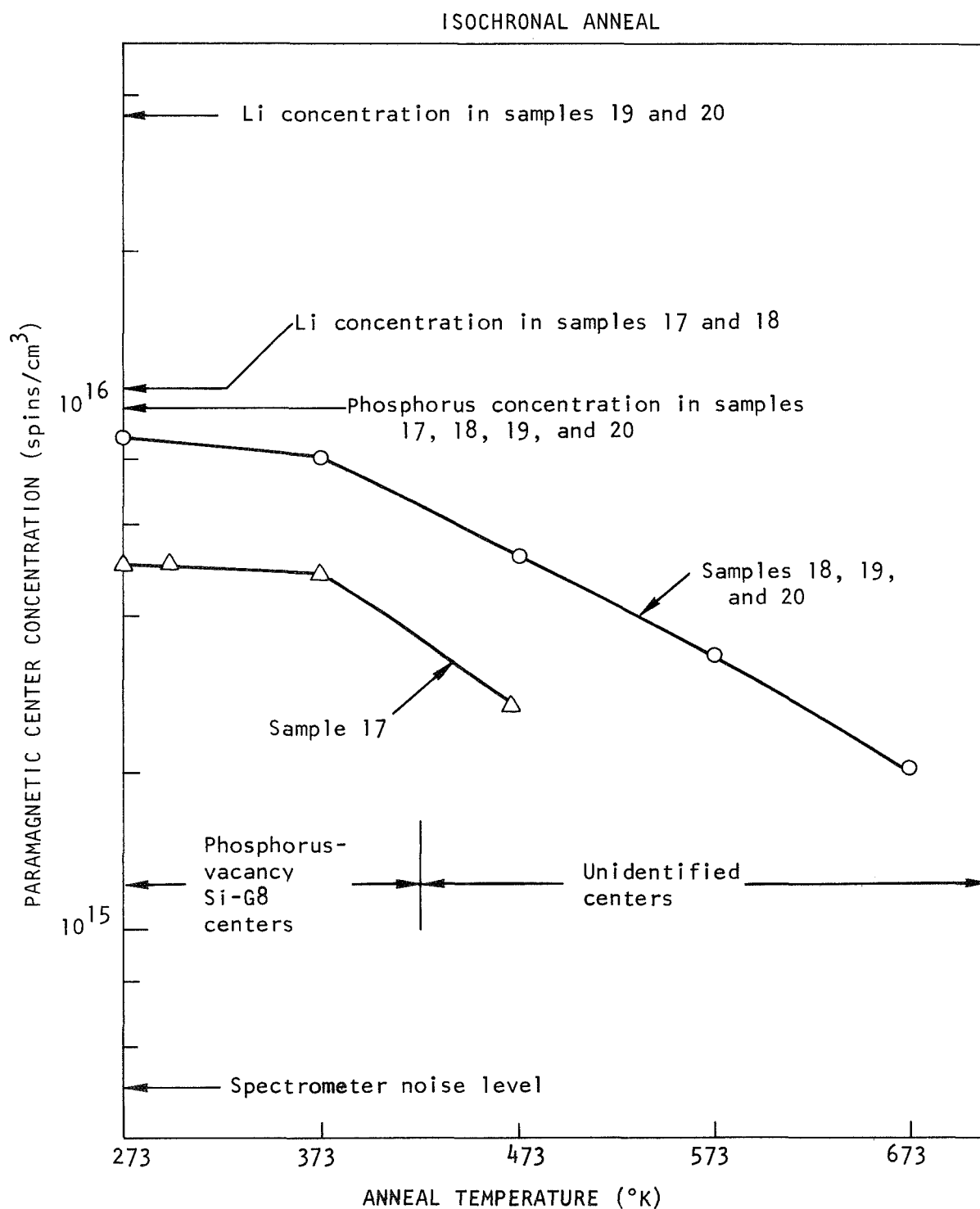


Fig. 23 Density of paramagnetic centers after 15-minute isochronal anneals for lithium-diffused, phosphorus-doped, electron-irradiated silicon

sample (as determined by four-probe resistivity measurements). This assumes that Si-G8 center production was in saturation at fluences of 2×10^{17} e/cm².

Since the Si-G8 anneals in the region of 425° to 475°K in non-lithium-diffused material,⁽³⁶⁾ examination of Fig. 23 reveals that the addition of the above concentrations of lithium does not have a significant effect on the annealing behavior of the Si-G8 center.

5.1.4 Conclusions

Several conclusions can be drawn from the data.

1. Since the same number of phosphorus donors was observed before and after lithium diffusion, it appears that the phosphorus does not pair with the lithium. The absence of a lithium-phosphorus complex leaves the phosphorus free to combine with the radiation-produced vacancy to produce the Si-G8 center.

2. At the high fluences required to observe the Si-G8 center, the introduction rate is the same in silicon with lithium donor densities as high as 3.6×10^{16} /cc as it is in silicon with no lithium. Thus, either the radiation-produced mobile vacancy is preferentially attracted to the phosphorus rather than to the lithium or all the lithium has been used up at these high fluences to produce radiation-induced complexes which do not compete with the phosphorus. The former supposition implies that phosphorus has a larger cross section for the vacancy than does lithium. This is in contrast with the earlier work on the Si-B1 and Si-G7 centers where, for 300°K irradiations, the effect of adding lithium is to decrease the introduction rates of these centers.

3. For these heavily irradiated samples, the Si-G8 center anneals between 425° and 475°K, in spite of the lithium present. As with the introduction rate, this can imply either (1) that lithium has no effect on the annealing of the Si-G8 center, or (2) that all the lithium initially present was used up by other radiation defects and, hence, not available to interact with the phosphorus vacancy.

5.2 INFRARED ABSORPTION STUDIES

As described in Section 5.1.1.2, ESR was used to search for the divacancy in lithium-diffused silicon. No resonance was observed. It was concluded that the reason for this failure was either a lower divacancy introduction rate in lithium-diffused silicon or the presence of divacancies in a nonparamagnetic charge state. To resolve this uncertainty, an infrared absorption study was carried out.

The infrared absorption measurements were performed using a Perkin-Elmer model 112 double-pass prism spectrometer. This instrument is equipped with various light sources (a tungsten lamp and a Globar), prisms (glass, fused quartz, NaCl, and CsBr), and detectors (photoconductive cells and thermocouples) that allow it to cover the wavelength region from ultraviolet to about 30 μm . The spectrometer has been modified so that the monochromatic beam can be extracted and the sample positioned in either the monochromatic beam or the white light.

Infrared absorption is less sensitive than ESR, requiring approximately 10^{16} defects/ cm^3 for bands to be observed. However, this technique has the advantage that the divacancy bands⁽³⁷⁾ are observed regardless of the divacancy charge state. The sample was placed in the white light beam of the Perkin-Elmer spectrometer and observed using fused quartz and NaCl prisms in the wavelength region from 1 to 4 μm .

Infrared absorption bands at 1.8, 3.3, and 3.9 μm have been correlated with the divacancy.⁽³⁷⁾ The bands which are seen depend on the Fermi level position as shown by Fan and Ramdas.⁽³⁸⁾ Figure 24 indicates this dependence; the shaded areas indicate the range of Fermi level position over which each band is seen.

Two lithium-diffused optical samples and two nondiffused control samples were prepared from 10^4 -ohm-cm FZ silicon. The sample dimensions were 2 x 4 x 10 mm. The samples were diffused by the paint-on technique to a lithium donor density of about 5×10^{16} Li/cc. They were irradiated with 30-MeV electrons to a fluence of 2.5×10^{17} e/ cm^2 . The samples were immersed in liquid nitrogen during irradiation, and their temperature never exceeded 150°K. After irradiation, the samples were transferred

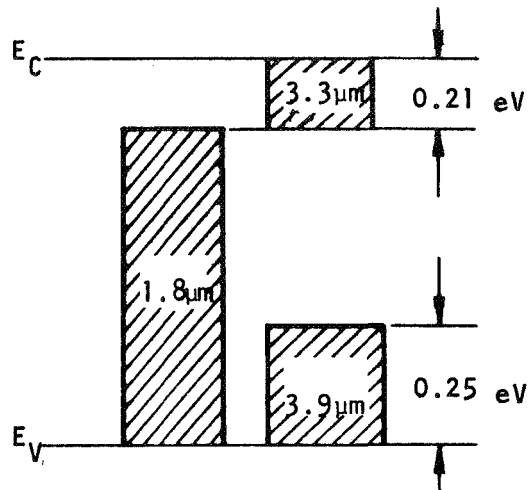


Fig. 24 Divacancy model

(still at 77°K) to an optical dewar and optically scanned in the Perkin-Elmer spectrometer in the 1.1- to 5- μ m range. Both the diffused and the nondiffused samples showed comparable absorption in the 1.75- to 1.8- μ m region, as shown in Fig. 25 (curves A). This absorption is attributed to the divacancy when the Fermi level is below ($E_c - 0.21$) eV.

The samples were annealed at room temperature for 15 minutes while being dried with dry nitrogen. On reexamination at 77°K, the 1.8- μ m band in the lithium-diffused sample was found to be greatly reduced, and there was enhanced absorption near 1.4 and 1.65 μ m. Annealing the samples below room temperature was impossible with the equipment being used. The samples were then warmed to room temperature again and immediately examined in the 1.1- to 2.5- μ m region. After less than 30 minutes at 300°K, the 1.8- μ m band had virtually disappeared in the lithium-diffused sample, and bands near 1.4 and 1.65 μ m had appeared. These bands have previously been observed by Young et al.⁽³⁹⁾ in lithium-diffused silicon. The primary difference between this investigation and Young's is that Young irradiated near 300°K rather than near 150°K, and several days elapsed between irradiation and observation; hence, the 1.8- μ m divacancy band he observed was considerably less dense than the one we observed. Young's samples had undergone 300°K annealing before his measurements

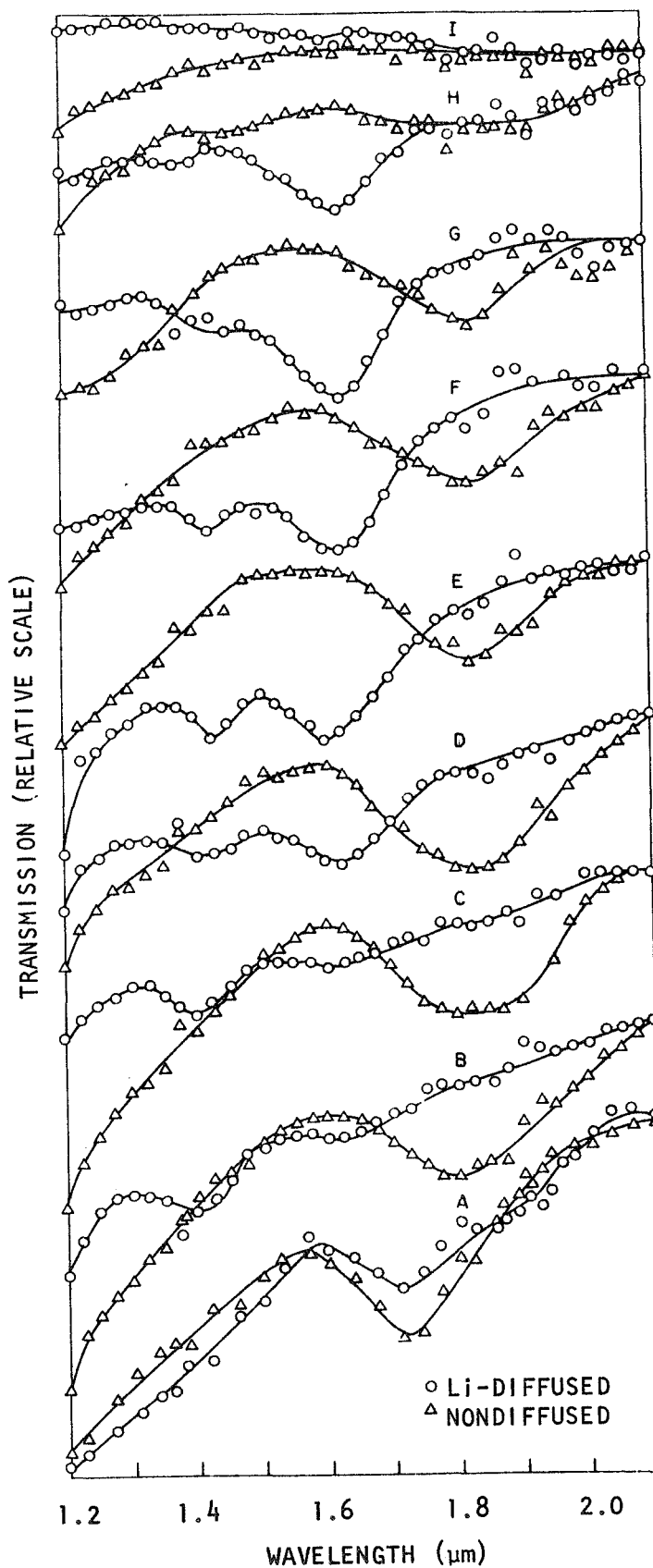


Fig. 25 Relative transmission of high-purity FZ (10^4 -ohm-cm) and high-purity Li-diffused ($n_0=5 \times 10^{16}$ Li/cc) FZ silicon after irradiation with 2.5×10^{17} e/cm² (30 MeV) at $<150^\circ\text{K}$. Curves A and B normalized to tungsten light source; other curves normalized to transmission through 10^4 -ohm-cm nonirradiated sample. History of samples given in Table 2.2. Resolution better than $0.02 \mu\text{m}$.

commenced. Our samples were isochronally annealed for 15-minute periods in 50°C steps from ~400° to ~625°K. The results of this anneal are substantially in agreement with those of Young et al.

Young et al. attribute the 1.4- and 1.65-μm bands to defect complexes consisting of one and two Li⁺ ions, respectively, which are trapped by a divacancy.

It is clear from Fig. 25 that the Si-G7 anneals at much lower temperature in lithium-diffused silicon than in non-lithium-diffused silicon; in nondiffused silicon, it anneals near 625°K.^(37,40)

Table 3 presents the annealing history of the samples used in the divacancy study.

Table 3
ANNEALING HISTORY OF SAMPLES USED IN DIVACANCY STUDY

Curve Designation (Fig. 25)	Sample Temperature (°K)	Anneal Temperature (°K)	Anneal Duration
A	77	<150	Intermittent during irradiation
B	300	300	<30 minutes
C	300	300	12 hours
D	300	398	15 minutes
E	300	448	15 minutes
F	300	473	15 minutes
G	300	523	15 minutes
H	300	573	15 minutes
I	300	623	15 minutes

6. USE OF COMPUTER PN CODE FOR PREDICTING PERFORMANCE OF SOLAR CELLS

6.1 INTRODUCTION

Although measurements under this contract were done on bulk silicon diffused with lithium, the desired ultimate goal is an operating device—namely, a solar cell—that is resistant to radiation damage. Therefore, in addition to measuring changes in the electronic properties of bulk materials due to damaging radiation and annealing, it is important to be able to predict the effect of such changes on the device performance. The conventional analyses of solar cell performance have usually taken two approaches. In the first, the short-circuit current (I_{sc}) of the solar cell is calculated based on diffusion theory, assuming uniform carrier lifetimes (or diffusion lengths) on the two sides of an estimated depletion region.^(41,42) The second approach consists of fitting experimental data to the solar cell current-voltage (I-V) equation,^(43,44)

$$I = I_{sc} - I_0 (e^{V/V_0} - 1) , \quad (8)$$

to empirically determine the unknown parameters: V_0 , the diode characteristic voltage; I_0 , the reverse saturation current; and I_{sc} , the short-circuit current.

While both of these methods can yield useful results for certain purposes, they both have shortcomings for application to radiation damage studies. Although the first method attempts to relate performance to the bulk material properties of the device (for example, lifetimes, diffusion constants, generation rate of excess electron-hole pairs, etc.), it is usually necessary to assume that the parameters are constant on either side of the junction. Thus, it is difficult or impossible to correctly simulate the effects of nonuniform damage or the attenuation of the light intensity with depth into the device. Also, it is usually necessary to make other simplifying assumptions—for example, quasi-charge neutrality

in the bulk of the device, zero-carrier densities at the edge of the depletion region, and no recombination in the depletion region. Moreover, this method is strictly applicable only to short-circuit conditions, and attempts to predict performance as a function of load would require additional assumptions. On the other hand, the solar cell equation (Eq. 8) predicts the device performance versus load, but it is difficult to relate the empirically determined parameters of the equation to the properties of the material, especially if the radiation damage is not uniformly distributed throughout the device. Thus, one needs a new method, one which predicts the output of a solar cell as a function of its external load, the basic material properties, and the distribution of damage.

Under government contracts,* Gulf Rad Tech has developed a computer code called PN^(45,46,47) which is ideally suited for this problem. This code is operational and was previously used to investigate a number of problems involving transient ionization effects in electronic devices. With no modifications, it can be used to predict the steady-state I-V characteristics of solar cells with arbitrary doping profiles, spectral light intensity, nonuniform radiation damage, etc. It can include the degradation of carrier lifetimes with radiation fluence and the annealing of this damage with time. For most solar cell applications, the damage is introduced so slowly compared to the annealing rate that only steady-state damage constants are necessary. An earlier version of the code is described in detail in Ref. 46, but some additional features that are useful for simulation of solar cells were added during the past year.⁽⁴⁷⁾ The general features of the code that are of interest for solar cell problems are described briefly in Section 6.2.

Section 6.3 is concerned with the application of the PN code to generating realistic I-V characteristics for a 10-ohm-cm N-on-P solar cell. This included a study of how varying input parameters such as doping, lifetimes, and generation rates affect solar cell output. Analytical expressions, which hold for open-circuit voltage and short-circuit current, are compared with computer code results.

*Sponsored by the Air Force Weapons Laboratory and the Defense Atomic Support Agency.

In Section 6.4, the computer PN code is used to calculate the degradation of performance for a solar cell exposed to 300-keV protons, which produce nonuniform damage. The results are shown to be in agreement with experimental results.

6.2 DESCRIPTION OF PN CODE

The PN code is applicable to devices that can be approximated in one dimension, either linear in rectangular geometries or radial in cylindrically or spherically symmetric geometries. In the following, the discussion will be confined to the linear geometry.

The basic equations that are solved by the computer for the interior of the device are the one-dimensional continuity equations for the two charge carriers, n and p ,

$$\frac{\partial n}{\partial t} = g - r - \frac{\partial J_n}{\partial x}, \quad (9)$$

$$\frac{\partial p}{\partial t} = g - r - \frac{\partial J_p}{\partial x}, \quad (10)$$

and Poisson's equation for the electric field E ,

$$\frac{\partial E}{\partial x} = \frac{4\pi q}{\kappa} [p - n + \Delta N]. \quad (11)$$

In these equations, n is the density of electrons in the conduction band, p is the density of holes in the valence band, ΔN is the net density of doping of the semiconductor (positive for donors, negative for acceptors), q is the magnitude of the electronic charge (1.6×10^{-19} C), and $\kappa = 4\pi\epsilon\epsilon_0 = 1.33 \times 10^{-11}$ f/cm for silicon. The term g is the generation rate of electron-hole pairs due to the incident radiation, and r is the recombination rate of excess electrons and holes. These terms may depend on time and position. Usually, the recombination rate is simulated by a Shockley-Read⁽¹¹⁾ type of equation of the form

$$r = \frac{n p - n_0^2}{\tau_{n_0} (p + p_F) + \tau_{p_0} (n + n_F)}, \quad (12)$$

where n_0 is the intrinsic carrier density, n_F and p_F are the values of

n and p when the Fermi level coincides with the energy level of the recombination center, and τ_{n0} and τ_{p0} are the low-injection-level recombination lifetime of electrons in heavily p-type material and of holes in heavily n-type material, respectively. However, more complicated types of recombination, including trapping, are available if desired. For radiation damage and annealing, τ_{n0} and τ_{p0} change with fluence and time. The quantities J_n and J_p are the particle current densities given by

$$J_n = n v_n - D_n \frac{\partial n}{\partial x} = \mu_n [-n E - \left(\frac{kT}{q}\right) \frac{\partial n}{\partial x}] , \quad (13)$$

$$J_p = p v_p - D_p \frac{\partial p}{\partial x} = \mu_p [+p E - \left(\frac{kT}{q}\right) \frac{\partial p}{\partial x}] . \quad (14)$$

The E (or velocity v) terms are the drift currents with mobilities μ_n and μ_p , and the $\partial/\partial x$ terms are the diffusion currents with diffusion coefficients D_n and D_p . Temperature enters the problem by Einstein's relation between the μ 's and the D 's and in the values of n_0 , μ_n , μ_p , τ_{n0} , τ_{p0} , n_F , and p_F . In these equations, n , p , g , τ_{n0} , τ_{p0} , and E can be functions of time and position, while ΔN , μ_n , and μ_p are constant in time but are functions of position.

The device is connected to an external circuit that can include various arrangements of batteries, resistances, capacitances, and inductances. However, for solar cell applications, the external circuit will normally consist of a single resistance connecting the two ends of the device. The code calculates the current in the external circuit by summing voltages around the loop, including internal electric fields inside the device and contact potentials at the two contacts, and dividing by the external resistance. The boundary conditions require that the external current equal the internal current inside each end of the device.

Several types of boundary conditions at the contacts are available. One, called "bulk" condition, forces the slope of the carrier densities to be zero at the boundaries. This condition is suitable if the details of the boundaries are not important. However, if differences in the work functions of the semiconductor and contacts are important, the "bulk" contact potentials, which are included automatically in the code as a function

of doping to give the proper summation of voltages around the circuit, can be modified to account for the difference in work functions. Finally, to simulate ohmic contacts, a thin region of high recombination rate was inserted at each contact.

To solve the time-dependent partial differential equations, they are converted into finite difference forms, and the resulting algebraic equations are solved by iteration for finite-time step intervals. The details of the differencing and iteration procedures are described fully in Refs. 46 and 47 and will not be repeated here. Suffice to say, the transient and steady-state solutions obtained from the code give excellent checks with problems that can be solved analytically. The mesh distribution for the finite differences is arbitrary, but the permissible total is limited to 230 stations by the capacity of the UNIVAC 1108 computer. This number is quite adequate for simulating a solar cell. The mesh spacing can be made small where the variables are changing rapidly with position, such as near junctions, and they can be spaced further apart where the variables are changing more slowly. The code has an automatic remesh feature in case the densities change more rapidly than a specified ratio between adjacent mesh stations.

To start a new problem, the code starts from an arbitrary but mathematically consistent set of distributions of densities and electric fields. This initial distribution is usually physically unrealistic, but the code then proceeds in time to the correct physical situation depending on the input parameters. If one then desires to make a small change to the system, such as changing the external resistance, it is usually permissible to start from the end of the previous run and make the change, rather than starting over from the arbitrary initial distribution.

The advantages of this code over most other methods of analysis are (1) it is not necessary to make arbitrary assumptions about the boundary conditions at the edge of the depletion region or about quasi-charge neutrality in various regions of the sample, (2) recombination inside the depletion region can be considered, and (3) the doping profile and the distributions of recombination centers and carrier generation rate inside the sample can be simulated to any reasonable degree of complexity. Thus,

the user has the assurance that what he obtains from the computer is not a byproduct of some dubious assumption that he may have had to make in order to obtain a solution but is the rigorously correct solution for the equations of the system, within the accuracy of the finite difference approximations.

6.3 APPLICATION OF CODE TO A TYPICAL SOLAR CELL

The first task set for the code was to see if it could reproduce a typical solar cell I-V characteristic curve. The cell that was simulated is an N-on-P cell with 10-ohm-cm base material; the area is 2.0 cm^2 with three electrical contacts on the front face. The real cell was manufactured by Texas Instruments, Inc. (TI), and is described in a TI bulletin.⁽⁴⁸⁾

There were several physical parameters that were unspecified in Ref. 48. For lack of better information, the doping profile on the N side was rather arbitrarily assumed to be the complimentary error function solution to the diffusion equation with a surface concentration of 10^{19} cm^{-3} diffused to give a junction depth of $0.5 \text{ }\mu\text{m}$. In the following section, a step-function doping density was assumed in order to compare PN code predictions with analytical expressions which are only valid for uniform doping densities on each side of the junction.

The lifetimes must also be supplied to the code. On the N side, it was assumed that the un-ionized fraction of the donors, of density N_u (cm^{-3}), acts as a recombination center, and the minority-carrier lifetime, τ_p (in sec), is

$$\tau_p = 1/(v_p \sigma_p N_u) . \quad (15a)$$

The value of the majority-carrier lifetime, τ_n , has an insignificant effect on the recombination rate, and almost any value could be used. For simplicity, it was also taken of the form

$$\tau_n = 1/(v_n \sigma_n N_u) . \quad (15b)$$

In Eq. 15, v is the thermal velocity and σ is the capture cross section. A nominal value of 10^7 cm/sec is used for v_p , and the velocity v_n is then found from

$$v_n = v_p \sqrt{m_p/m_n} = 0.82 v_p . \quad (16)$$

The specific value 0.82 is obtained from the density-of-states masses. The value of the cross sections, σ , depends on whether the center is charged or neutral for that particular capture. In fact, near room temperature the two cross sections appear to differ very little⁽¹²⁾ and, for the following, we have assumed them both to be equal to $5 \times 10^{-16} \text{ cm}^2$.

Since the doping density N decreases from $10^{19}/\text{cc}$ at the surface to the order of $10^{15}/\text{cc}$ at the junction, τ_p varies from $2 \times 10^{-11} \text{ sec}$ to the order of $3 \times 10^{-7} \text{ sec}$.

The doping in the base was initially taken to be $1.5 \times 10^{15} \text{ cm}^{-3}$ from Irvin's⁽⁵⁾ data of resistivity versus doping, but it was later found necessary to assume a density of $5 \times 10^{15} \text{ cm}^{-3}$ in order to match the open-circuit voltage reported in Ref. 48. The electron lifetime in the base region was varied as described in Section 6.4 to obtain a short-circuit current of about 30 mA/cm^2 . The final value that was chosen was $\tau_n = 7.3 \text{ } \mu\text{sec}$, which yielded a current of 28.8 mA/cm^2 .

The generation rate $g(x)$ (in $\text{cm}^{-3}\text{-sec}^{-1}$), was found by following Kleinmann⁽⁴²⁾ and integrating over the entire effective solar photon flux $N(\lambda)$ (in $\text{photons/cm}^2\text{-sec-}\mu\text{m}$):

$$g(x) = \int_{0.42}^{1.08} N(\lambda) \alpha_{\lambda} e^{-\alpha_{\lambda} x} d\lambda , \quad (17)$$

where α_{λ} is the absorption coefficient in cm^{-1} and λ is the wavelength in μm . The limits on the integral are Kleinmann's and correspond to limits imposed by the band gap and optical absorption. The TI test cell was measured under air mass one (AM1) conditions. The energy absorbed by the atmosphere is relatively large in the bandgap region of silicon, so Eq. 17, which is based on air mass zero (AM0), was appropriately reduced.

The main objective of this test to simulate a solar cell has been fulfilled, as is shown in Fig. 26, where the calculated I-V curve is compared with the measured I-V curve.

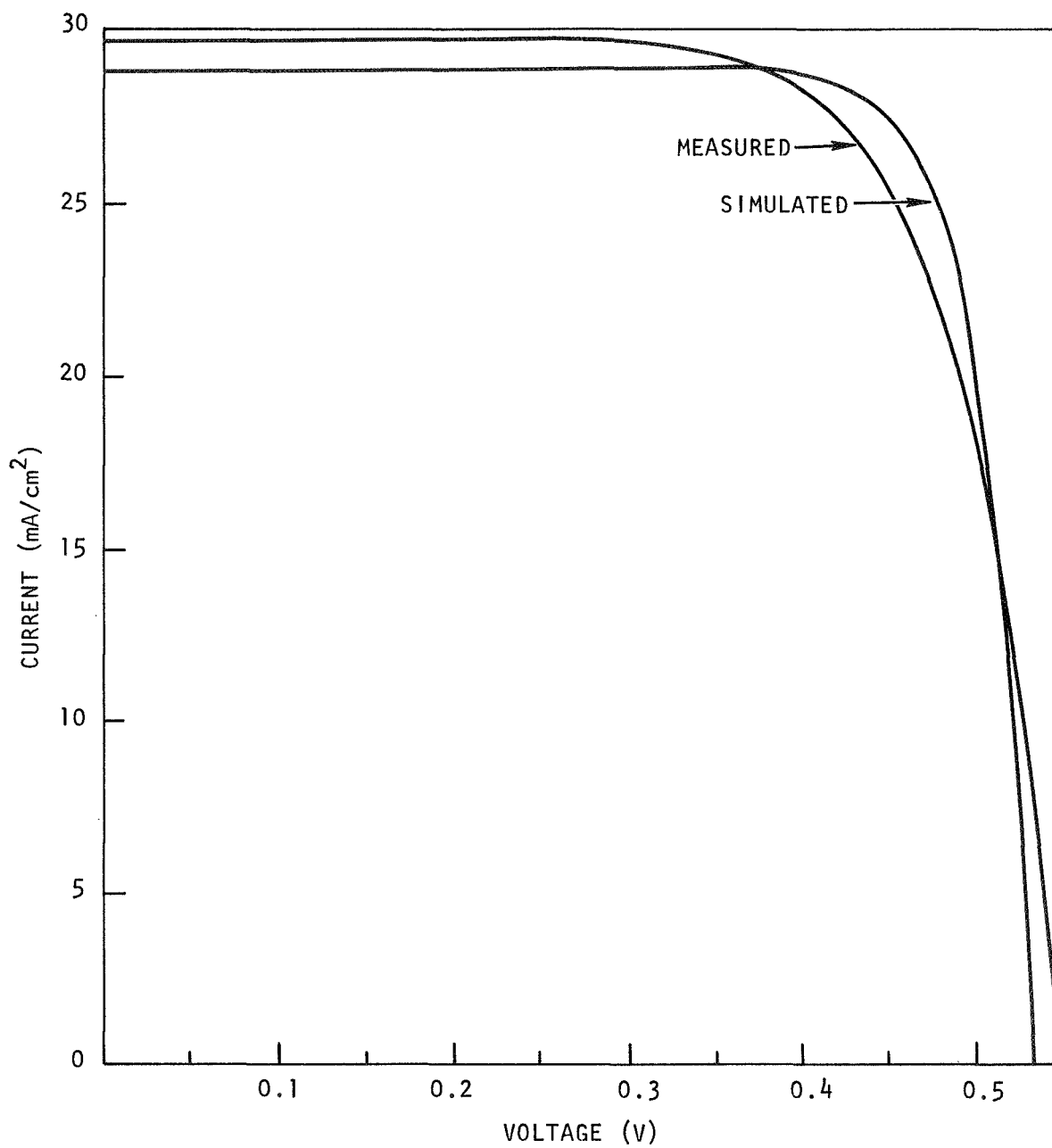


Fig. 26 Measured I-V curve compared with cell simulated by the PN code. Both cells are graded junction in AM1 sunlight.

6.4 DEPENDENCE OF ELECTRICAL OUTPUT ON PHYSICAL PARAMETERS

Some of the more important inputs to the PN code are the doping, junction depth, lifetime, etc. In order to fully understand the operation of a cell, it is necessary to know how these parameters affect the electrical output of the cell. Various calculations, applicable to special cells, appear in the literature. A few computer runs were undertaken to test some of these analytical expressions.

The analysis of Wysocki and Rappaport,⁽⁴⁹⁾ for example, can be used to obtain an approximation* for the open-circuit voltage, V_{oc} ,

$$V_{oc} \approx (kT/q) \ln (I_{sc}/I_0) . \quad (18)$$

In Eq. 18, I_0 is the reverse saturation current for an ideal diode,

$$I_0 = qn_i^2 (L_n/\tau_n N_A + L_p/\tau_p N_D) . \quad (19)$$

In Eq. 19, the diffusion lengths L (in cm) are

$$L = \sqrt{D\tau} , \quad (20)$$

N_A and N_D are doping densities on the P and N sides, respectively, and n_i is the intrinsic carrier concentration. We shall later find (cf. pp. 85, 86) that, under solar illumination, I_{sc} does not vary much with lifetime τ_n ; in this case, and assuming a large doping N_D , Eq. 18 predicts that V_{oc} will vary as $(kT/q) \log \sqrt{\tau_n}$. For penetrating uniform light, on the other hand, $I_{sc} \propto \sqrt{\tau_n}$ and $V_{oc} \propto (kT/q) \log \tau_n$.

6.4.1 Calculation of Open-Circuit Voltage, V_{oc} **

A different calculation of the open-circuit voltage can be made by arguing that the generation, g , will create an electron density, $g\tau_n$, in the base region. This density will fill the conduction band up to an energy E_p , given by

*The validity of this approximation rests on the fact that in Eq. 15 of Ref. 49 the ideal diode current contains a factor $\exp(qV/kT)$, while the recombination current contains a factor $\sinh(qV/2kT)$. The first term dominates the second for $V = V_{oc} \gtrsim 0.5$.

**The analytical expressions derived in this section specifically apply to a solar cell which has uniform doping densities on either side of the junction. This is consistent with a constant Fermi level on either side of the junction and a generation rate which does not depend on position.

$$g\tau_n = N_c e^{(E_p - \eta_p)/kT}, \quad (21)$$

where η_p is the Fermi level on the P side. The density of electrons in the N region, N_D , must satisfy an analogous relation

$$N_D = N_c e^{(E_n - \eta_n)/kT}. \quad (22)$$

An expression relating the energies is found by dividing Eq. 21 by Eq. 22 to find

$$g\tau_n/N_D = \exp [(E_p - E_n + \eta_n - \eta_p)/kT]. \quad (23)$$

The difference in Fermi levels represents the energy gained by transferring a single electron from one side to the other; i.e., it is qV_{oc} :

$$qV_{oc} = \eta_n - \eta_p. \quad (24)$$

The two populations of electrons, while not in thermodynamic equilibrium (if they were, $\eta_n = \eta_p$), are free to exchange electrons across the junction, until they both reach the same energy level. This is illustrated in Fig. 27. The bottom of the band on the N side is lowered by the built-in voltage, qV_b , which can be calculated from the doping densities:

$$E_p = E_n - qV_b. \quad (25)$$

The use of Eqs. 24 and 25 in Eq. 23 yields

$$V_{oc} = V_b + (kT/q)\log_e (g\tau_n/N_D) \quad (26)$$

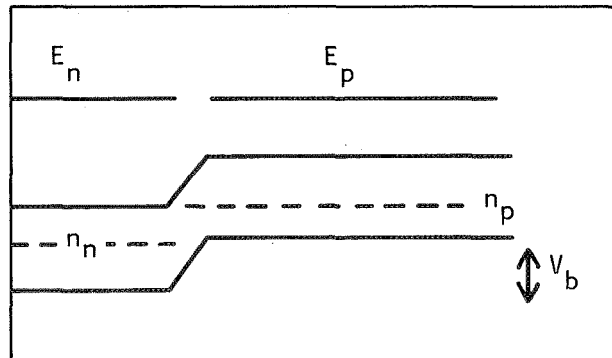


Fig. 27 Diagram showing the relative energies of carriers across an n/p solar cell junction

Note that $g\tau_n/N_D$ is less than one for all practical cases, so V_{oc} is less than V_b . (Equation 26 must become invalid as $g\tau_n/N_D$ approaches unity because V_{oc} can never exceed V_b .)

To compare the PN code predictions with the analytical expression given by Eq. 26, input parameters representing a step junction, with values given in Table 4, were supplied to the code. Open-circuit voltage versus generation rate is shown in Fig. 28. Also shown is the open-circuit voltage calculated from the empirical equation (18), where I_0 was calculated from Eq. 19 and I_{sc} was generated by the PN code. The excellent agreement between V_{oc} calculated by the PN code and Eq. 26 shows that the code correctly calculates V_{oc} in the limits imposed by this special and analytically soluble case, and gives one confidence that the code may be applied to more realistic solar cell configurations, including graded-junction devices.

Table 4
INPUT PARAMETERS FOR PN CODE
STEP JUNCTION CELL

	Doping (cm^{-3})	τ (sec)	L (cm)	$L/N\tau$ (cm^4/sec)
N side	10^{18}	2.5×10^{-9}	1.2×10^{-4}	4.8×10^{-14}
P side	1.5×10^{15}	5.0×10^{-6}	1.2×10^{-2}	1.6×10^{-12}

The graded junction does not satisfy the simple assumptions of uniform generation and doping, but both Eqs. 18 and 26 suggest that V_{oc} varies as $\log \tau$. Returning to the original solar cell configuration, which had the complimentary error function diffused junction, the relationship between open-circuit voltage (calculated by the PN code) and minority-carrier lifetime in the base τ_n is shown in Fig. 29. The values of τ_p in the base is not an important parameter; but in any case, τ_p was changed whenever τ_n was changed to keep the ratio $\tau_p/\tau_n = 0.82$. Figure 29 shows that V_{oc} does depend linearly on $\log \tau$, with a slope $\Delta V/\Delta \log \tau$ equal to about 0.0137 volt which is roughly $0.5 \times kT$. Equation 18 predicts a value of $0.5 kT$ for the case of solar illumination.

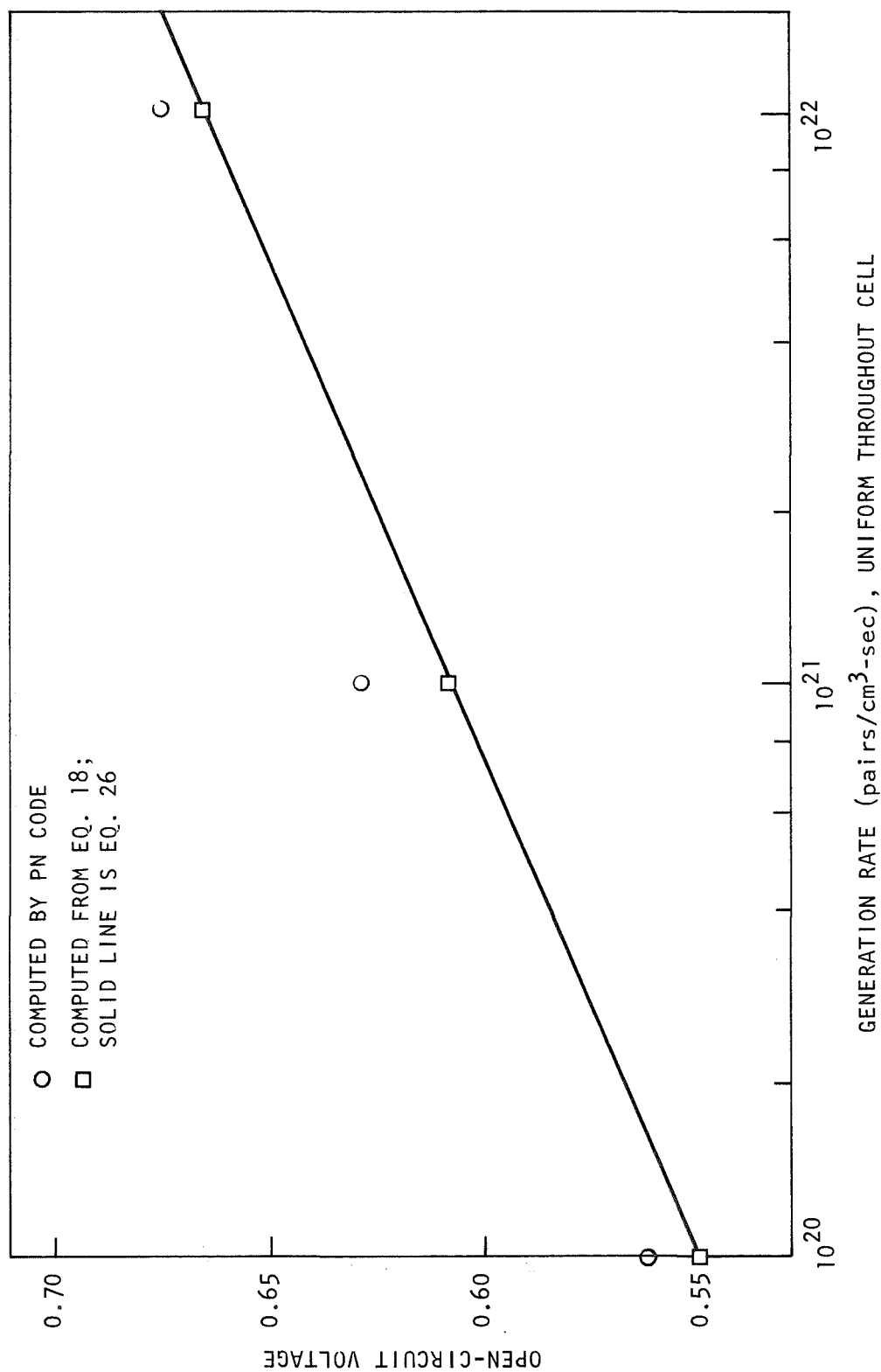


Fig. 28 V_{oc} versus g for run 310.1; $N = 10^{18} \text{ cm}^{-3}$, $\tau = 5 \text{ } \mu\text{sec}$, $kT = 0.025 \text{ eV}$ (nominal value for room temperature); built-in voltage, 0.74165 ; 10-ohm-cm base material

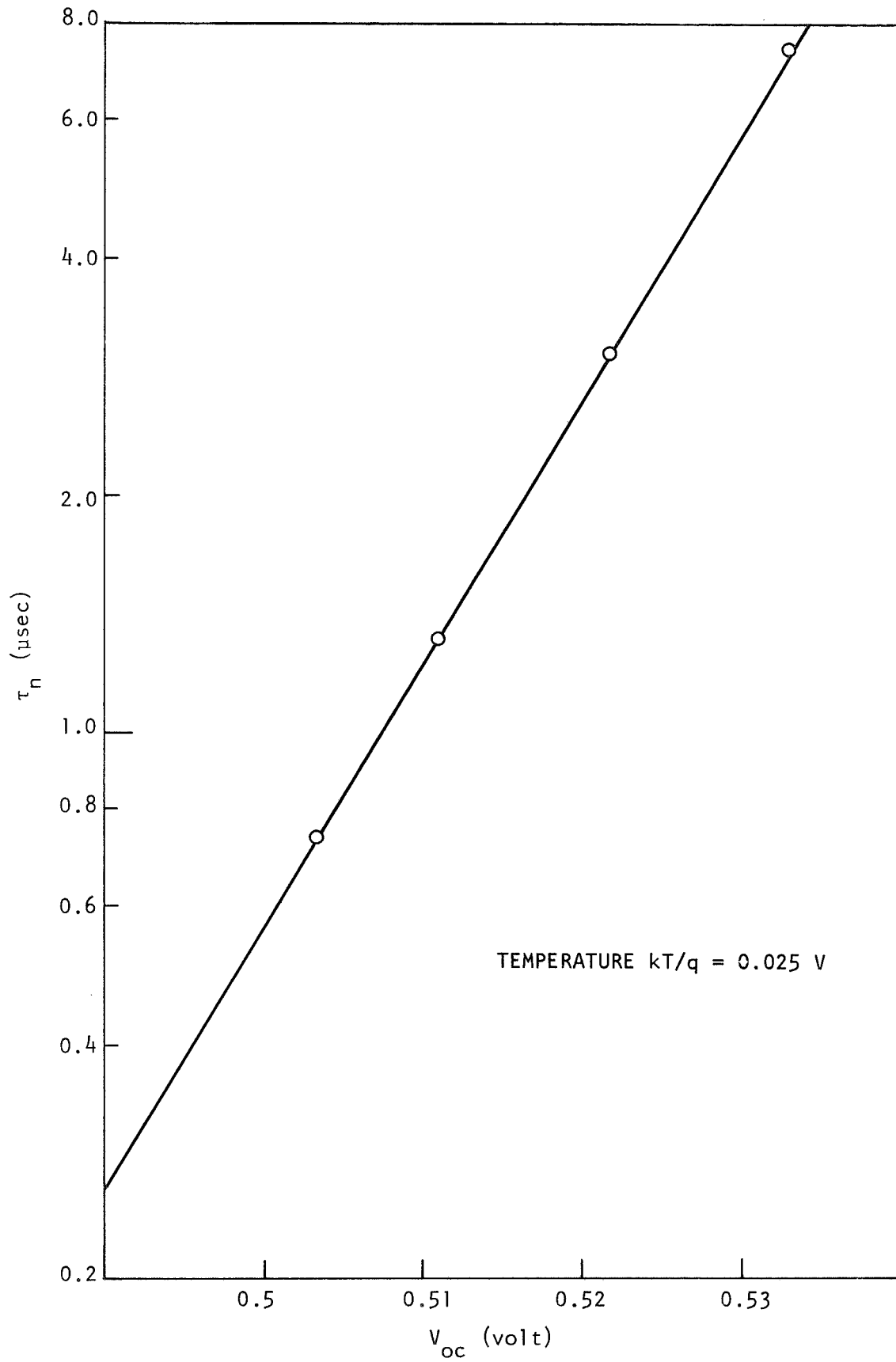


Fig. 29 Variation of open-circuit voltage, V_{oc} , with minority-carrier lifetime in the base, τ_n , as calculated by PN code. Cell is graded junction on 10-ohm-cm material, illuminated by a solar spectrum.

6.4.2 Short-Circuit Current

We now inquire into the solar cell's short-circuit current. Cooley⁽⁵⁰⁾ gives

$$I_{sc} = CL/(L + 1/\alpha) , \quad (27)$$

where C is a proportionality constant, L is the diffusion length, and α is the frequency-dependent optical absorption coefficient. Again, in order to discover whether the data calculated by the PN code exhibit any regularity, they were tested against the functional form of Eq. 27. Equation 27 was recast in the form

$$\frac{1}{I_{sc}} = \frac{1}{C\alpha} (\alpha + 1/L) , \quad (28)$$

so that, if Eq. 28 is obeyed, a plot of $1/I$ versus $1/L$ should be a straight line. Figure 30 shows that this is approximately the case for the larger values of $1/L$. The intercept indicates that C is 31.8 mA/cm^2 and the slope gives $\alpha \approx 1.45 \times 10^3 \text{ cm}^{-1}$. This number is about equal to the attenuation coefficient in the neighborhood of the spectral response peak for a solar cell with diffusion length of order 10^{-2} cm or less. The points appear to break away from the linear relation for smaller $1/L$, so Eq. 28 may not be applicable for large diffusion lengths.

The fact that Eq. 28 adequately describes a graded-junction solar cell for $L < 10^{-2} \text{ cm}$ is very useful in assessing the degradation of current by a process which uniformly changes diffusion length, neutron and high-energy electron damage being examples.

In the important case of low-energy proton damage, Eq. 28 is of no avail, so a specific computation was made for this case, as described in the next section.

6.5 COMPUTER-SIMULATED 300-keV PROTON DAMAGE

The PN code has been used to calculate the I-V output of the 10-ohm-cm N-on-P Texas Instruments cell previously discussed, after it had been exposed to normally incident 300-keV proton fluences up to $10^{15}/\text{cm}^2$. Low-energy proton radiation is taken to be typical of space radiation, and is thought to provide a stringent test for the applicability of the PN code, because of the nonuniform distribution of recombination centers produced

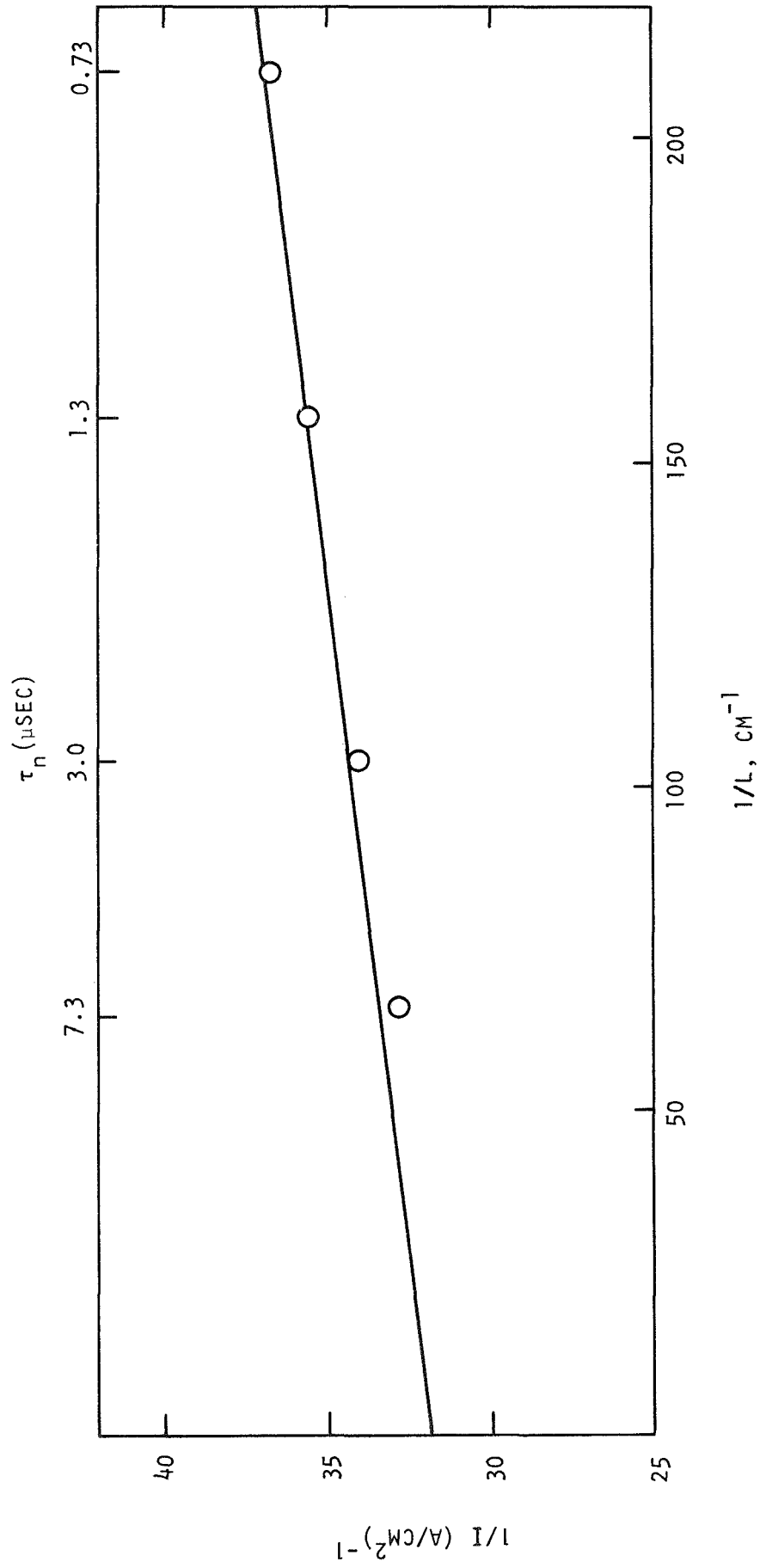


Fig. 30 PN code calculation of variation of short-circuit current, I , with minority-carrier lifetime, τ_n , where $L = \sqrt{30\tau_n}$ cm. Cell parameters other than lifetime are as for the simulation shown in Fig. 26.

by such radiation. Proton damage was simulated by adding radiation-induced recombination centers to Eqs. 9 and 10. The number of recombination centers produced depends on the proton's energy, and the proton's energy depends on its penetration depth. These recombination centers may act as carrier removal sites in addition to degrading the lifetime. Carrier removal was initially assumed to be of less importance in degrading solar cell performance than lifetime degradation; however, the influence of carrier removal was later estimated.

The variation of proton energy with depth is found from the tabulations of Janni⁽⁵¹⁾ which give the range $R(E_0)$ (in cm), of normally incident protons of energy, E_0 (in keV):

$$R(E_0) = \int_{100}^{E_0} \langle \cos \theta \rangle dE/w, \quad (29)$$

where $w = dE/dX$ is the energy loss in keV/cm and $\langle \cos \theta \rangle$ is the mean value of the cosine of the angle of the projection of the proton velocity to its original direction. If we define $R(E, E_0)$ as the range at which the proton with initial energy E_0 has energy E , then

$$R(E, E_0) = \int_E^{E_0} \langle \cos \theta \rangle dE/w = R(E_0) - R(E). \quad (30)$$

Table 5 gives $R(E)$ and $R(E, E_0)$ versus E for $E_0 = 300$ keV. The function $R(E, 300)$ is roughly linear in E .

Table 5
RANGE VERSUS ENERGY FOR LOW-ENERGY
PROTONS IN SILICON

E (keV)	$R(E)$ (cm)	$R(E, 300)$ (Eq. 30) (cm)
0	0	3.65×10^{-4}
100	1.22×10^{-4}	2.43×10^{-4}
150	1.74×10^{-4}	1.91×10^{-4}
200	2.33×10^{-4}	1.32×10^{-4}
250	3.00×10^{-4}	0.65×10^{-4}
300	3.65×10^{-4}	0

To calculate the number of defects at depth R, we used the results of Crowther et al.,⁽⁵²⁾ as extended by Barrett and Stroud.⁽⁴³⁾ References 52 and 43 use the diffusion length (L) degradation with fluence Φ :

$$\Delta(1/L^2) = K_L \Delta\Phi , \quad (31)$$

which, because of Eq. 20, can be written

$$\frac{1}{D} \Delta(1/\tau) = K_L \Delta\Phi . \quad (32)$$

In particular, Refs. 43 and 52 report the specific functional form

$$K_L(E) = (1.92/\Omega^{0.75}) e^{-1.08E} \times 10^{-5} , \quad (33)$$

where Ω is the resistivity in ohm-cm, E is the proton energy in MeV, and K_L itself has the units proton^{-1} .

The computer code requires the recombination center introduction rate, K_N , defined by

$$\Delta N = K_N \Delta\Phi , \quad (34)$$

which can also be written as

$$\Delta N = \frac{1}{\sigma v} \Delta(1/\tau) . \quad (35)$$

Combining Eqs. 32 through 35, one finds

$$K_N = (D/\sigma v) K_L = (6 \times 10^9) K_L , \quad (36)$$

if the standard values of $D = 30 \text{ cm}^2/\text{sec}$ and $\sigma v = 5 \times 10^{-9} \text{ cm}^3/\text{sec}$ are used for 10-ohm-cm material. However, a value of $K_N = (1.5 \times 10^9) K_L$ was found to give a better fit to the data of Statler and Curtin.⁽⁵³⁾ This final result can be achieved by increasing the σv product or decreasing the value of $K_L(E)$ by a factor of 4. This indicates that Eq. 33 does not accurately describe the proton degradation of the cell being simulated. This observation is consistent with the findings of Barrett and Stroud.⁽⁴³⁾

Values of K_N and ΔN for $\Phi = 10^{10}$ and 10^{15} protons/cm² are given in Table 6.

Table 6
DISTRIBUTION OF DEFECT RECOMBINATION CENTERS AS A FUNCTION OF FLUENCE
OF 300-keV PROTONS IN AN UNSHIELDED SOLAR CELL

X (μm)	E (keV)	K_N ($\text{cm}^{-1}/\text{proton}$)	ΔN ($\Phi = 10^{10}$ protons/ cm^2) (cm^{-3})	ΔN ($\Phi = 10^{15}$ protons/ cm^2) (cm^{-3})
0	300	3.73×10^3	3.73×10^{13}	3.73×10^{18}
0.65	250	3.8×10^3	2.8×10^{13}	3.8×10^{18}
1.32	200	4.0×10^3	4.0×10^{13}	4.0×10^{18}
3.65	100	5.2×10^3	5.2×10^{13}	5.2×10^{18}
3.8	0	0	0	0

Figure 31 presents a family of I-V curves calculated by the PN code for the 10-ohm-cm N-on-P cell described in detail in Section 6.3. The initial I-V output (also shown in Fig. 26) and the degraded I-V output after 300-keV proton fluences of 1×10^{13} , 1×10^{14} , and 1×10^{15} p/cm² are shown. The illumination level was one solar spectrum at air mass one (AM1), and the degraded curves were obtained by adding the spatial distribution of proton-induced recombination centers as given in Table 6 to the initial recombination center distribution selected in Section 6.3.

Figure 32 shows the degradation of short-circuit current with fluence, normalized to the unirradiated value. Both the results of the PN code and experimental results* by Statler and Curtin⁽⁵³⁾ are shown. The trend of the present calculation is quite satisfactory. The flattening with higher fluence is more pronounced in the experimental curve than in the PN computation. This may be because the damage constant tends to decrease for large fluence where carrier removal effects begin to become important.

Some effort has been devoted to investigating the effect of carrier removal on solar cell degradation. Carrier removal reflects back on lifetime by changing the injection level. Most of the specific information on carrier removal to be found in literature resulted from neutron irradiation experiments. As a first approximation, we assume that neutron damage and proton damage are sufficiently similar that neutron radiation results differ from proton damage only by some scale factor; thus, the results may differ numerically but are qualitatively identical. Appropriate corrections can later be supplied.

Buehler⁽⁵⁴⁾ has found that the resistivity, ρ (in ohm-cm), varies with fluence Φ (in particles/cm²) according to

$$\rho = \rho_0 e^{\Phi/k} . \quad (37)$$

The parameter k in Eq. 37 is

$$k = 387 \rho_0^{0.77} = 4.87 \times 10^{14} \text{ (particles/cm}^2\text{)} , \quad (38)$$

*The data of Statler and Curtin were actually on cells partially shielded, or covered by cover glasses. For the purpose of comparison with PN code predictions, their results were extrapolated to the limit of a bare cell.

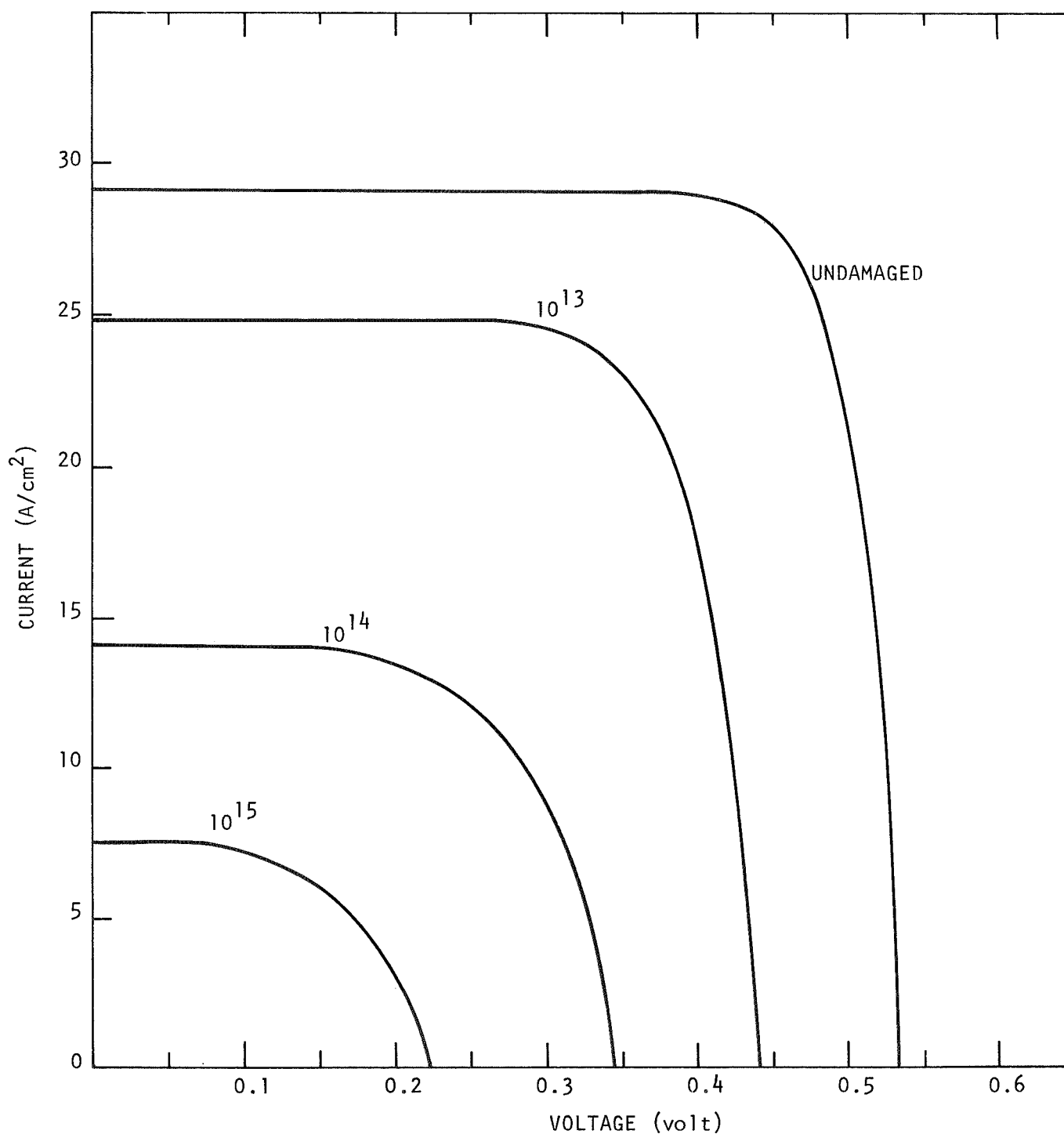


Fig. 31 Current-voltage curves of a graded-junction cell degraded by 300-keV protons to fluences as marked on curves. Undamaged cell is the one shown in Fig. 26 and discussed in Section 6.3.

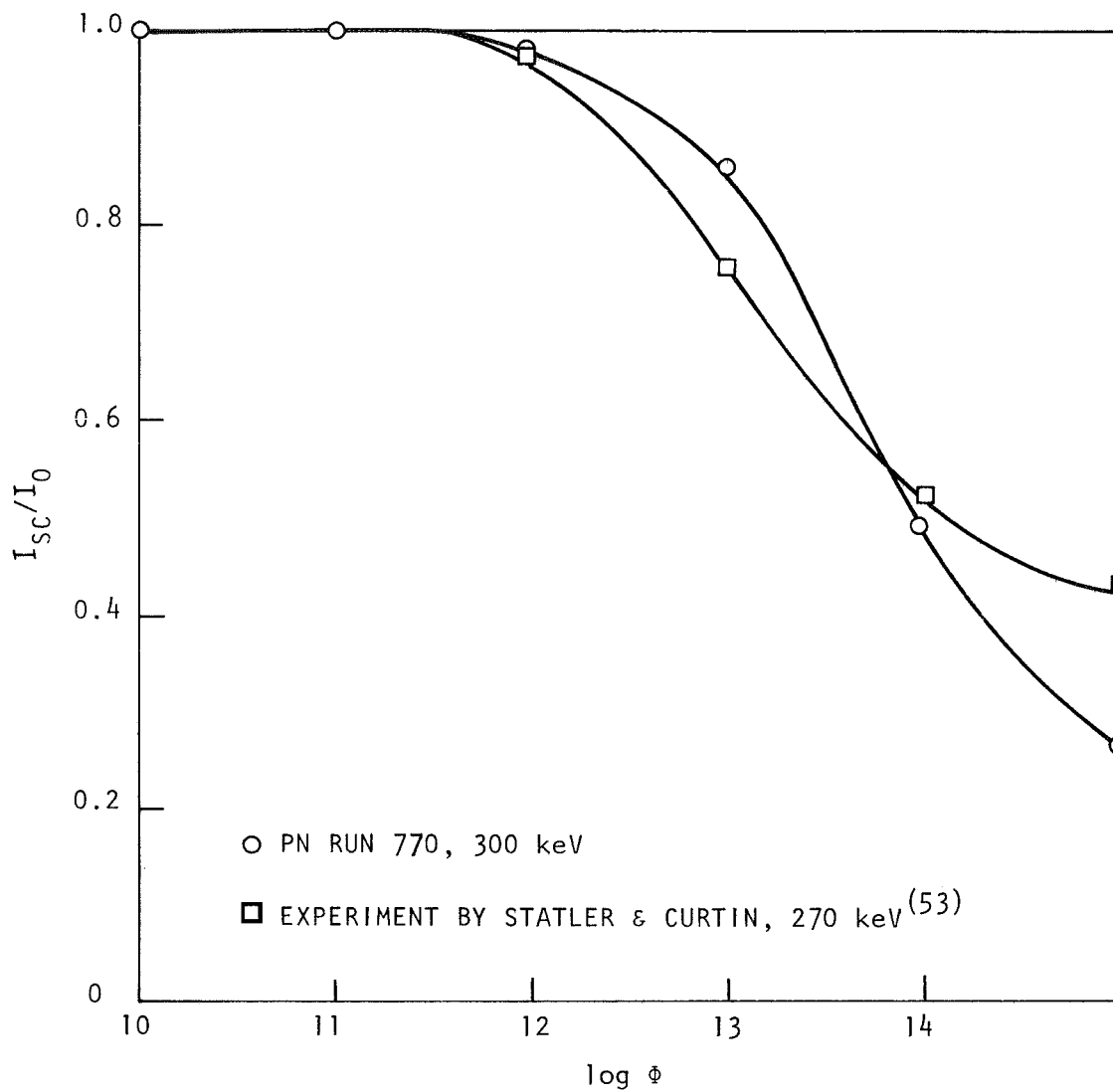


Fig. 32 Normalized short-circuit current, I_{sc}/I_0 , versus proton fluence, ϕ (protons/cm²)

where p_0 , the initial hole concentration, was taken to be $p_0 = 5 \times 10^{15} \text{ cm}^{-3}$, the value used for the simulated cell.

Gregory⁽⁵⁵⁾ has measured a lifetime degradation coefficient for neutrons, K , which he defines by

$$\Delta(1/\tau) = \Delta\Phi/K(\Phi) . \quad (39)$$

The coefficient $K(\Phi)$ is found to depend on fluence and resistivity, and a plot of Gregory's data on log-log coordinates shows that $K(\Phi)$ varies approximately as the 0.5 power of resistivity (ρ) and as the 0.2 power of injection level (n/p). The hole density, p , is proportional to $1/\rho$, so

$$K(\Phi) \approx K(0)\rho^{0.5} (n/p)^{0.2} \approx K(0)\rho^{0.7} \approx K(0) e^{0.7\Phi/k} . \quad (40)$$

The damage-induced lifetime is calculated by taking such small fluence steps that the differences can be considered to be differentials:

$$\frac{1}{\tau} = \int_0^{\Phi} d\Phi/K(\Phi) = \frac{k}{0.7K(0)} [1 - e^{0.7\Phi/k}] + 1/\tau_0 . \quad (41)$$

If $0.7\Phi/k$ is much less than one, Eq. 41 reduces to Eq. 39, but for $\Phi = 10^{15}$, Eq. 41 gives a $1/\tau$ that is 0.53 times the value found from Eq. 39. A computer run with this τ increases the current ratio shown on Fig. 32 from 0.26 to 0.31 at $\Phi = 10^{15} \text{ p/cm}^2$. The correction is in the right direction but not of sufficient magnitude to bring the ratio up to the experimental ratio of 0.44. This probably means that the effect of carrier removal on the damage constant is greater for irradiation by protons than estimated above using neutron data.

6.6 CONCLUSIONS

The above results indicate that the PN code is a very useful and powerful tool for computing the I-V characteristics of solar cells and in studying how changes in the cell, such as radiation damage, change the electrical output. The agreement between results from the PN code for an abrupt step junction and simplified analyses assures that the code will give realistic results for more complicated junctions which cannot be analyzed by the simpler techniques. In particular, the contribution to the solar cell

current due to the heavily doped face of the cell could be studied by varying the lifetime in this region. Also, the effect of nonuniform damage, such as that caused by low-energy protons, can be computed, but more work is required to determine the magnitude of some of the degradation parameters at large fluences.

7. OTHER WORK

During November of this year, several lithium-diffused silicon solar cells were irradiated with 30-MeV electrons to fluences of 3×10^{14} and 3×10^{15} e/cm² at room temperatures, for Dr. J. R. Carter of TRW Systems Group. The data from the cells are to be used in their Jet Propulsion Laboratory (JPL) program.

At the same time, a sample of 10^4 -ohm-cm float-zone silicon from the boule investigated in this contract was irradiated to intrinsic resistivity and supplied to Dr. R. J. Stirn of JPL.

8. SUMMARY OF CONCLUSIONS

The conclusions from the basic research performed on silicon are varied and help to illuminate the nature of defects in irradiated silicon. During this program, special emphasis was placed on minority-carrier lifetime measurements, since the performance of solar energy devices is largely determined by the minority-carrier lifetime. Electron-spin resonance measurements, along with infrared absorption measurements, were used to help illuminate the detailed nature of the defects.

8.1 MINORITY-CARRIER LIFETIME

8.1.1 30-MeV Electron Irradiation

The minority-carrier lifetime of 30-MeV electron-irradiated, FZ and QC lithium-diffused n-type silicon was studied. The lifetime temperature dependence, degradation rate, and annealing characteristics were measured. Both lightly diffused ($n_0 \leq 2.0 \times 10^{15} \text{ cm}^{-3}$) and heavily diffused ($n_0 \geq 1.0 \times 10^{16}$) samples were investigated. From these studies, the following conclusions can be drawn.

1. The initial preirradiation lifetime of lightly diffused FZ silicon is due to at least two centers. Its temperature dependence indicates one center of unknown charge near ($E_c - 0.17$) eV, and an attractive center deeper than 0.35 eV from either band edge. The shallow center is not the A center because, in lightly diffused FZ silicon, preirradiation lifetime measurements indicate attractive recombination centers further than 0.3 eV from a band edge, and no center near ($E_c - 0.17$) eV. Because the initial conduction electron concentration in the heavily diffused silicon was so high, the minority-carrier lifetime temperature dependence could not distinguish between the two centers if both were present. Our

measurements on heavily diffused FZ and QC silicon indicate attractive centers deeper than $(E_c - 0.17)$ eV.

2. At least two kinds of recombination centers are introduced in lightly diffused FZ silicon by the 30-MeV electron irradiation: one deeper than about 0.35 eV, which controls recombination above 150° to 200° K, and one near $(E_c - 0.17)$ eV, which is dominant below 150° to 200° K. In QC silicon, all radiation-induced recombination centers seem to be more than 0.3 eV from a band edge. The recombination centers in heavily diffused silicon are not well located but are deeper than $(E_c - 0.17)$ eV.
3. The room-temperature minority-carrier lifetime degradation constant for heavily diffused FZ and QC silicon was approximately twice that for lightly diffused or nondiffused silicon. The increased degradation constant of heavily lithium-diffused silicon compared with that of non-lithium-diffused silicon is interpreted to indicate that the presence of lithium is effective in the production of recombination centers in lithium-diffused silicon. These recombination centers either contain lithium or are affected in their production by lithium.
4. In lightly diffused FZ and QC silicon, the minority-carrier lifetime at and above room temperature is controlled by recombination through centers further than about 0.3 eV from either band edge. These centers show first-order thermal annealing near $380 \pm 20^\circ$ K, with activation energies of 0.8 ± 0.1 eV for FZ and 1.1 ± 0.2 eV for QC silicon. Effective frequency factors scale with lithium concentration.
5. In lightly diffused FZ silicon, the radiation-induced center at $(E_c - 0.17)$ eV which is dominant at low temperatures was not appreciably annealed in 1 hour at 390° K but appears to anneal, at least partially, over long periods at room temperature.
6. The annealing of the recombination centers in lightly irradiated, heavily diffused FZ and QC silicon is apparently complete.

However, after extended fluences, the annealing of the recombination centers is not complete; not all the recombination centers are annealed. Trapping centers also are created, apparently during thermal anneal, and these are not reduced by thermal annealing below 430°K. This may reflect a depletion of lithium which is able to neutralize a recombination or trapping center.

7. In general, it appears that in electron-irradiated, lithium-diffused, FZ and QC silicon, both lithium-dependent and non-lithium-dependent recombination centers are produced. The number of each depends on the lithium concentration, with the largest number of lithium-dependent centers being found in highly diffused silicon and the largest number of non-lithium-dependent centers being found in lightly diffused silicon.
8. No irradiation temperature dependence of the recombination center introduction rate for 30-MeV electrons in the 115° to 300°K temperature range was observed. However, the minority-carrier lifetime degradation constant for lithium-diffused samples irradiated and measured at 300°K is five to ten times smaller than that for samples irradiated and measured at 115°K. This may be attributed to the temperature dependence of the recombination center capture cross section.
9. Isochronal and isothermal annealing results on both FZ and QC lithium-diffused, electron-irradiated silicon indicate that the anneal is a single-stage, first-order anneal. Activation energies of 0.8 ± 0.1 eV for FZ samples and 1.1 ± 0.2 eV for QC samples were observed, which agree with the activation energies of diffusion of lithium in FZ and QC silicon,⁽²¹⁾ respectively. Effective frequency factors ranged from 10^7 to 10^{11} sec⁻¹, increasing with increasing lithium donor density. These facts strongly suggest that the thermal annealing of radiation defects in lithium-diffused silicon is due to the migration of lithium to the defect center.

8.1.2 Fission Neutron Irradiations

A number of observations can be made concerning the results of minority-carrier lifetime studies in fission-neutron-irradiated lithium-diffused silicon. First, the lifetime degradation constant for 4-ohm-cm FZ silicon is nearly the same as for silicon containing no lithium ($K \approx 6 \times 10^{-6} \text{ cm}^2/\text{n-sec}$), which is consistent with the lack of impurity dependence for neutron damage. The degradation constant for oxygen-rich QC silicon, however, is more than twice as great, suggesting a radiation-induced recombination center which contains or whose creation depends upon oxygen. Second, more than 90% of the neutron damage was annealed at temperatures between 300° and 380°K . From Stein's data, one would expect less than 10% recovery for non-lithium-diffused n-type silicon subjected to the same annealing schedule. This is to be contrasted with the insignificant impurity dependence of the annealing observed for phosphorus- and arsenic-doped n-type silicon. Third, the activation energies determined from isothermal and isochronal anneals are very close to $E = 0.66 \pm 0.05 \text{ eV}$ for the energy of lithium diffusion in FZ silicon. The annealing results for QC silicon are more uncertain, but indicate an energy of $E \approx 1.2 \pm 0.6 \text{ eV}$. The activation energy for lithium-oxygen dissociation and lithium diffusion is thought to be about $1.07 \pm 0.05 \text{ eV}$. This strongly suggests that the anneal depends on the diffusion of lithium to the neutron-produced recombination centers in both FZ and QC silicon. Finally, the effective frequency factor of $\nu \approx 10^7 \text{ sec}^{-1}$ for annealing in FZ silicon suggests long-range migration.

8.2 ELECTRON-SPIN RESONANCE

Three specific defects have been observed in electron-irradiated lithium-diffused silicon, two by electron-spin resonance techniques and one by infrared absorption measurements. In QC silicon, the Si-B1 center introduction rate is the same as in non-diffused silicon ($\sim 0.15 \text{ cm}^{-1}$) as long as the lithium density is much less than the oxygen density. When the lithium and oxygen densities are comparable, the B1 center introduction rate is significantly reduced ($\sim 0.025 \text{ cm}^{-1}$). We can attribute this to the lithium-oxygen pairing, reducing the number of oxygen atoms available to form oxygen-vacancy (Si-B1) centers, or to competition between oxygen and the positively charged donors for the vacancies. The B1 center

in lithium-diffused silicon is found to anneal below 400°K instead of near 500°K , as in nondiffused silicon. The LiV^{+} density and conductivity decreased as the Si-B1 center annealed. When phosphorus-doped silicon is lithium-diffused to a lithium donor density up to three times the original phosphorus density, the number of phosphorus donors remains unchanged, indicating that lithium-phosphorus pairing does not occur. In phosphorus-doped lithium-diffused silicon (10^{16} P/cc; $\sim 10^{16}$ Li/cc), 30-MeV electron irradiations of 10^{17} e/cm² below 150°K are found to produce Si-G8 (phosphorus-vacancy) defects at a rate comparable to nondiffused silicon. Production and annealing studies on the Si-G8 center at these density and fluence levels indicate that the presence of lithium has little or no effect on the creation or annealing of that center.

8.3 INFRARED ABSORPTION

Infrared absorption measurements indicate that, at fluences of 10^{17} e/cm², the introduction rate of the Si-G7 center (divacancy) is comparable to electron-irradiated lithium-diffused (5×10^{16} Li/cc) and nondiffused silicon. The divacancy anneals at or below 300°K in diffused silicon, compared with $\sim 325^{\circ}$ to 575°K in nondiffused silicon. As the $1.8\text{-}\mu\text{m}$ divacancy band disappears, new bands near 1.4 and $1.65\text{ }\mu\text{m}$ appear, and these anneal near 600°K .

8.4 COMPUTER SIMULATION OF SOLAR CELL

Our ESR and IR measurements have identified three known radiation defects, thought to be recombination centers, in lithium-diffused silicon, and have measured their introduction and anneal rates. From lifetime measurements, we have information about the energy levels, introduction, and annealing rates of radiation-induced recombination centers in lithium-diffused silicon of various lithium and oxygen densities. Although we have not identified these defects, their measured introduction and annealing rates should permit us to use our PN computer code to predict the degradation and anneal of solar cells.

The PN code has been shown to be a very useful tool for computing the current-voltage (I-V) characteristics of solar cells and in studying how

changes in the cell, such as radiation damage or different doping density profiles, change the electrical output. The agreement between results from the PN code for a simple step-junction cell and analytical expressions which hold for this simplified cell configuration give confidence that the code gives correct results for more complicated and realistic junctions which cannot be analyzed by the simpler techniques. The code has been successfully applied to calculate the I-V degradation of a realistic solar cell irradiated with low-energy protons. Both the original recombination center densities and the radiation damage centers were spatially nonuniform. The code's predictions compare favorably with experimental results.

9. RECOMMENDATIONS FOR FUTURE WORK

The overall goal of this research program has been the development of better solar cells for space missions and the accumulation of the basic data required to correctly predict the effect of radiation damage on solar cell performance. These objectives have been partially fulfilled over the past several years, during which a large amount of information has been obtained on radiation damage to silicon with and without lithium. To bring this program to a successful conclusion, the main tasks which remain are the development of a reliable method for predicting the performance of solar cells subjected to various radiation fluences and the application of this information to try to improve the output and radiation hardness of solar cells. Gulf Rad Tech suggests that the continuation of the present program concentrate heavily on these two areas.

The present methods of predicting the effect of radiation damage on solar cell performance rely extensively on costly and time-consuming long-term testing of solar cells under simulated flight conditions. Rad Tech believes that the delay and costs inherent in this method could be greatly reduced by utilizing a program combining accelerated testing and analytical prediction. Under the accelerated tests, solar cells would be irradiated to fluences comparable to those experienced on space missions but at considerably faster rates, so that the total fluences could be delivered in a few days or weeks rather than months or years. From our experience with basic mechanisms of radiation damage, the dose rates can be chosen so that dose rate effects are negligible and only the total dose is important. Using the results from the accelerated tests for arbitrary fluences, the results could be extrapolated or interpolated to the specific radiation time histories for any mission. This analytic prediction could be accomplished using the PN code, which has been described previously. For each cell, the parameters for the code would be determined by independent

lifetime and capacitance-voltage measurements and then by comparison of calculated I-V curves with experiment. When satisfactory results have been obtained for the unirradiated cells, changes in the parameters due to radiation damage would be estimated from the open literature, and these parameters would be adjusted until agreement was again obtained between calculated I-V curves for a specific fluence and the corresponding experimental results from the accelerated tests. Once the parameters have been determined for a given cell and a particular kind of radiation per unit fluence, results can be easily predicted for any other combination of irradiating particles and fluences.

The increased demand for power and low weight on space missions emphasizes the need for more efficient solar cells. The gradual improvement in solar cell performance since they were first suggested has resulted mostly from improved technology in the manufacturing process. However, there is still much that is not known about how important certain features of a solar cell are in determining its performance. Consequently, without such knowledge, solar cell manufacturers cannot be sure what are the most advantageous avenues for improvement and, therefore, where to concentrate their efforts. Many attempts have been made to analyze the operation of solar cells, but these efforts have been hampered by the complexity of the equations and the many assumptions that often had to be made to obtain tractable problems. In particular, it was difficult to accurately consider nonuniform spatial effects such as that due to low-energy proton damage.

Since the PN code incorporates the complete equations for the flow of charges in the semiconductor, it can simulate solar cells, including surface and depletion region effects, without resorting to gross simplifying assumptions. Also, nonuniform spatial effects can be readily included and parametric studies of the effect of design changes can be performed easily and accurately.

In summary, Rad Tech believes that continued studies on solar cells could most profitably be directed to developing better and cheaper prediction techniques for radiation effects on solar cells and to studying

the basic mechanisms of solar cell operation, with the aim of improving their operation and radiation hardness. These objectives could be obtained by a combined program of accelerated testing and analytic study utilizing the PN code.

10. NEW TECHNOLOGY

No new technology is currently being developed or employed in this program.

11. PUBLICATIONS AND PRESENTATIONS

A paper entitled, "Minority-Carrier Lifetime Degradation and Anneal in Neutron-Irradiated Lithium-Diffused n-Type Silicon," by B. C. Passenheim and J. A. Naber, appeared in Radiation Effects 2, 229-231, March 1970. This paper described work performed during 1969 under contract NAS7-100.

A paper entitled, "Lithium—An Impurity of Interest in Radiation Effects of Silicon," by J. A. Naber, H. Horiye, and B. C. Passenheim, was presented at the 1970 International Conference on Radiation Effects in Semiconductors, held at the State University of New York at Albany, N.Y., in August 1970. This paper is to be published in Radiation Effects during 1971.

A paper entitled, "Production and Annealing of Defects in Lithium-Diffused Silicon after Irradiation with 30-MeV Electrons and Fission Neutrons at 300°K," by J. A. Naber, B. C. Passenheim, and R. A. Berger, was presented and published in the Proceedings of the Eighth Photovoltaic Specialists Conference, held in Seattle, Washington, August 4-6, 1970.

REFERENCES

1. J. A. Naber, H. Horiye, and V. A. J. van Lint, "Radiation Effects on Silicon," Gulf Rad Tech report GA-8668, August 20, 1968.
2. J. A. Naber, B. C. Passenheim, and R. A. Berger, "Study of Radiation Effects in Silicon Solar Cells," Gulf Rad Tech report GA-9909, January 23, 1970.
3. R. G. Downing, J. R. Carter, and W. K. van Atta, "Study of Radiation Effects in Lithium-Doped Silicon Solar Cells," TRW Systems report on JPL contract 952251, November 15, 1968.
4. L. B. Valdes, Proc. IRE 42, 420 (1954).
5. J. C. Irvin, Bell System Tech. J. XLI, 387 (1962).
6. J. A. Naber, H. Horiye, and E. G. Wikner, "Radiation Effects on Silicon," Gulf Rad Tech report GA-8016, June 20, 1967.
7. C. Kittel, Introduction to Solid-State Physics, John Wiley & Sons, New York (1963).
8. K. C. Nomura and J. S. Blakemore, Phys. Rev. 112, 1607 (1958).
9. K. C. Nomura and J. S. Blakemore, Phys. Rev. 121, 734 (1961).
10. V. A. J. van Lint et al., "Radiation Effects on Silicon Solar Cells," NASA report NASA-CR-56563, December 4, 1963.
11. W. Shockley and W. T. Read, Jr., Phys. Rev. 87, 835 (1952).
12. R. E. Leadon and J. A. Naber, J. Appl. Phys. 40, 2633 (1969).
13. M. Lax, Phys. Rev. 119, 1502 (1960).
14. V. A. J. van Lint and D. P. Snowden, "Radiation Effects on Silicon," NASA report NASA-CR-69568, July 21, 1965.
15. J. M. Weingart, "Defect Structure and Behavior in Electron-Irradiated Lithium-Diffused Silicon Solar Cells," Conf. Record of Eighth IEEE Photovoltaic Specialists Conference, IEEE Catalog No. 70C32ED, 267 (August 1970).
16. J. W. Corbett, R. W. McDonald, and G. D. Watkins, J. Phys. Chem. Solids 25, 873 (1964).
17. T. M. Flanagan et al., "Transient Radiation Effects," Gulf Rad Tech report GA-8338, December 1967.
18. A. C. Damask and G. J. Dienes, Point Defects in Metals, Gordon and Breach, New York (1963).
19. G. Brucker et al., "Study to Determine and Improve Design for Lithium-Diffused Solar Cells," Third Quarterly Report, RCA report AED-R-3562F, April 10, 1970.

20. R. G. Downing et al., "Study and Determination of an Optimum Design for Space-Utilized Lithium-Doped Solar Cells," TRW Systems report 13154-6011-RO-00, June 19, 1970.
21. E. M. Pell, Solid-State Physics in Electronics and Telecommunications, Vol. I, p. 261, Academic Press, New York (1960).
22. R. G. Downing, J. R. Carter, and W. K. van Otto, "Study and Determination for Optimum Design for Space-Utilized Lithium-Doped Solar Cells," TRW Systems report April 15, 1970.
23. Private communication, J. C. Corelli, Rensselaer Polytechnic Institute, 1970.
24. V. S. Vavilov, "Interaction of Radiation Defects with Impurities," Radiation Damage in Semiconductors, p. 120, 7th Intl. Conf. on Physics of Semiconductors, Paris, 1964, Academic Press, New York, 1965.
25. R. A. Cesena et al., "Research on the Physics of Transient Radiation Effects," Gulf Rad Tech report prepared under contract DAAG39-68-C-0060, April 1970.
26. B. C. Passenheim and J. A. Naber, Radiation Effects 2, 229 (1970).
27. H. J. Stein, J. Appl. Phys. 37, 3382 (1966).
28. G. D. Watkins, "A Review of EPR Studies in Irradiated Silicon," Proc. 7th Intl. Conf. on Physics of Semiconductors, Radiation Damage in Semiconductors, Dunod, Paris, 1965.
29. E. G. Wikner et al., "Transient Radiation Effects," Gulf Rad Tech report GA-7607, 1967 (AD-808-797).
30. T. M. Flanagan et al., "Transient Radiation Effects," Gulf Rad Tech report GA-8338, December 1967 (AD-838-975).
31. T. M. Flanagan and T. F. Wrobel, IEEE Trans. Nucl. Sci. NS-16, 130 (December 1969).
32. G. D. Watkins, J. W. Corbett, and R. M. Walker, "Spin Resonance in Electron-Irradiated Silicon," J. Appl. Phys. 30, 1148 (1959).
33. R. E. Leadon et al., "Research on the Physics of Transient Radiation Effects," Gulf Rad Tech report GA-9334, 1969.
34. G. D. Watkins and J. W. Corbett, "Defects in Irradiated Silicon: EPR and ENDOR of the Si-E Center," Phys. Rev. 134, A1359.
35. H. Horiye, Gulf Radiation Technology unpublished data.
36. F. L. Vook and H. J. Stein, "Production of Defects in N-Silicon," Radiation Effects in Semiconductors, F. L. Vook, ed., Plenum Press, New York (1968).
37. L. J. Cheng et al., Phys. Rev. 152, 761 (1966).
38. H. Y. Fan and A. K. Ramdas, J. Appl. Phys. 30, 1127 (1959).
39. R. C. Young et al., J. Appl. Phys. 40, 271 (1969).

40. G. D. Watkins and J. W. Corbett, *Phys. Rev.* **138**, A543 (1965).
41. R. L. Cummeron, *Phys. Rev.* **95**, 16 (1954).
42. D. A. Kleinman, *B. S. I. J.* **40**, 85 (1961).
43. M. J. Barrett and R. H. Stroud, "A Model for Solar Cell Performance in Space," Final Report, contract JPL 952246, February 28, 1969.
44. M. J. Barrett *et al.*, "Solar Cell Performance Mathematical Model," Final Report, contract JPL 952548, June 15, 1970.
45. V. A. J. van Lint *et al.*, "Short-Pulse Gamma-Radiation Effects on Dynamic Electronic Components," AFWL-TR-67-20, May 1967.
46. R. E. Leadon and M. L. Vaughn, "Short-Pulse Radiation Effects on Dynamic Electronic Components, DASA-2358, June 1969.
47. R. E. Leadon *et al.*, "Radiation Effects on Dynamic Electronic Components," DASA-2546, July 1970.
48. Texas Instruments, Inc., bulletin DL-S 657985, August 1965.
49. J. J. Wysocki and P. Rappaport, *J. Appl. Phys.* **31**, 571 (1960).
50. W. C. Cooley and M. J. Barrett, "Handbook of Space Environmental Effects on Solar Cell Power Systems," NASA report on contract NASW-1345, January 1968.
51. J. F. Janni, "Calculations of Energy Loss, Range, Path Length, Straggling, Multiple Scattering, and the Probability of Inelastic Nuclear Collisions for 0.1- to 100-MeV Protons," AFWL-TR-65-150, September 1966.
52. D. L. Crowther *et al.*, "An Analysis of Nonuniform Proton Irradiation Damage in Silicon Solar Cells," *IEEE Trans. Nucl. Sci.* **NS-13**, No. 5, 37-49 (October 1966).
53. R. L. Statler and D. J. Curtin, "Low-Energy Damage in Partially Shielded and Fully Shielded Silicon Solar Cells," Communications Satellite Corp. report CL-24-68, November 21, 1968.
54. M. G. Buehler, *Proc. IEEE* **56**, 1741 (October 1968).
55. B. L. Gregory, *IEEE Trans. Nucl. Sci.* **NS-16**, 53 (December 1969).